



Politecnico di Bari

Repository Istituzionale dei Prodotti della Ricerca del Politecnico di Bari

Design of devices for integrated systems based on optical and microwave technologies for 5G

This is a PhD Thesis

Original Citation:

Design of devices for integrated systems based on optical and microwave technologies for 5G / Loconsole, Antonella Maria. - ELETTRONICO. - (2022). [10.60576/poliba/iris/loconsole-antonella-maria_phd2022]

Availability:

This version is available at <http://hdl.handle.net/11589/246260> since: 2022-12-22

Published version

DOI:10.60576/poliba/iris/loconsole-antonella-maria_phd2022

Publisher: Politecnico di Bari

Terms of use:

(Article begins on next page)



Politecnico
di Bari

Department of Electrical and Information Engineering
ELECTRICAL AND INFORMATION ENGINEERING

Ph.D. Program

SSD: ING-INF/02–ELECTROMAGNETIC FIELDS

Final Dissertation

Design of devices for integrated systems
based on optical and microwave
technologies for 5G

by

Antonella Maria Loconsole

Supervisor:

Prof. Francesco PRUDENZANO

Coordinator of Ph.D. Program

Prof. Mario Carpentieri

Course n°35, 01/11/2019-31/10/2022



Politecnico
di Bari

Department of Electrical and Information Engineering
ELECTRICAL AND INFORMATION ENGINEERING

Ph.D. Program

SSD: ING-INF/02–ELECTROMAGNETIC FIELDS

Final Dissertation

Design of devices for integrated systems
based on optical and microwave
technologies for 5G

by

Antonella Maria Loconsole

Referees:

Prof. Guido PERRONE

Prof. Alessandro CHIASERA

Supervisor:

Prof. Francesco PRUDENZANO

Coordinator of Ph.D. Program

Prof. Mario Carpentieri

Course n°35, 01/11/2019-31/10/2022

Abstract

In this PhD thesis, innovative microwave and optical devices for Fiber-Wireless (FiWi) networks in 5G and Internet of Things (IoT) scenarios have been designed, optimized and characterized. They find different applications in communications, industrial, medical, and environmental monitoring applications, with the aim to provide wide bandwidth and low latency. In particular, the thesis reports: i) the design and optimization of a multilayer air-filled SIW array antenna, operating at $f = 60 \text{ GHz}$, which will be constructed and characterized at the Institut d'Electronique et des Technologies du numéRique (IETR) in Rennes (France); ii) the design, fabrication and characterization of microwave applicators for industrial monitoring and thermal ablation of cancer; iii) the design and optimization of continuous wave (CW) and pulsed laser emitting at $\lambda_s = 3.92 \mu\text{m}$ in the mid-infrared (Mid-IR) wavelength range, as optical sources in FiWi hybrid networks. Part of the obtained results have been published in the Proceedings of National and International Conferences or on International Journals, as listed at the end of the thesis.

Contents

Introduction	1
1 Microwave and optical technologies for IoT and 5G	3
1.1 Microwave technology for IoT and 5G	4
1.1.1 Antennas	4
1.1.2 Sensors and applicators.....	5
1.1.3 Metamaterials	7
1.2 Optical technology for IoT and 5G	8
2 Theory	11
2.1 Microwave technologies for IoT and 5G	11
2.1.1 Substrate Integrated Waveguide	11
2.1.2 Metamaterials	12
2.2 Optical technology for IoT and 5G	16
2.2.1 Analytical model for fluoroindate glass fiber-based lasers .	16
2.2.1.1 Continuous wave laser	16
2.2.1.2 Gain-switching pulsed laser	18
3 Low-cost air-filled SIW multilayer array antenna at mm-waves	23
3.1 Introduction	23
3.2 Power losses investigation	23
3.3 Antenna design	26
3.3.1 Elementary 2×2 slot sub-array	26
3.3.1.1 Optimization of the coupling aperture	29
3.3.1.2 Optimization of the cavity wall distances	31
3.3.1.3 Optimization of the radiating slot	33
3.3.1.4 Optimized geometry	34
3.3.2 4×4 slot sub-array	35
3.3.3 8×8 slot array	39
3.4 Connector to air-filled SIW transition	42

3.4.1	Connector	42
3.4.2	Connector-to-GCPW transition	43
3.4.3	Wide GCPW-to-small GCPW transition	44
3.4.4	Small GCPW-to-SIW transition	44
3.4.5	SIW-to-air-filled SIW transition	45
3.4.6	Connector-to-air-filled SIW transition	46
3.5	Conclusions	49
4	Design of a Substrate Integrated Waveguide microwave sensor for water-in-fuel applications.....	50
4.1	Introduction	50
4.2	Water-fuel blend characterization	51
4.3	Applicator design	54
4.3.1	Single slot SIW applicator in air	55
4.3.2	Cross slot SIW applicator in air	58
4.4	Simulation of cross-slot SIW applicator as sensor, water-in-diesel background	63
4.5	Cross-slot SIW applicator characterization, air background	65
4.6	Cross-slot SIW applicator characterization, water-in-diesel background	66
4.7	Conclusions	72
5	Design of low-cost mini-invasive needle applicators for cancer thermal ablation	73
5.1	Introduction	73
5.2	Applicator design	73
5.2.1	Geometrical investigation	75
5.2.1.1	16G applicator	76
5.2.1.2	14G applicator	79
5.2.2	Dielectric materials: analysis and characterization	81
5.2.2.1	Study on the permittivity of the dielectric section	82
5.2.2.2	Study on the thermal conductivity and capacity of the dielectric constant	82
5.2.2.3	Study on the material of the dielectric section	84
5.2.3	Influence of the cooling circuit on microwave heating	85
5.3	Experiment and prototype characterization	89
5.4	Conclusions	90

6 Design of a Split Ring Resonator-based metamaterial for microwave impedance matching with biological tissue	91
6.1 Introduction	91
6.2 Microwave applicator design	92
6.3 Experimental	98
6.4 Comparison with literature	102
6.5 Conclusions	104
7 Design of a Mid-IR laser based on a Ho:Nd-codoped fluoroindate fiber	105
7.1 Introduction	105
7.2 Energy transfer coefficients recovery	106
7.3 Laser design	112
7.4 Results discussion	115
7.5 Conclusions	117
8 Design of a gain-switching pulsed laser based on a Ho³⁺-doped fluoroindate fiber	118
8.1 Introduction	118
8.2 Laser design	118
8.2.1 Model validation	120
8.2.2 Pulsed laser results	121
8.3 Conclusions	130
Conclusions	131
List of publications	133
References	137

Introduction

In recent years, hybrid solutions for communications, industrial, medicine, environmental monitoring applications, employing both optical and microwave technologies have attracted much research interest. These hybrid solutions have permitted high efficiency and exploitation of innovative and fast wireless communication channels, characterized by wide bandwidth and low latency. Moreover, the increasing number of devices connected to the Internet, due to Machine-to-Machine (M2M) scenarios, and the increasing amount of shared data constitutes a big challenge for future networks.

Optical access networks are an excellent candidate to ensure a huge amount of bandwidth, in order to adopt wavelength division multiplexing (WDM) technique to transmit different signals in parallel.

Wireless networks allow to reach users with large coverage areas and provide larger flexibility with respect to wired solutions. Employing Multiple-Input-Multiple-Output (MIMO) antennas, beamforming and beam-steering techniques, users can be followed by the base transceiver station (BTS) during the communication, improving the link efficiency. On the other hand, fiber and integrated optical technology allows long haul and high-capacity information transport. The combination of these two technologies is the so-called Fiber-Wireless (FiWi) network, in which optical and microwave or millimeter-wave devices find applications.

FiWi networks can be designed employing the Radio-over-Fiber (RoF) and the Radio-and-Fiber (R&F) scenarios. While RoF networks use optical fiber as an analog transmission medium between a central control station and one or more Remote Antenna Units (RAUs) with the central station being in charge of controlling access to both optical and wireless media, in R&F networks access to the optical and wireless media are controlled separately each other by using in general two different Medium Access Control (MAC) protocols in the optical and wireless media, with protocol translation taking place at their interface.

The aim of this research thesis is to propose both optical and microwave devices for FiWi, RoF, and R&F scenarios for 5G communications. The obtained results are illustrated by following this organization:

- (i) Chapter 1 is an introduction on optical and microwave devices employed for IoT and 5G communications, with particular reference to the ones which are object of the thesis.
- (ii) Chapter 2 recalls the theory for the design of SIW antennas, metamaterials, and Mid-IR lasers.
- (iii) Chapter 3 describes the design and the optimization of a partially-air-filled SIW antenna, working at $f = 60 \text{ GHz}$.
- (iv) Chapter 4 describes the design, fabrication, and characterization of a SIW sensor for detection of water in diesel.
- (v) Chapter 5 describes the design, fabrication, and characterization of a needle applicator for hyperthermal cancer therapy.
- (vi) Chapter 6 describes the design, fabrication, and characterization of a microwave applicator, optimized with metamaterials, for skin cancer therapy.
- (vii) Chapter 7 describes the design and the optimization of a continuous wave laser, working at $\lambda = 3.92 \mu\text{m}$, based on a $\text{Nd}^{3+}:\text{Ho}^{3+}$ -codoped fluoroindate fiber, in order to increase the slope efficiency with respect to the Ho^{3+} -heavily-doped fluoroindate fiber.
- (viii) Chapter 8 describes the design and the optimization of a gain-switching pulsed laser, working at $\lambda = 3.92 \mu\text{m}$, based on a Ho^{3+} -heavily-doped fluoroindate fiber.

1 Microwave and optical technologies integration for IoT and 5G

The main goal of the fifth generation (5G) of communication is to serve an ever-growing number of users. This is due to the increasing need of efficient communication channels, including the already diffused Internet of Things (IoT) applications that aim to connect many different devices, such as mobile smartphones, vehicles, industrial machines, and smart homes devices. With this goal, very high-speed wired (optical fibers) and wireless technologies must be developed. As for wireless communications, it is mandatory to use high frequency carriers to reach the data rates of around 100 Gbit/s foreseen for future beyond 5G networks.

Employing higher frequencies usually called millimeter waves (mm-Waves) for the 5G carriers, including $f = 28 \text{ GHz}$, $f = 39 \text{ GHz}$, $f = 60 \text{ GHz}$, and $f = 73 \text{ GHz}$, can be a good way to achieve this goal. However, mm-Wave decay very quickly in free space, requiring very small network cells. This changes the network structure with respect to those employed nowadays, introducing the concept of nano- or pico-cells. Moreover, to ensure high speed communication, the base transceiver station (BTS) should be fed by fiber optics, employing Radio-over-Fiber (RoF) and Radio&Fiber (R&F) solutions. This scenario suggests that the full integration of microwave and optical technology is mandatory in the next generation of communication systems.

The main topics on which this PhD thesis is focused are:

- (i) Millimeter-wave antennas for BTS, portable devices, and devices to be monitored;
- (ii) Microwave applicators for IoT medical, industrial, and environment applications, optimized with metamaterials;
- (iii) Optical sources in the Mid-IR wavelength range, for biomolecule sensing and atmosphere monitoring.

1.1 Microwave technology for IoT and 5G

Microwave and mm-Wave technology can be employed in 5G solutions, mainly through antennas and sensors.

Antennas working at 5G frequencies are used for the wireless link with the user, which should be secure, stable, and fast. Moreover, to maintain the link as the user moves is the nano-cell, antennas should be able to change the direction of the main lobe to follow those movements. This can be obtained with beam-steering and beam-forming techniques, allowing power consumption optimization. To increase the channel throughput Multiple-Input-Multiple-Output (MIMO) antennas can be considered.

The application areas of mm-wave communications are not only limited to cellular communication, but also include different areas, such as radar communication, automotive radars, device-to-device communication, medical imaging, security and healthcare, which involve wide range of frequency starting from few gigahertz till to $f = 300 \text{ GHz}$ [1]. All these applications can be considered as a part of IoT networks, in order to monitor industrial processes or for smart home solutions.

1.1.1 Antennas

Nowadays, MIMO antennas are widely employed in communication, because they can serve multiple users at a time and follow them as they move in the antenna area, optimizing power consumption.

In particular, mm-Wave antennas are attracting much research and industrial interest, thanks to the possibility of faster communications for the next generation systems as 5G and 6G [2]. Moreover, wideband antennas allow multiplexing techniques, increasing transmission capacity and throughput. The unlicensed band around $f = 60 \text{ GHz}$ is employed and promises different potential applications, such as short-range wireless communication, radar, and high-speed mobile connections [3-7]. Moreover, the small wavelength of the mm-wave region facilitates the array architecture to be embedded into portable devices. However, due to atmospheric absorption and free-space attenuation, antennas working in this band require high gain and beam-steering. The antenna array technology helps in producing highly directive and steerable beams. To achieve the steering, a specific time delay is introduced between the elements of the array so that the contributions from all the elements are coherently summed at a particular angle to the array face [1]. These antennas can be designed by means of different technologies, such as microstrip, low-temperature co-fired ceramic (LTCC),

diffusion bonding, and substrate integrated waveguide (SIW) [2-15]. Microstrip is low-cost and easy to be constructed, but suffers of parasite current losses, while LTCC and diffusion bonding guarantee high-performance but are very expensive [2,6-7]. SIW technology can be considered as a good trade-off, since it is quite simple, low-cost, and can handle intermediate power levels although losses are higher than those of diffusion bonding and LTCC approaches [8-16]. SIW technology can ultimately satisfy the required antenna performances, if compared to more expensive diffusion bonding and LTCC technologies [16-18].

Substrate Integrated Waveguide (SIW) technology is a technique allowing the integration of multiple active and passive microwave devices into one only substrate. The devices can be embedded by employing metalized vias, drawing the shape of waveguides, couplers, filters, or antennas.

This technology has several advantages, such as a high integration level, compactness, high power handling, easiness of construction, employment of commercial substrates. These substrates should have low losses, in order to maximize the efficiency. Recently, partially air-filled SIW technology has been proposed to reduce dielectric losses and reach better gain [19-21]. Moreover, multilayer antennas can be considered a good way to enlarge the bandwidth and obtain compact arrays [5-6].

The design of array antennas at mm-wave frequencies is a challenging work, including many aspects that should be taken into account [1]:

- (i) the antenna size should be small, in order to integrate it in portable devices, but this may lead to higher fabrication errors and complexity. Also the spacing between the array elements should be small, to avoid undesired side lobes. However, proximity among elements could cause mutual coupling that may degrade the antenna performances;
- (ii) the losses of the array feeding lines can be considerable at mm-wave frequencies and they should be minimized, in order to obtain good antenna efficiency;
- (iii) the employment of commercial substrates with low losses is desired in order to guarantee high integration level with other electronic devices.

1.1.2 Sensors and applicators

Microwave sensors and applicators are widely employed in IoT networks because they allow many different detections and monitoring. In this thesis, this kind of devices are proposed. They could be integrated in IoT systems for

environment, industrial, medicine applications. One example is detecting water in diesel by using SIW microwave device, working at about $f = 12 \text{ GHz}$ [22]. This kind of sensors are based on the interaction between the sample and the electromagnetic wave. Since water dielectric constant is about forty times larger than the diesel one, little concentrations of water cause large variations of the blend dielectric constant, allowing an easy detection. These sensors are also low profile and low-cost, allowing real-time monitoring of industrial processes. They are of interest in industrial processes and environment monitoring.

Microwave technology can also be employed for medical applicators. Microwave applicators are generally composed by a microwave generator and by an antenna. They can be designed employing different kinds of radiating sections such as monopole, dipole, slot, and helical antennas. Generally, the electromagnetic (EM) wave is delivered to the target tissues via intracavitary, percutaneous, or laparoscopic paths [23-32]. Moreover, the treatment session can be supervised with the aid of ultrasound scanning, magnetic resonance imaging, or an electromagnetic tracking system [33].

Percutaneous microwave applicators are antennas emitting directly into the human tissue, driven with the aid of a hypodermic tube. The tissue is heated by the electromagnetic field absorption. The antenna design plays an essential role in the optimization of the radiation pattern within the treated tissue and of the efficiency of electromagnetic energy transfer. These aspects are also influenced by the dielectric features of the biological medium. A correct impedance matching of the radiating section of the applicator with the human tissue is the first design objective. Indeed, stationary waves and dispersions along the feeding line can cause overheat of the applicator and undesired damages to the surrounding healthy tissues. The design goals of the applicator can be summarized as:

- i) reducing the antenna size, to embed it into a hypodermic tube for a mini-invasive approach;
- ii) choosing a coaxial cable with small section and ensuring high power transmission;
- iii) optimizing the antenna to obtain temperature increase of the target tissue with a quite spherical profile. This last feature is important for an efficient treatment with a scalable size. In fact, it is possible to control the damaged region size by varying the input power and the time duration of the ablation session.

1.1.3 Metamaterials

In order to improve performances of microwave devices, it is possible to employ metamaterials (MTMs). They are defined as engineered artificial materials with unusual properties, not available in nature. An example is shown in Fig. 1.1 [34]. They are structures composed by very little cell elements, compared to the guided wavelength. Therefore, they can be considered as a homogeneous structure, from an electromagnetic point of view. They are characterized by specific relative dielectric permittivity ϵ_r and relative magnetic permeability μ_r , that can be opportunely dimensioned, also having negative values. Indeed, MTMs can be classified by the sign of the relative dielectric permittivity and the magnetic permeability. The four possible sign combinations in the pair (ϵ_r, μ_r) can be arranged in a $\epsilon - \mu$ diagram, as shown in Fig. 1.2 [34].

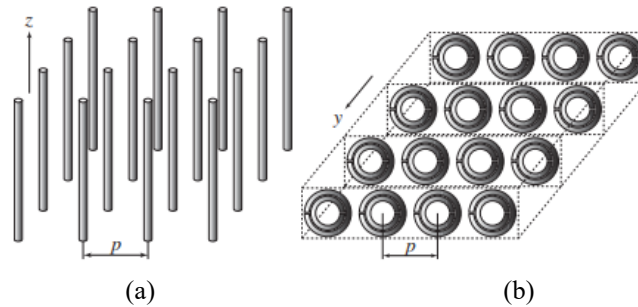


Fig. 1.1. Example of metamaterials, (a) parallel wires thin (PTW), (b) circular splitting ring resonators (CSRR) [34].

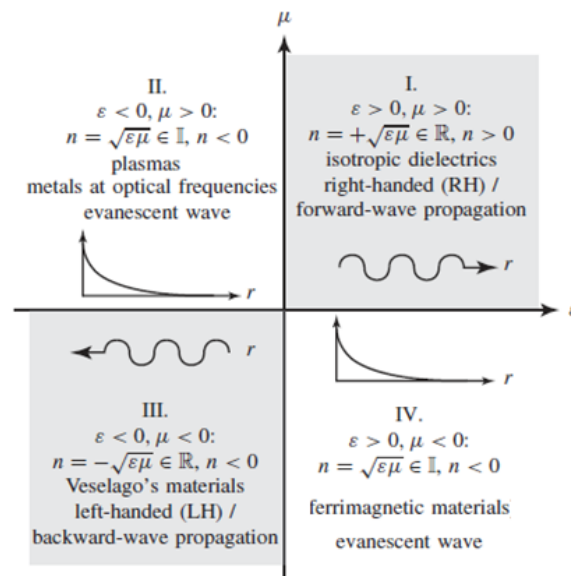


Fig. 1.2. Permittivity-permeability ($\epsilon - \mu$) and refractive index (n) diagram [34].

Many different geometries have been proposed, such as squared split ring resonators (SSRR), circular split ring resonators (CSRR), which exhibit ($\epsilon_r > 0$, $\mu_r < 0$), and parallel wires thin (PTW), which exhibits ($\epsilon_r < 0$, $\mu_r > 0$) [34].

MTMs are usually added to the radiating structure, to improve the radiative properties. These materials allow to enhance the gain and/or bandwidth of the antenna. Moreover, they can help in miniaturizing the antenna keeping good performances if compared to the original one [32,34].

In this thesis, metamaterials are investigated for improve the impedance matching of medical applicators with skin, for ablation of melanoma.

1.2 Optical technology for IoT and 5G

Hybrid optical-microwave FiWi is an attractive technique for 5G cellular system and has gained more and more attentions thanks to its centralized signal processing and network management, simple remote antenna unit (RAU) and low-cost implementation [35]. Both RoF and R&F technologies can be employed in FiWi networks. To support a large number of antennas in RAUs, wavelength division multiplexing (WDM) techniques in fiber are highly desired to ensure high speed communications. Moreover, space-division multiplexing (SDM) based on multi-core fiber (MCF), or multi-mode fiber (MMF) has proved its great merit in overcoming the barrier from capacity limit of single mode fiber [36-37].

In particular, in R&F scenarios, different optical devices can be employed, such as optical sources working in the mid-infrared (Mid-IR) and tunable lasers, tunable receivers, optical amplifiers, optical switches, optical combiners, and photodetectors [35].

Mid-IR lasers can be employed as optical sources for feeding the BTS with large bandwidth. Moreover, pulsed lasers can be employed as modulators for microwave signal generations [35,38-39].

Mid-IR emitting sources have attracted much interest during the last years, especially thanks to their multiple potential application in particular for fast communications, environmental monitoring, and sensing [40-49]. These lasers can be designed and fabricated considering different fiber glasses, including chalcogenide and fluoride ones, doped or co-doped with different rare-earth ions, as thulium, holmium, dysprosium, erbium, neodymium, and praseodymium, for emission at different wavelengths [50-61].

In particular, fluoroindate fibers exhibit high transparency in the 3-5 μm range, where many air pollutants and biomolecules exhibit light absorption peaks. The reduced optical attenuation $\alpha \approx 0.2 \text{ dB/m}$ from ultra-violet (UV) to Mid-IR about $\lambda = 500 \text{ nm}$ to about $\lambda = 4500 \text{ nm}$, and the low phonon energy of fluoroindate glasses make them good candidates for laser construction and exploitation [40,54,60]. In addition, they are good rare-earth hosts since contrarily to other glasses, it is possible to incorporate also 10 mol.% of rare earth ions, similarly to fluorozirconate glasses.

Fluoroindate optical fibers can exhibit attenuation much smaller with respect to the fluoride ones at longer wavelength, beyond $\lambda = 3.3/3.5 \mu\text{m}$ [60]. During the last years, rare-earth doped fluoroindate glasses have been spectroscopically investigated with the aim of finding new pumping schemes and operating wavelengths [55-59]. Erbium-, dysprosium-, and holmium-doped fluoroindate fibers have attracted particular attention for their emission at $\lambda = 3.5 \mu\text{m}$, $\lambda = 4.2 \mu\text{m}$, and $\lambda = 3.9 \mu\text{m}$, respectively [61-66]. Recently, holmium-doped fluoroindate fibers have been characterized [61,67-72] and continuous wave (CW) lasers emitting at $\lambda_s = 2.875 \mu\text{m}$ [72] and $\lambda_s = 3.92 \mu\text{m}$ [61], pumped at $\lambda_p = 1120 \text{ nm}$ and $\lambda_p = 888 \text{ nm}$ respectively, have been demonstrated. For that pertaining the pulsed laser operation, emissions at the wavelength $\lambda_s = 2.106 \mu\text{m}$ and in the $\lambda_s = 2.95 - 3.015 \mu\text{m}$ range [73-74] have been obtained.

New spectroscopical investigations on fluoroindate glasses co-doped with holmium-neodymium, holmium-europium, and praseodymium-ytterbium have shown that co-doping can lead to an improvement of the emission efficiency if compared to the employment of a single dopant. In particular, holmium-neodymium co-doping could allow better performance than those of heavily-holmium-doped, $N_{Ho} = 2 \times 10^{27} \text{ ions/m}^3$, fluoroindate fiber lasers [75-77].

Pulsed lasers in the middle-infrared (Mid-IR) wavelength range are usually employed as modulators for fast communications. Great research interest was focused on Er^{3+} -doped fluoride fiber, since emission at about $\lambda = 2.8 \mu\text{m}$ and $\lambda = 3.5 \mu\text{m}$ allowed to obtain intriguing laser in continuous wave (CW), gain-switched, and Q -switched regime [78-80]. In particular, in [79] a gain-switched fiber laser operating near $\lambda = 3.5 \mu\text{m}$ via a dual-wavelength pumping scheme was obtained in an erbium-doped fluorozirconate fiber, with stable pulses with repetition rates ranging between $f_R = 15 \text{ kHz}$ and $f_R = 20 \text{ kHz}$ and laser efficiency of $\eta = 4.7\%$.

In this thesis both CW and pulsed optical sources in the Mid-IR range are designed to work at $\lambda_s = 3.92 \mu\text{m}$, employing commercially available fluoroindate fibers, with the aim to propose new sources for FiWi networks.

2 Theory

In this chapter, a recall of theory useful for the design of both the microwave and optical devices, proposed in this thesis, is briefly reported.

2.1 Microwave technologies for IoT and 5G

Substrate integrated waveguide (SIW) technology has been largely employed for the construction of couplers, filters, oscillators, amplifiers, mixers, and antennas since it allows for low-cost implementation. In this thesis, it is exploited to: i) improve 5G antenna radiation characteristics, thus obtaining better performances than those of the conventional microstrip/printed board circuits (PCB) while maintaining the typical advantages of planar technologies; ii) for the construction of a planar microwave applicator optimized with metamaterial; ii) for the construction of a water in fuel sensor. The basis theory devices for the design of the SIW devices is reported in the following. Similarly, the fundamentals of theory for the design of a metamaterials are reported.

2.1.1 Substrate Integrated Waveguide

A typical Substrate Integrated Waveguide is shown in Fig. 2.1.

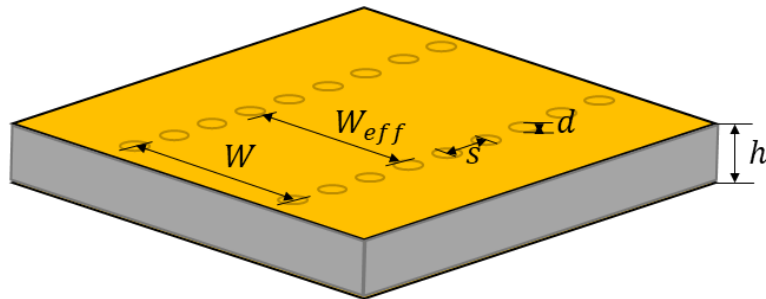


Fig. 2.1. Typical scheme of a SIW

It can be modelled as a rectangular waveguide, employing empirical formulas [16,18]. Its effective width W_{eff} is given by

$$W_{eff} = W - \frac{d^2}{0.95s} \quad (2.1)$$

where W is the SIW width, s is the center-center distance between two next vias, and d is the vias diameter.

The cut-off frequency of the TE_{10} mode can be obtained by

$$f_c = \frac{c}{2\sqrt{\epsilon_r}W_{eff}} \quad (2.2)$$

In order to minimize leakage losses and return losses, the following conditions must be respected:

$$d < \lambda_g/5 \quad (2.3)$$

$$s \leq 2d \quad (2.4)$$

where λ_g is the guided wavelength defined as

$$\lambda_g = \frac{2\pi}{\sqrt{\frac{\epsilon_r(2\pi f_0)^2}{c^2} - \left(\frac{\pi}{W}\right)^2}} \quad (2.5)$$

and f_0 is the operating frequency in free space.

2.1.2 Metamaterials

In order to model the split ring resonators (SRR), the fundamental theory is recalled in this paragraph. The following formulas are employed in to obtain preliminary geometric parameters of the SRRs, before the actual design, refined via CST Microwave Studio® as described in Chapter 6.

The metamaterial based on SRR exhibits an effective magnetic permeability described by the Lorentz model approximation [35,81]:

$$\mu_{r,eff}(\omega) = \frac{F\omega^2}{\omega^2 - \omega_{0m}^2 + j\gamma\omega} \quad (2.6)$$

where $\omega = 2\pi f$ is the angular frequency; ω_{0m} is the resonant frequency; F is the fractional of the unit cell occupied by interior ring; γ is the damping factor due to metal losses.

Starting from (2.6), a frequency range in which $Re(\mu_{r,eff})$ is negative can be identified:

$$\omega_{0m} < \omega < \frac{\omega_{0m}}{\sqrt{1-F}} \quad (2.7)$$

where ω_{pm} is the plasma magnetic frequency. Both ω_{pm} and ω_{0m} are finely tunable by optimizing the geometry of the unit cell.

When an electromagnetic wave propagates orthogonally to the SRR plane, the SRR behavior can be approximatively described by an equivalent LC circuit, where the inductance and the capacitance are related to the currents induced in the metal rings and to the capacitive phenomena between the split terminations (capacitive gap), respectively [81]. If the dimension of unit cell is very small with respect to wavelength λ , the metamaterial layer exhibits an effective capacitance and an effective inductance at the macroscopic/average level, according to the effective medium theory, which leads to the calculation of an effective permeability [35].

Considering a single broadside coupled SRR with square form rings in the xy -plane, the effective magnetic permeability is described by (2.3) [82]:

$$\mu_{r,eff} = \frac{j\omega L_{eff}S}{\Delta_x \Delta_y (R_{eff} - \frac{j}{\omega C} + j\omega L_{eff})} \quad (2.8)$$

$$S = l_x l_y \quad (2.9)$$

where Δ_x and Δ_y are the dimensions of the SRR unit cell in xy -plane; l_x and l_y are the lengths of the metallic ring in the x and y directions, respectively; R_{eff} , C_{eff} and L_{eff} are the effective resistance, the effective capacitance and the effective inductance of the metamaterial, respectively. The effective capacitance is approximatively obtained from the formula for the capacitance per unit length of a strip line [83].

$$C_{eff} = \frac{\epsilon_r \epsilon_0 l}{4} \frac{K(k)}{K'(k)} \quad (2.10)$$

$$k = \tanh \frac{\pi w}{2t} \quad (2.11)$$

$$l = 2(l_x + l_y - s) \quad (2.12)$$

where $K(k)$ and $K'(k)$ are elliptic integrals [35], w, s are the width and the split gap of the SRR; t is the distance between the two SRR in the z direction. The effective inductance is [83]:

$$L_{eff} = \frac{\mu_0 S}{t} \quad (2.13)$$

The effective resistance R_{eff} includes the radiation resistance and the loss resistance [83].

In other words, the control of the effective magnetic permeability, by varying both the inductive and capacitive properties of metamaterial, via a proper SRR optimization, is the basic physics principle of the electromagnetic field focusing. A planar metamaterial lens based on SRR, formed by an array of the unit cell in the rings plane, exhibits an anisotropic negative permeability; if the wave propagates in the z direction, the permeability tensor is [82]:

$$\mu = \mu_0 \begin{pmatrix} 1 & 0 & 0 \\ 0 & 1 & 0 \\ 0 & 0 & \mu_{r,eff} \end{pmatrix} \quad (2.14)$$

When the antenna radiation frequency is within the range for which the permeability element $\mu_{r,eff} < 0$, the x -axis wave vector component is imaginary $k_x = \omega \sqrt{\epsilon_y \mu_z}$, and therefore the component of the electromagnetic field parallel to SRRs plane is evanescent and the sideward radiation forbidden.

Consequently, the main lobe of antenna radiation pattern will be improved while the side lobe is attenuated, and there is an overall improvement in terms of directivity and gain [84].

The metamaterial lens placed on the antenna, in addition to the electromagnetic field focusing properties, allowing the gain increasement, can be used as impedance matching layer. When the radiated electromagnetic waves propagate through media with different permittivity and permeability values an impedance mismatch occurs. The scheme of the normal wave propagation through the two layers sandwiched between two semi-infinite media is illustrated in Fig. 2.2, where the SRR metamaterial layer is placed at distance t_2 from the biological

layer to be matched. The metamaterial lens placed on the antenna, in addition to the electromagnetic field focusing properties, allowing the gain increasement, can be used as impedance matching layer. When the radiated electromagnetic waves propagate through media with different permittivity and permeability values an impedance mismatch occurs. The scheme of the normal wave propagation through the two layers sandwiched between two semi-infinite media is illustrated in Fig. 2.2, where the SRR metamaterial layer is placed at distance t_2 from the biological layer to be matched.

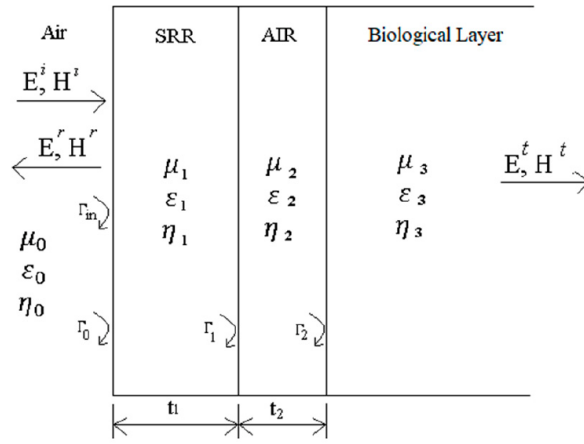


Fig. 2.2. Scheme of the normal wave propagation through the two layers sandwiched between two semi-infinite media. The split ring resonator (SRR) metamaterial layer is placed to distance t_2 from the medium to be matched.

The metamaterial lens, if properly designed, can minimize the mismatch, and maximize the energy transmission. With reference to Fig. 2.2, the general form of wave matrices is given by (2.15).

$$\begin{bmatrix} E^i \\ E^r \end{bmatrix} = \prod_{n=1}^3 \frac{1}{T_n} \begin{pmatrix} e^{j\gamma_n t_n} & \Gamma_{n-1} e^{-j\gamma_n t_n} \\ \Gamma_{n-1} e^{j\gamma_n t_n} & e^{-j\gamma_n t_n} \end{pmatrix} \begin{bmatrix} E^t \\ 0 \end{bmatrix} = \begin{pmatrix} a_{11} & a_{12} \\ a_{21} & a_{22} \end{pmatrix} \begin{bmatrix} E^t \\ 0 \end{bmatrix} \quad (2.15)$$

$$\Gamma_{in} = \frac{E^r}{E^i} = \frac{a_{21}}{a_{11}} \quad (2.16)$$

where T_n , γ_n , and t_n are the transmission coefficient, propagation constant and thickness of the layer n , and Γ_{n-1} is the reflection coefficient at the $(n - 1) - n$ layers interface. The total reflection coefficient of the multiple layers Γ_{in} , given by (2.16), is zero for a ‘perfect’ impedance match. By considering (2.16), the total reflection coefficient is a function of frequency and can be minimized by

appropriately planning the effective magnetic permeability of the metamaterial and by adjusting the distance from the medium to be matched.

2.2 Optical technology for IoT and 5G

2.2.1 Analytical model for fluoroindate glass fiber-based lasers

In the following paragraphs, the models for the $\text{Nd}^{3+}:\text{Ho}^{3+}$ -doped fluoroindate fiber CW laser and for the Ho^{3+} -doped fluoroindate fiber gain-switched laser are reported. These optical sources are of interest in a wide area of applications, such as communications, environmental monitoring, and sensing.

2.2.1.1 Continuous wave laser

The $\text{Ho}:\text{Nd}$ -codoped fluoroindate fiber stimulated emission at $\lambda_s = 3.92 \mu\text{m}$ can be modeled by considering a nine-level system, pumped at $\lambda_p = 808 \text{ nm}$. The complete level scheme, including all the significant ion interactions, is reported in Fig. 2.3. These are the pump absorption, the stimulated emission, the radiative and nonradiative decays, and the energy transfers (ET) between Ho^{3+} and Nd^{3+} ions [76].

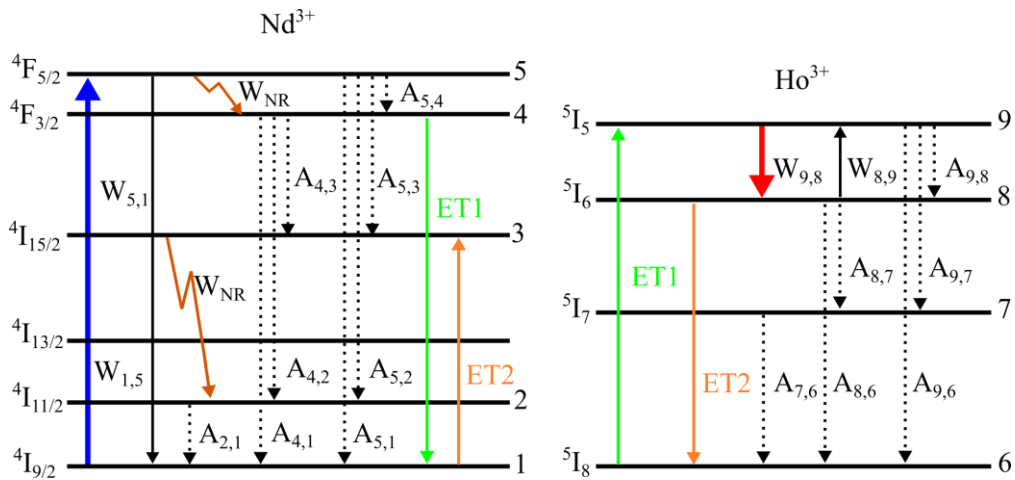


Fig. 2.3. Energy level scheme for the 9-level laser, pumped at $\lambda_p = 808 \text{ nm}$, including pump absorption (transition 1-5, bold blue line) stimulated emission at $\lambda_s = 3920 \text{ nm}$ (transition 9-8, bold red line), radiative decays (dotted lines), nonradiative decays (transition 5-4 and transition 3-2, brown lines), and energy transfers (ET) (green and orange solid lines).

By following the rate equations approach [12,14,24], the energy level populations N_1, \dots, N_5 of neodymium can be written by the nonlinear system (2.17a)-(2.17j) below:

$$\frac{\partial N_1}{\partial t} = -W_{15}N_1 + W_{51}N_5 + A_{51}N_5 + A_{41}N_4 + A_{21}N_2 + K_{ET1}N_6N_4 - K_{ET2}N_8N_1 \quad (2.17a)$$

$$\frac{\partial N_2}{\partial t} = -\frac{1}{\tau_{R2}}N_2 + A_{52}N_5 + A_{42}N_4 + W_{NR}N_3 \quad (2.17b)$$

$$\frac{\partial N_3}{\partial t} = A_{53}N_5 + A_{43}N_4 + K_{ET2}N_8N_1 - W_{NR}N_3 \quad (2.17c)$$

$$\frac{\partial N_4}{\partial t} = -\frac{1}{\tau_{R4}}N_4 + A_{54}N_4 - K_{ET1}N_6N_4 + W_{NR}N_5 \quad (2.17d)$$

$$\frac{\partial N_5}{\partial t} = W_{15}N_1 - W_{51}N_5 - \frac{1}{\tau_{R5}}N_5 - W_{NR}N_5 \quad (2.17e)$$

whereas the energy level populations N_6, \dots, N_9 of holmium can be written as

$$\frac{\partial N_6}{\partial t} = A_{96}N_9 + A_{86}N_8 + A_{76}N_7 - K_{ET1}N_6N_4 + K_{ET2}N_8N_1 \quad (2.17f)$$

$$\frac{\partial N_7}{\partial t} = -\frac{1}{\tau_{R7}}N_7 + A_{97}N_9 + A_{87}N_8 \quad (2.17g)$$

$$\frac{\partial N_8}{\partial t} = W_{98}N_9 - W_{89}N_8 - \frac{1}{\tau_{R8}}N_8 + A_{98}N_9 - K_{ET2}N_8N_1 \quad (2.17h)$$

$$\frac{\partial N_9}{\partial t} = -W_{98}N_9 + W_{89}N_8 - \frac{1}{\tau_{R9}}N_9 + K_{ET1}N_6N_4 \quad (2.17j)$$

where $A_{i,j} = \frac{\beta_{i,j}}{\tau_{Ri}}$ are the radiative decay rates; $\beta_{i,j}$ are the branching ratios; τ_{Ri} are the i -th level lifetimes; K_{ET1} and K_{ET2} are the ET coefficients; W_{NR} are the non-radiative decay rates. The emission/absorption transition rate $W_{i,j}$ for the $i \rightarrow j$ transition is defined as

$$W_{i,j}(z, t) = \frac{\sigma_{i,j}(\lambda_{p/s})}{\frac{hc_0}{\lambda_{p/s}}} [P_{p/s}^{\pm}(z, t)] \Gamma_{p/s} \quad (2.18)$$

where $\sigma_{i,j}(\lambda_{p/s})$ is the emission/absorption cross section at the wavelength $\lambda_{p/s}$ for the $i \rightarrow j$ (1-5, 5-1 and 8-9, 9-8) transitions; $\lambda_{p/s}$ is the pump/signal wavelength; h is the Plank constant; c_0 is the light speed in vacuum; P_p^{\pm} is the

forward/backward pump power; P_s^\pm is the forward/backward signal power; Γ_p/Γ_s are the overlap coefficients between the pump/signal beam and the doped area A_d . The conditions $N_1 + N_2 + N_3 + N_4 + N_5 = N_{Nd}$ and $N_6 + N_7 + N_8 + N_9 = N_{Ho}$ are imposed, where N_{Ho} and N_{Nd} are the dopant concentrations.

The power propagation for pump and signal beams is governed by the following partial differential equations

$$\frac{\partial P_p}{\partial z} = [g_p(z) - \alpha]P_p(z) \quad (2.19a)$$

$$\frac{\partial P_s^\pm}{\partial z} = \pm[g_s(z) - \alpha]P_s^\pm(z) \quad (2.19b)$$

where

$$g_p(z) = [-\sigma_{15}(\nu_p)N_1(z) + \sigma_{51}(\nu_p)N_5(z)]\Gamma_p,$$

$$g_s(z) = [-\sigma_{89}(\nu_s)N_8(z) + \sigma_{98}(\nu_s)N_9(z)]\Gamma_s,$$

are the gain coefficients for the pump and the signal, respectively, and α is the glass optical background loss.

To solve (2.19), the following boundary conditions are imposed.

$$P_p(0) = P_p^{in} \quad (2.20a)$$

$$P_s^+(0) = R_{in}P_s^-(0) \quad (2.20b)$$

$$P_s^-(L) = R_{out}P_s^+(L) \quad (2.20c)$$

where $z = 0$ and $z = L$ represent the ends of the laser cavity, P_p^{in} is the input pump power, R_{in} and R_{out} are the input and output mirror reflectivity, respectively. Initial conditions for level populations are also imposed as follows:

$$N_1(0) = N_{Nd} \quad (2.20d)$$

$$N_6(0) = N_{Ho} \quad (2.20e)$$

$$N_2(0) = N_3(0) = N_4(0) = N_5(0) = N_7(0) = N_8(0) = N_9(0) = 0 \quad (2.20f)$$

2.2.1.2 Gain-switching pulsed laser

The Ho^{3+} -doped fluorindate fiber stimulated emission at $\lambda_s = 3.92 \mu\text{m}$ can be modeled by considering a six-levels system [76], pumped at $\lambda_p = 888 \text{ nm}$. The complete level scheme, including all the main phenomena, is reported in

Fig. 2.4. The six-level model is employed instead of the five-level model proposed in [61,70] because it allows an accurate simulation. It is validated by simulating the CW laser presented in [61], obtaining results in good agreement, as reported in the next section, while the five-level model is not suitable and wrong results are obtained in the cases here investigated. Level 5I_4 and level 5I_5 degenerate and are considered as single level 4 as reported in [70-71]. The energy transfer up-conversion phenomenon between level 1 and level 3, starting from level 2, even if included in the model of [71], is here neglected since this approximation does not affect the simulation results. The other light-rare earth interactions taken into account are pump absorption, stimulated emission, radiative and nonradiative decays, excited state absorption (ESA), cross-relaxation (CR), and energy transfer up-conversion (ETU) due to the high Ho^{3+} ions concentration that will be simulated.

By following the rate equations approach [48,51], the energy level populations N_1, \dots, N_6 can be written as a nonlinear system,

$$\begin{aligned} \frac{\partial N_1}{\partial t} = & -W_{14}N_1 + W_{41}N_4 + A_{61}N_6 + A_{51}N_5 + A_{41}N_4 + A_{31}N_3 \\ & + A_{21}N_2 + KN_3^2 - W_{CR1}N_1N_4 - W_{CR2}N_1N_6 \end{aligned} \quad (2.21a)$$

$$\begin{aligned} \frac{\partial N_2}{\partial t} = & -\frac{1}{\tau_{R2}}N_2 + A_{62}N_6 + A_{52}N_5 + A_{42}N_4 + A_{32}N_3 \\ & + 2W_{CR1}N_1N_4 + W_{CR2}N_1N_6 \end{aligned} \quad (2.21b)$$

$$\begin{aligned} \frac{\partial N_3}{\partial t} = & -W_{36}N_3 + W_{63}N_6 + W_{43}N_4 - W_{34}N_3 - \frac{1}{\tau_{R3}}N_3 + A_{63}N_6 \\ & + A_{53}N_5 + A_{43}N_4 - 2KN_3^2 \end{aligned} \quad (2.21c)$$

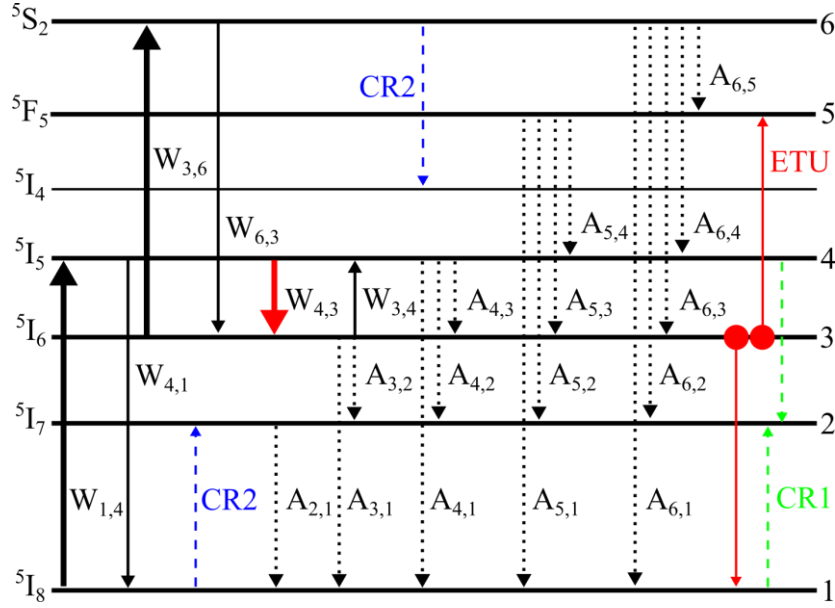


Fig. 2.4. Energy level scheme for the 6-level laser, pumped at $\lambda_p = 888 \text{ nm}$, including pump absorption (transition 1-4, bold black line) stimulated emission at $\lambda_s = 3920 \text{ nm}$ (transition 4-3, bold red line), radiative and nonradiative decays (dotted lines), excited state absorption (ESA) (transition 3-6, bold black line), cross-relaxation (CR) (blue and green dashed lines), and energy transfer up-conversion (ETU) (red solid lines).

$$\begin{aligned} \frac{\partial N_4}{\partial t} = & W_{14}N_1 - W_{41}N_4 - W_{43}N_4 + W_{34}N_3 - \frac{1}{\tau_{R4}}N_4 + A_{64}N_6 \\ & + A_{54}N_5 - W_{CR1}N_1N_4 + W_{CR2}N_1N_6 \end{aligned} \quad (2.21d)$$

$$\frac{\partial N_5}{\partial t} = -\frac{1}{\tau_{R5}}N_5 + A_{65}N_6 + KN_3^2 \quad (2.21e)$$

$$\frac{\partial N_6}{\partial t} = W_{36}N_3 - W_{63}N_6 - \frac{1}{\tau_{R6}}N_6 - W_{CR2}N_1N_6 \quad (2.21f)$$

where $A_{i,j} = \frac{\beta_{i,j}}{\tau_{Ri}}$ take into account radiative and non-radiative decays, $\beta_{i,j}$ are the branching ratios, τ_{Ri} are the i -th level lifetimes, K is the ETU rate, and W_{CR1} and W_{CR2} are the cross-relaxation transition rates. The condition $N_1 + N_2 + N_3 + N_4 + N_5 + N_6 = N_{Ho}$ is considered, where N_{Ho} is the dopant concentration. The transition rate $W_{i,j}$ for the $i \rightarrow j$ transition is defined as

$$W_{i,j}(z, t) = \frac{\sigma_{i,j}(\lambda_{p/s})}{\frac{hc_0}{\lambda_{p/s}}} [P_p(z, t)] i_{p/s}(x, y) \quad (2.22)$$

where $\sigma_{i,j}(\lambda_{p/s})$ is the cross section at the wavelength $\lambda_{p/s}$ for the $i \rightarrow j$ transition, h is the Plank constant, c_0 is the light speed in vacuum, $\lambda_{p/s}$ is the pump/signal wavelength, P_p^\pm is the forward/backward pump power, P_s^\pm is the forward/backward signal power, i_p and i_s are the normalized transverse intensity profiles, i.e., the squared modulus of the electromagnetic field, of pump and signal beams, respectively.

The power propagation for pump and signal beams is considered by the following partial differential equations

$$\frac{\partial P_p}{\partial z} + \frac{1}{v_g^p} \frac{\partial P_p}{\partial t} = [g_p(z, t) - \alpha] P_p(z, t) \quad (2.23a)$$

$$\frac{\partial P_s^\pm}{\partial z} \pm \frac{1}{v_g^s} \frac{\partial P_s^\pm}{\partial t} = \pm [g_s(z, t) - \alpha] P_s^\pm(z, t) \pm 2h\nu_s B_{ase} \sigma_{43} n_{4s}(z, t) \quad (2.23b)$$

where

$$g_p(z, t) = -\sigma_{14}(\nu_p) n_{1p}(z, t) + \sigma_{41}(\nu_p) n_{4p}(z, t) - \sigma_{36}(\nu_p) n_{3p}(z, t) + \sigma_{63}(\nu_p) n_{6p}(z, t),$$

$$g_s(z, t) = -\sigma_{34}(\nu_s) n_{3s}(z, t) + \sigma_{43}(\nu_s) n_{4s}(z, t),$$

are the gain coefficients for the pump and the signal, respectively, α is the glass optical loss, v_g^p and v_g^s are the group velocity for the pump and the signal, respectively, and B_{ase} is the equivalent noise bandwidth for the Amplified Spontaneous Emission (ASE), $n_{i,p/s}$ are the overlap integrals over the rare earth-doped region Ω_d between the i -th level population distribution $N_i(x, y, z, t)$ and the pump/signal optical mode intensity $i_{p/s}(x, y)$ and they are defined as follows.

$$n_{1p}(z, t) = \int_{\Omega_d} N_1(x, y, z, t) i_p(x, y) dx dy \quad (2.24a)$$

$$n_{3p}(z, t) = \int_{\Omega_d} N_3(x, y, z, t) i_p(x, y) dx dy \quad (2.24b)$$

$$n_{4p}(z, t) = \int_{\Omega_d} N_4(x, y, z, t) i_p(x, y) dx dy \quad (2.24c)$$

$$n_{6p}(z, t) = \int_{\Omega_d} N_6(x, y, z, t) i_p(x, y) dx dy \quad (2.24d)$$

$$n_{3s}(z, t) = \int_{\Omega_d} N_3(x, y, z, t) i_s(x, y) dx dy \quad (2.24e)$$

$$n_{4s}(z, t) = \int_{\Omega_d} N_4(x, y, z, t) i_s(x, y) dx dy \quad (2.24f)$$

These coefficients allow to take into account the overlapping strength between the spatial distribution of ion populations and the electromagnetic field. To solve (2.23), the following initial conditions are imposed.

$$P_p(0, t) = P_p^{in}(t) \quad (2.25a)$$

$$P_s^+(0, t) = R_1 P_s^-(0, t) \quad (2.25b)$$

$$P_s^-(L, t) = R_2 P_s^+(L, t) \quad (2.25c)$$

where $z = 0$ and $z = L$ represent the ends of the laser cavity, $P_{p0}(t)$ is the input pump power, R_1 and R_2 are the first and second mirror reflectivity, respectively. Time initial conditions are also considered as follows.

$$N_1(x, y, z, 0) = N_{tot}(x, y, z) \quad (2.25d)$$

$$N_2(x, y, z, 0) = N_3(x, y, z, 0) = N_4(x, y, z, 0) = N_5(x, y, z, 0) = \\ = N_6(x, y, z, 0) = 0 \quad (2.25e)$$

$$P_p(z, 0) = P_s^+(z, 0) = P_s^-(z, 0) = 0 \quad (2.25f)$$

To evaluate the time evolution of the generated pulses, the output power is defined as

$$P_s^{out}(t) = [1 - R_2(v_s)] P_s^+(L, t) \quad (2.26)$$

3 Low-cost air-filled SIW multi-layer array antenna at mm-waves

3.1 Introduction

In this chapter, a low-cost multilayer air-filled substrate integrated waveguide (SIW) array antenna has been designed to work at frequency $f = 60 \text{ GHz}$ in the unlicensed 5G band. The SIW technology is exploited as an alternative to higher cost fabrication techniques. The feeding network and the slotted cavities are almost completely empty in order to minimize the power losses. To this aim, a preliminary investigation on the SIW channel waveguide has been performed. A broadside maximum gain $G = 19.8 \text{ dB}$ with efficiency $\eta = 94\%$ has been simulated for an array composed by 4×4 radiating slots. The antenna bandwidth is $BW = 8.0 \text{ GHz}$, corresponding a percent bandwidth $BW_{\%} \approx 13.3\%$. The array composed by 8×8 radiating slots is characterized by $G = 24.3 \text{ dB}$, $\eta = 85\%$, $BW = 8.0 \text{ GHz}$, $BW_{\%} \approx 13.3\%$. The antenna will be constructed and characterized at the Institut d'Electronique et des Technologies du numéRique (IETR) in Rennes (France).

3.2 Power losses investigation

Before designing the multilayer antenna, a power loss investigation is performed to minimize dielectric losses of the partially-air-filled SIW. The chosen dielectric substrates are Rogers RT/Duroid 5880 ($\epsilon_r = 2.2$, $\tan\delta = 0.0009$), with the commercial thicknesses reported in Table 3.I. The investigation is performed by simulating a partially-air-filled substrate integrated waveguide and comparing its dielectric losses to those of a traditional SIW. The investigated geometry is illustrated in Fig. 3.1, whereas the list of the geometrical parameters is reported in Table 3.I. The parameters regard the basic structure that will be considered for the antenna array.

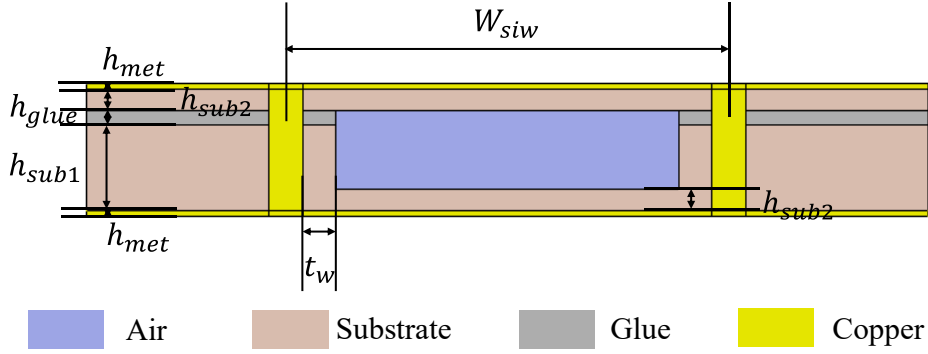


Fig. 3.1. Geometry of the considered air-filled SIW.

TABLE 3.I
GEOMETRICAL PARAMETERS OF PARTIALLY-AIR-FILLED SIW

Symbol	Value	Description
W_{siw}	3.1 mm	Distance between two parallel vias
h_{met}	0.035 mm	Metal thickness
h_{sub1}	0.508 mm	Substrate 1 thickness
h_{sub2}	0.127 mm	Substrate 2 thickness
h_{glue}	0.08 mm	Prepreg glue thickness
t_w	0.2 mm	Thickness between metallic vias and air portion

The air-filled SIW is obtained considering two substrate laminates of thicknesses $h_{sub1} = 0.508 \text{ mm}$ and $h_{sub2} = 0.127 \text{ mm}$, glued with the Taconic fastRiseTM 27 prepreg ($\epsilon_r = 2.72$, $\tan\delta = 0.0017$). Simulations are performed by employing CST Microwave Studio Suite. The thicker substrate (i.e., the one with thickness h_{sub1}) is partially removed to obtain the air waveguide. To this aim, different techniques such as UV ablation, mechanical milling, and chemical etching can be employed. The metallic layers have thickness $h_{met} = 0.035 \text{ mm}$ and are made of copper ($\sigma = 5.8 \times 10^7 \text{ S/m}$). The SIW is designed starting from semi-empirical formulas, reported in paragraph 2.1. The investigation regards the optimization of the thickness between metallic vias and air volume, depending on t_w to parity of the other geometrical parameters, see Fig. 3.1.

Fig. 3.2 shows the dielectric (dash-dotted curve), metallic (dotted curve), and total (solid curve) percentage losses as a function of the thickness t_w at frequency $f = 60 \text{ GHz}$. In particular, $t_w = 0.0 \text{ mm}$ represents the total-air-filled SIW, while $t_w = 1.5 \text{ mm}$ corresponds to the full dielectric traditional SIW. The thickness $t_w = 0.05 \text{ mm}$ is considered as a fabrication constraint of typical milling. Therefore, $t_w = 0.1 \text{ mm}$ can be chosen as the optimized value, allowing

total losses reduction from about $\alpha_t = 27.60\%$, for full substrate case, to $\alpha_t = 13.85\%$ and it being within the fabrication tolerance. This value is considered optimized for the antenna design, too. To conclude, the optimized SIW should be practically empty or air-filled. Table 3.II lists all the simulated values.

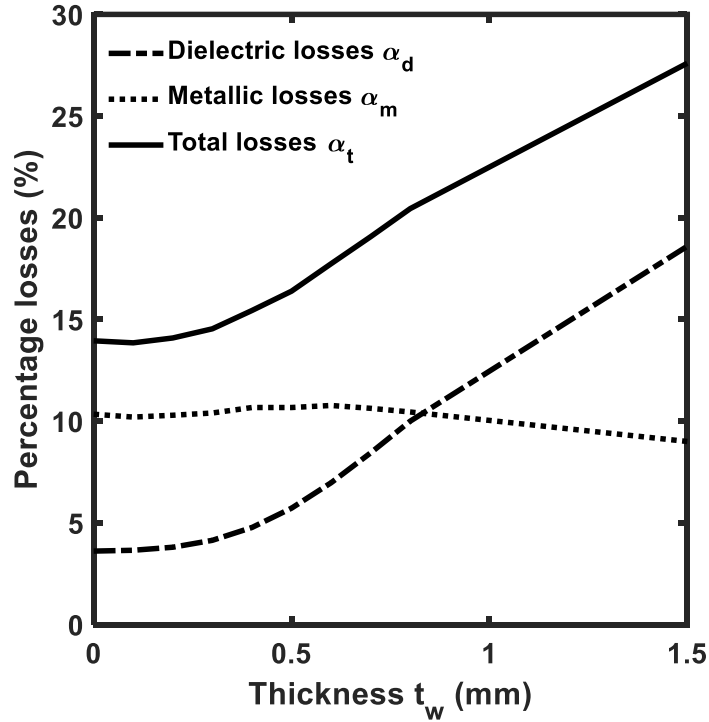


Fig. 3.2. Dielectric (dash-dotted curve), metallic (dotted curve), and total (solid curve) percentage losses as a function of the thickness t_w at frequency $f = 60$ GHz.

TABLE 3.II
DIELECTRIC, METALLIC, AND TOTAL PERCENTAGE LOSSES FOR DIFFERENT
VALUES OF t_w AT FREQUENCY $f = 60 \text{ GHz}$

Thickness t_w	Dielectric losses α_d	Metallic losses α_m	Total losses α_{tot}
0.0 mm (totally-air-filled)	3.61 %	10.34 %	13.95 %
0.1 mm	3.65 %	10.20 %	13.85 %
0.2 mm	3.80 %	10.29 %	14.09 %
0.3 mm	4.14 %	10.40 %	14.54 %
0.4 mm	4.77 %	10.67 %	15.44 %
0.5 mm	5.72 %	10.67 %	16.40 %
0.6 mm	6.97 %	10.77 %	17.74 %
0.7 mm	8.44 %	10.63 %	19.07 %
0.8 mm	10.00 %	10.45 %	20.45 %
1.5 mm (full substrate)	18.60 %	9.00 %	27.60 %

3.3 Antenna design

3.3.1 Elementary 2×2 slot sub-array

The design starts from the elementary 2×2 slot sub-array, shown in Fig. 3.3. The antenna is obtained by considering five layers, as shown in the exploded view of Fig. 3.4. It is composed of two-level regions, with lateral walls designed as for the air-filled SIW reported in paragraph 3.2, in term of metalized vias sizes and thickness t_w .

The antenna is fed by an air-filled SIW, coupled with the cavity by means of a coupling aperture. Layer 01 is the ground plane; Layer 02 hosts the metalized vias constituting the lateral walls of the feeding waveguide; Layer 03 includes the coupling aperture between the waveguide and the cavity; Layer 04 hosts the metalized vias constituting the lateral walls of the cavity; the metallic Layer 05 includes the four radiating slots.

Fig. 3.5 reports the main geometric parameters of the elementary 2×2 slot sub-array. The nominal values are identified with preliminary simulations in order to obtain the operation at $f = 60 \text{ GHz}$ and are reported in Table 3.III. The 2×2 slot sub-array has been optimized as a tradeoff to obtain the maximum of the bandwidth BW , gain G , and efficiency η .

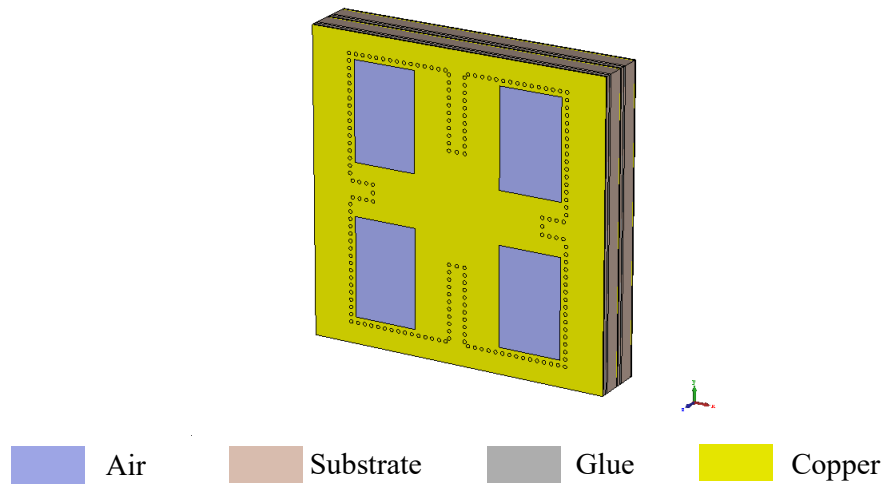


Fig. 3.3. Geometry of elementary 2×2 slot sub-array.

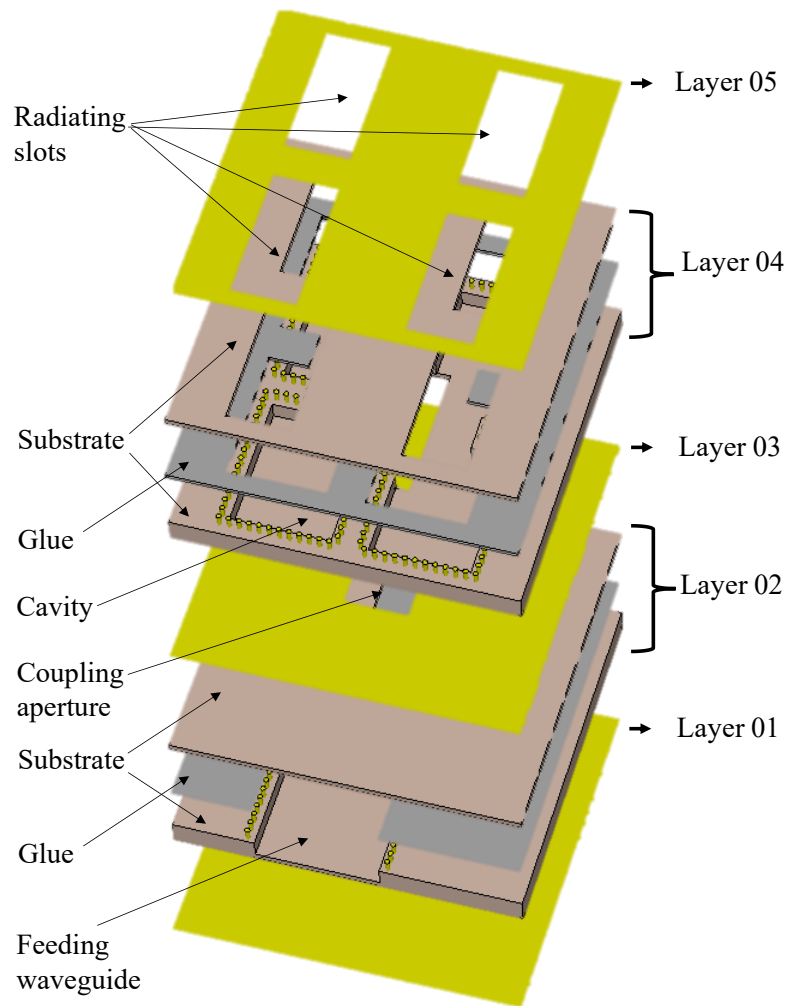


Fig. 3.4. Exploded view of the 2×2 slot sub-array layers.

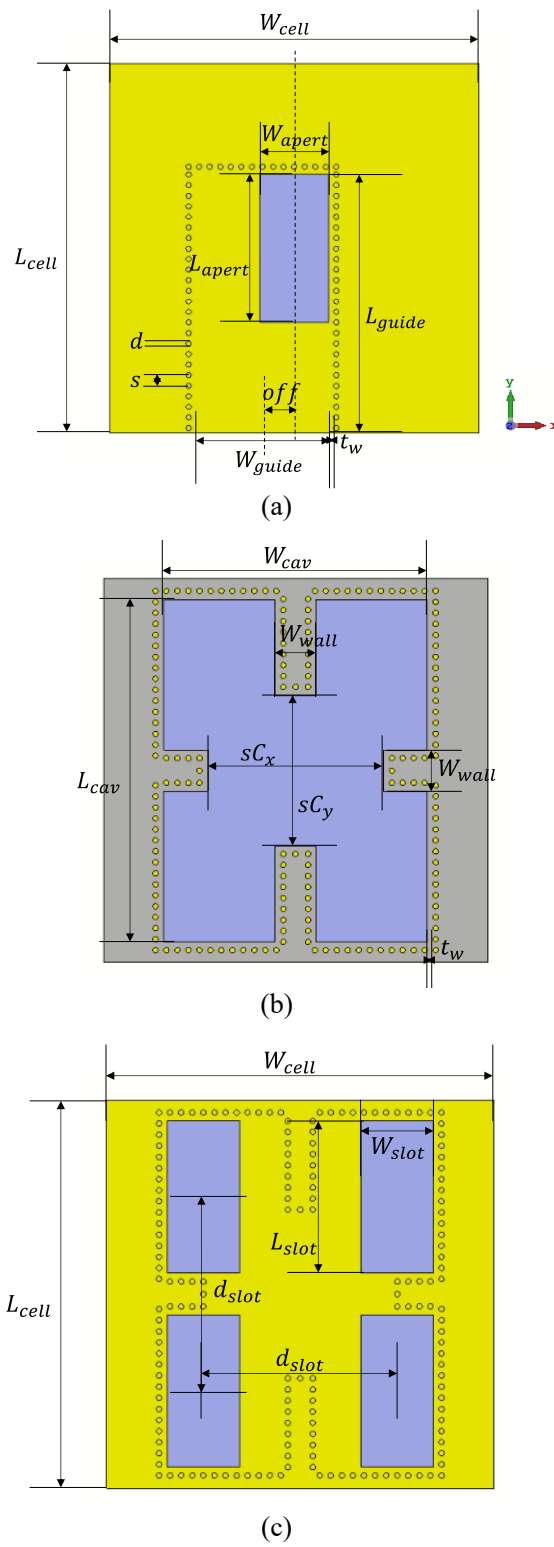


Fig. 3.5. Main geometrical parameters of the 2×2 slot sub-array for (a) Layer 03, (b) Layer 04, (c) Layer 05.

TABLE 3.III
NOMINAL GEOMETRICAL PARAMETERS OF THE 2×2 SLOT SUB-ARRAY

Symbol	Nominal value	Description
W_{cell}	7.6 mm	Elementary sub-array width
L_{cell}	7.6 mm	Elementary sub-array length
W_{cav}	5.3 mm	Cavity width
L_{cav}	6.6 mm	Cavity length
W_{guide}	2.5 mm	Feeding line width
L_{guide}	5.05 mm	Feeding line length
W_{apert}	1 mm	Coupling aperture width
L_{apert}	2.5 mm	Coupling aperture length
W_{slot}	1.5 mm	Radiating slot width
L_{slot}	2.8 mm	Radiating slot length
d_{slot}	3.8 mm	Radiating slot distance
sC_x	4 mm	Cavity wall distance along x -axis
sC_y	3 mm	Cavity wall distance along y -axis
W_{wall}	0.75 mm	Cavity wall width
L_{off}	0.75 mm	Offset of the feeding line from the sub-array center
s	0.2 mm	Distance between two adjacent vias
d	0.1 mm	Vias diameter
t_w	0.1 mm	Thickness between metallic vias and air portion

In first place, the optimization regards the coupling aperture of Layer 03, without considering Layer 04 (cavity) and Layer 05 (radiating slots). Once obtained the best impedance matching in the widest frequency bandwidth BW , the cavity and radiating slots have been added. The whole structure has been again optimized, by varying the radiating slot length L_{slot} , the radiating slot width W_{slot} , the cavity wall distance along x -axis sC_x , and the cavity wall distance along y -axis sC_y .

3.3.1.1 Optimization of the coupling aperture

As shown in Fig. 3.5(a), the coupling aperture of Layer 03 is placed at the center of the elementary sub-array, while the feeding waveguide is designed with an offset L_{off} from the center, in order to guarantee the best field coupling [5] as described below in a). Moreover, the coupling aperture is placed at the end

of the feeding line [5]. By changing W_{apert} , to parity of feeding waveguide, L_{off} is changed accordingly.

Fig. 3.6 shows the modulus of the scattering parameter S_{11} as a function of the frequency f for different values of the coupling aperture width W_{apert} of Layer 03. The impedance matching improves, and the bandwidth BW enlarges as the coupling aperture width W_{apert} increases, until $W_{apert} = 1.3 \text{ mm}$ (dot-dashed line). For $W_{apert} = 1.4 \text{ mm}$, the bandwidth BW decreases and the minimum of the scattering parameter modulus $|S_{11}|$ shifts towards higher frequencies. The optimized aperture is $W_{apert} = 1.3 \text{ mm}$ and the offset is $L_{off} = 0.8 \text{ mm}$.

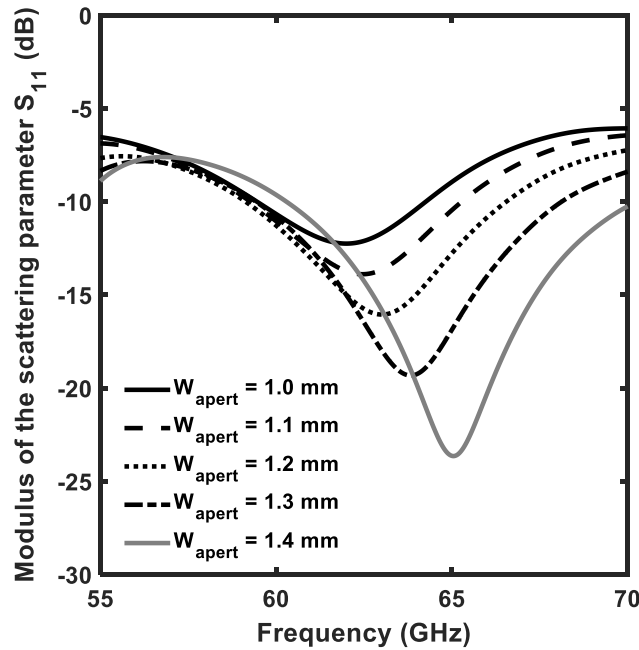


Fig. 3.6. Modulus of the scattering parameter S_{11} as a function of the frequency f for different values of the coupling aperture width W_{apert} .

Fig. 3.7 shows the modulus of the scattering parameter S_{11} as a function of the frequency f for different values of the coupling aperture length L_{apert} . The impedance matching improves as the aperture length L_{apert} increases until $L_{apert} = 2.8 \text{ mm}$ (dotted line). Since the coupling aperture is designed to be at the edge of the feeding line, also the feeding guide length L_{guide} varies accordingly with the coupling aperture length L_{apert} . The optimized values are $L_{apert} = 2.8 \text{ mm}$ and $L_{guide} = 5.2 \text{ mm}$.

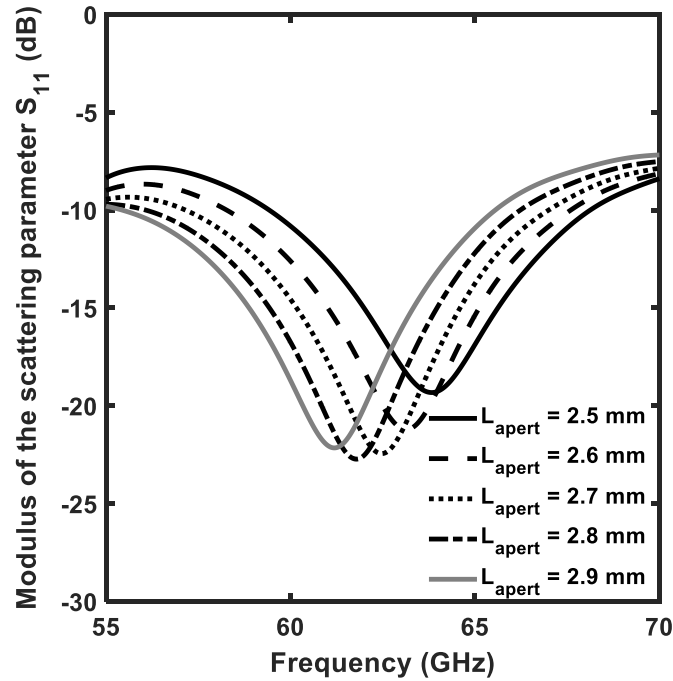


Fig. 3.7. Modulus of the scattering parameter S_{11} as a function of the frequency f for different values of the coupling aperture length L_{apert} .

3.3.1.2 Optimization of the cavity wall distances

The cavity has been optimized by varying the cavity wall distance along x -axis, sC_x , and along y -axis, sC_y .

Fig. 3.8 shows the modulus of the scattering parameter S_{11} as a function of the frequency f for different values of the cavity wall distance along x -axis, sC_x . The impedance matching improves and shifts to higher values when the cavity walls become closer. The chosen value is $sC_x = 2.8$ mm because it allows the best impedance matching and maximizes the bandwidth BW .

Fig. 3.9 shows the modulus of the scattering parameter S_{11} as a function of the frequency f for different values of the cavity wall distance along y -axis, sC_y . As it reduces, the bandwidth BW slightly shifts towards higher frequencies. The optimized value is $sC_y = 3.6$ mm, ensuring good impedance matching at $f = 60$ GHz and largest bandwidth BW .

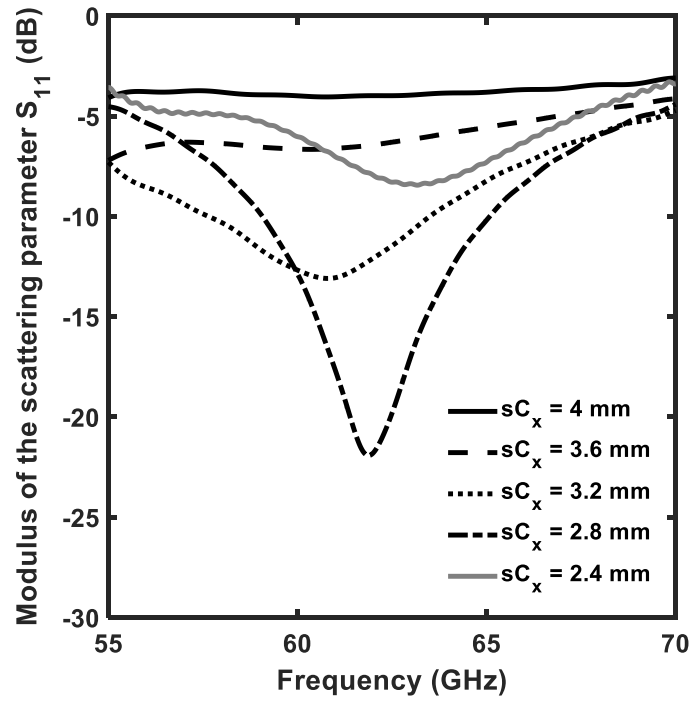


Fig. 3.8. Modulus of the scattering parameters S_{11} (solid curves) and S_{21} (dotted curves) as a function of frequency f for different values of the slot width W_{slot} .

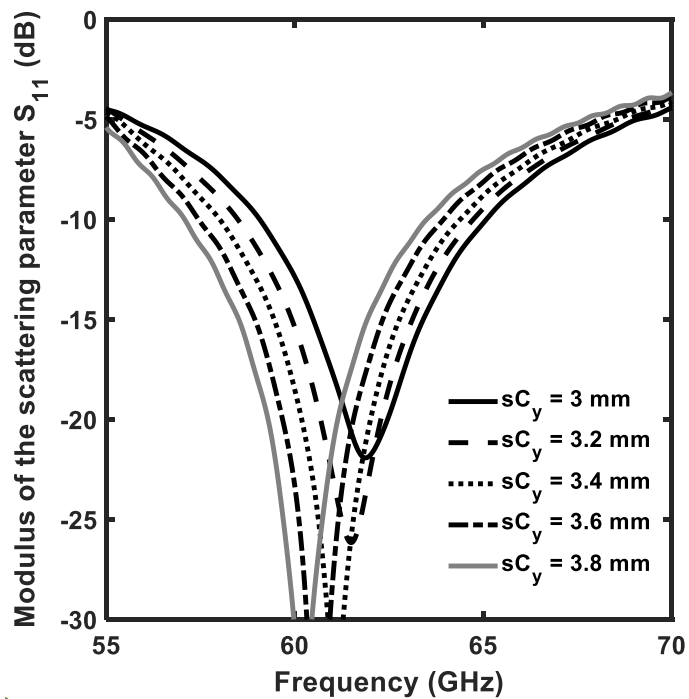


Fig. 3.9. Modulus of the scattering parameter S_{11} as a function of the frequency f for different values of the cavity wall distance along y -axis sC_y .

3.3.1.3 Optimization of the radiating slot

To refine the whole structure, the radiating slot length, L_{slot} , and the radiating slot width W_{slot} have been optimized.

Fig. 3.10 shows the modulus of the scattering parameter S_{11} as a function of the frequency f for different values of the radiating slot length, L_{slot} .

The impedance matching shifts to lower frequencies for bigger values of the radiating slot length L_{slot} and the bandwidth BW enlarges. The largest, i.e., optimized, value to keep the suitable distance between slot d_{slot} (geometrical constraint) is $L_{slot} = 3.1 \text{ mm}$ (dash-dotted curve).

Fig. 3.11 shows the modulus of the scattering parameter S_{11} as a function of the frequency f for different values of the radiating slot width, W_{slot} . The impedance matching shifts to higher frequencies as the radiating slot width increases, while the largest bandwidth BW is obtained for $W_{slot} = 1.7 \text{ mm}$ (dotted curve).

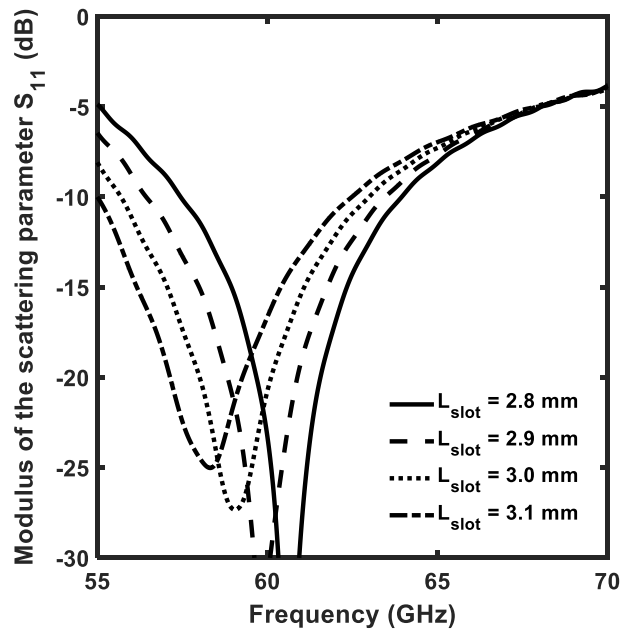


Fig. 3.10. Modulus of the scattering parameter S_{11} as a function of the frequency f for different values of the radiating slot length L_{slot} .

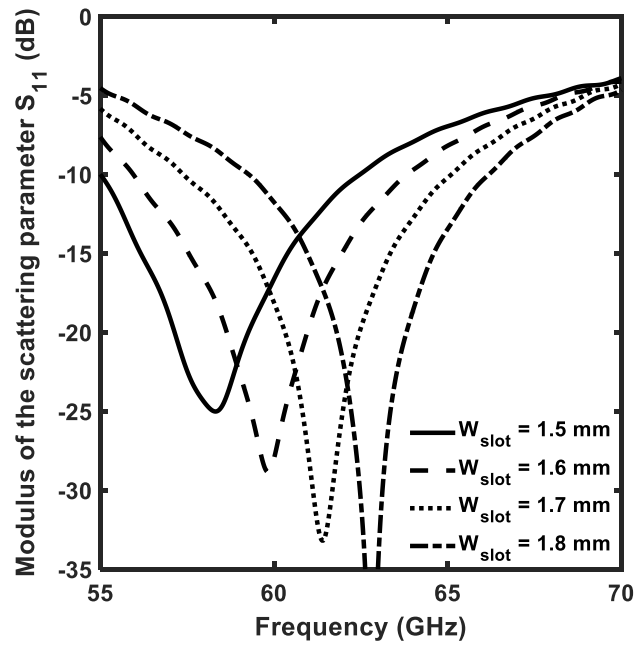


Fig. 3.11. Modulus of the scattering parameter S_{11} as a function of the frequency f for different values of the radiating slot width W_{slot} .

3.3.1.4 Optimized geometry

After all the investigation, the optimized values of the geometrical parameters are reported in Table 3.IV.

TABLE 3.IV
OPTIMIZED GEOMETRICAL PARAMETERS OF THE 2×2 SLOT SUB-ARRAY

Symbol	Optimized value	Description
W_{cell}	7.6 mm	Elementary sub-array width
L_{cell}	7.6 mm	Elementary sub-array length
W_{cav}	5.5 mm	Cavity width
L_{cav}	6.9 mm	Cavity length
W_{guide}	2.5 mm	Feeding line width
L_{guide}	5.2 mm	Feeding line length
W_{apert}	1.3 mm	Coupling aperture width
L_{apert}	2.8 mm	Coupling aperture length
W_{slot}	1.7 mm	Radiating slot width
L_{slot}	3.1 mm	Radiating slot length
d_{slot}	3.8 mm	Radiating slot distance
sC_x	2.8 mm	Cavity wall distance along x -axis
sC_y	3.6 mm	Cavity wall distance along y -axis
W_{wall}	0.75 mm	Cavity wall width
L_{off}	0.6 mm	Offset of the feeding line from the sub-array center
s	0.2 mm	Distance between two adjacent vias
d	0.1 mm	Vias diameter
t_w	0.1 mm	Thickness between metallic vias and air portion

3.3.2 4×4 slot sub-array

The 4×4 slot sub-array has been obtained considering four elementary 2×2 slot sub-array, as shown in Fig. 3.3. The feeding of the coupling apertures is designed via a H-junction, shown in Fig. 3.12, reporting its main dimensions. Their starting values are listed in Table 3.V. Couples of irises are added to increase bandwidth BW and efficiency η [6]. Optimization of iris distance w_f and the divider length l_f allows to reach best performances, as reported below.

TABLE 3.V
GEOMETRICAL PARAMETERS OF THE FEEDING H-JUNCTION 4 × 4 SLOT ARRAY

Symbol	Nominal value	Description
W_w	0.5 mm	Dividing wall width
l_f	1.2 mm	Dividing wall length
w_{iris}	0.5 mm	Iris width
w_f	2.3 mm	Iris distance

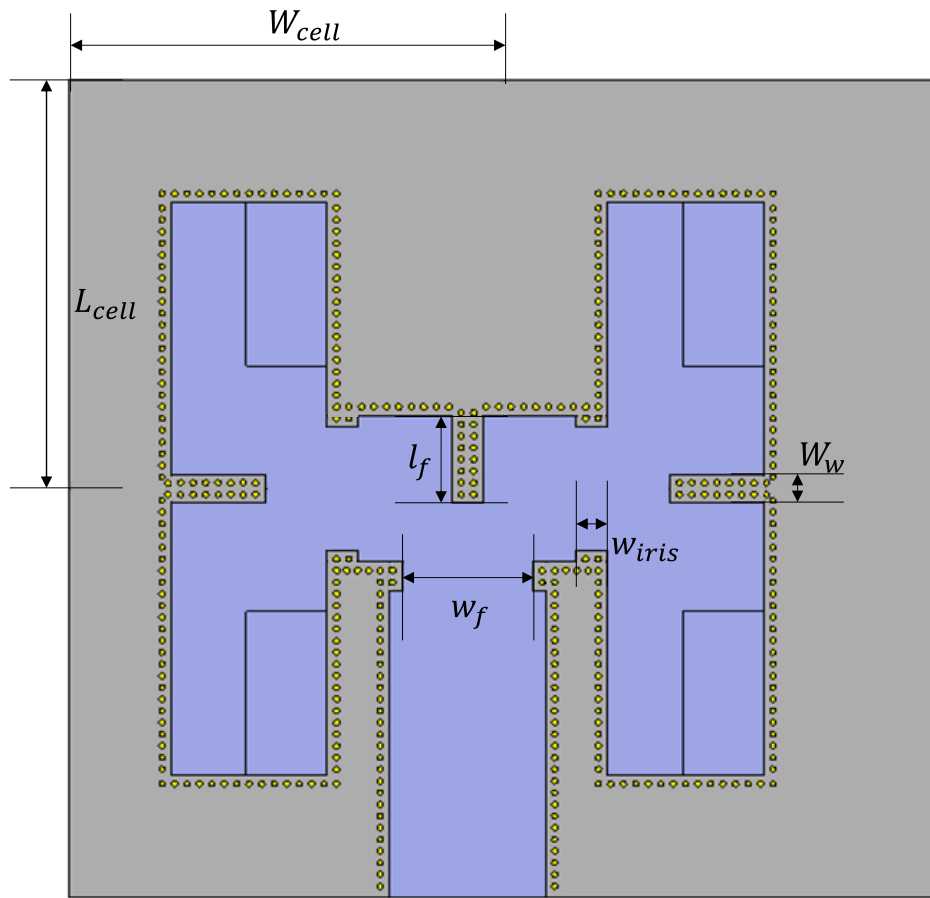


Fig. 3.12. Geometry of the feeding H-junction of the 4 × 4 slot array.

Fig. 3.13 shows the modulus of the scattering parameter S_{11} as a function of the frequency f for different values of the septum length l_f . As it increases, the first minimum of the scattering parameter modulus $|S_{11}|$ shifts towards higher frequencies and the bandwidth BW enlarges until the optimized value $l_f = 1.2 \text{ mm}$ (dotted curve). For $l_f > 1.2 \text{ mm}$ (dash-dotted curve and grey curve) the bandwidth BW is reduced.

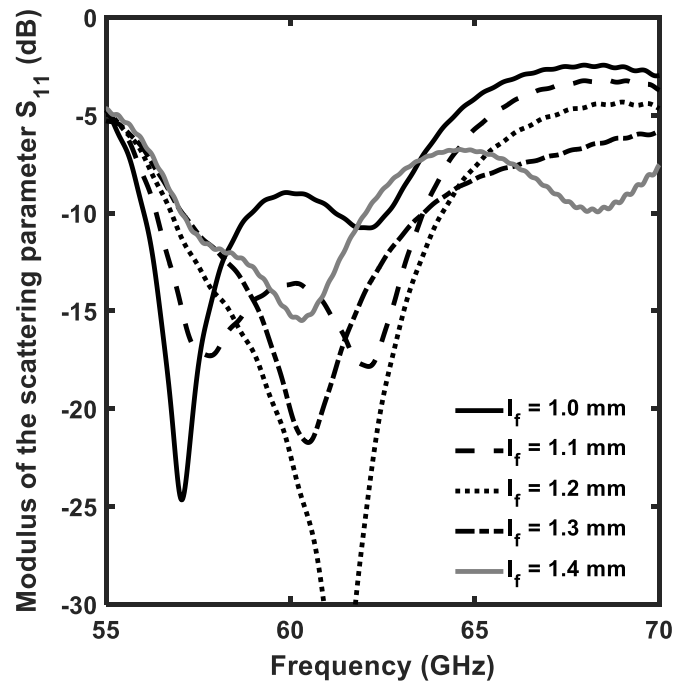


Fig. 3.13. Modulus of the scattering parameter S_{11} as a function of the frequency f for different values of divider length l_f .

Fig. 3.14 shows the modulus of the scattering parameter S_{11} as a function of the frequency f for different values of the iris distance w_f . As it reduces, also the bandwidth BW enlarges, but the minimum of the scattering parameter modulus $|S_{11}|$. The value $w_f = 2.05$ mm (solid curve) is chosen as the optimal, because it allows the best trade-off between the large bandwidth BW and the good impedance matching.

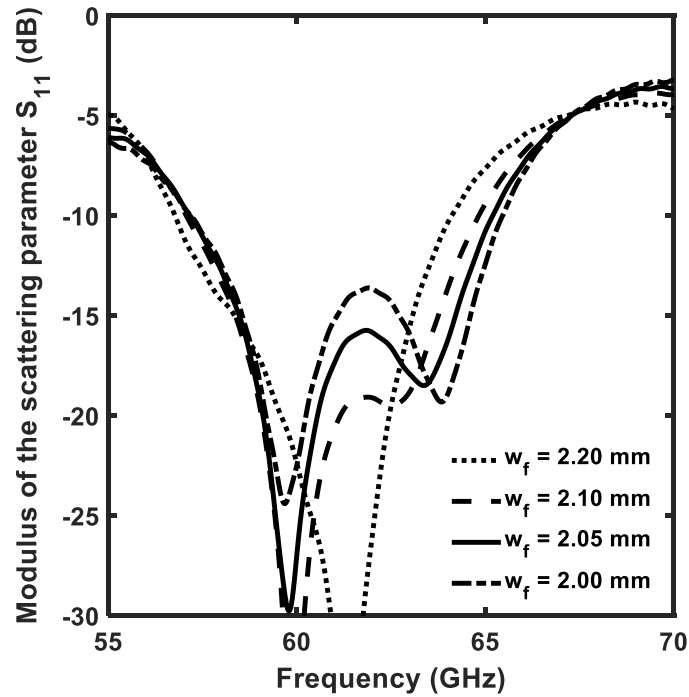


Fig. 3.14. Modulus of the scattering parameter S_{11} as a function of the frequency f for different values of the iris distance w_f .

Fig. 3.15 shows the modulus of the scattering parameter S_{11} as a function of the frequency f with optimized irises (solid line) and without irises (dash line). The bandwidth BW is increased, from about $BW = 1 \text{ GHz}$ to $BW = 8 \text{ GHz}$, and shifted towards the desired frequencies when irises are inserted.

The simulated gain is $G = 19.8 \text{ dB}$, with efficiency $\eta = 94 \%$, and optimized bandwidth $BW = 8 \text{ GHz}$, corresponding to a percentage bandwidth $BW_{\%} = 13.3\%$.

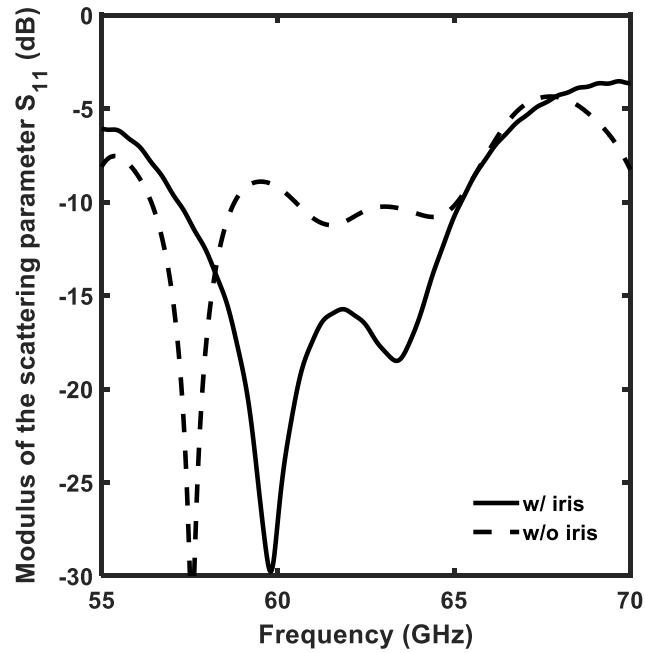


Fig. 3.15. Modulus of the scattering parameter S_{11} as a function of the frequency f , with (solid line) and without (dash line) irises.

Table 3.VI reports the optimized values of the geometrical parameters of the H-junction.

TABLE 3.VI
GEOMETRICAL PARAMETERS OF THE FEEDING H-JUNCTION 4×4 SLOT ARRAY

Symbol	Nominal value	Description
W_w	0.5 mm	Dividing wall width
l_f	1.2 mm	Dividing wall length
w_{iris}	0.5 mm	Iris width
w_f	2.05 mm	Iris distance

It is worthy to observe that, for the optimized 4×4 slot, the thickness $t_w = 0.1$ mm allows total losses reduction from about $\alpha_t = 10\%$, for full substrate case, to $\alpha_t = 5.7\%$.

3.3.3 8×8 slot array

The 8×8 slot array is obtained by composing four 4×4 slot sub-arrays. The complete feeding network is shown in Fig. 3.16. In this case, $w_f = 2.1$ mm is the optimized iris distance while all the other parameters are maintained. This

slight change with respect to the 4×4 has allowed to further widen the bandwidth BW .

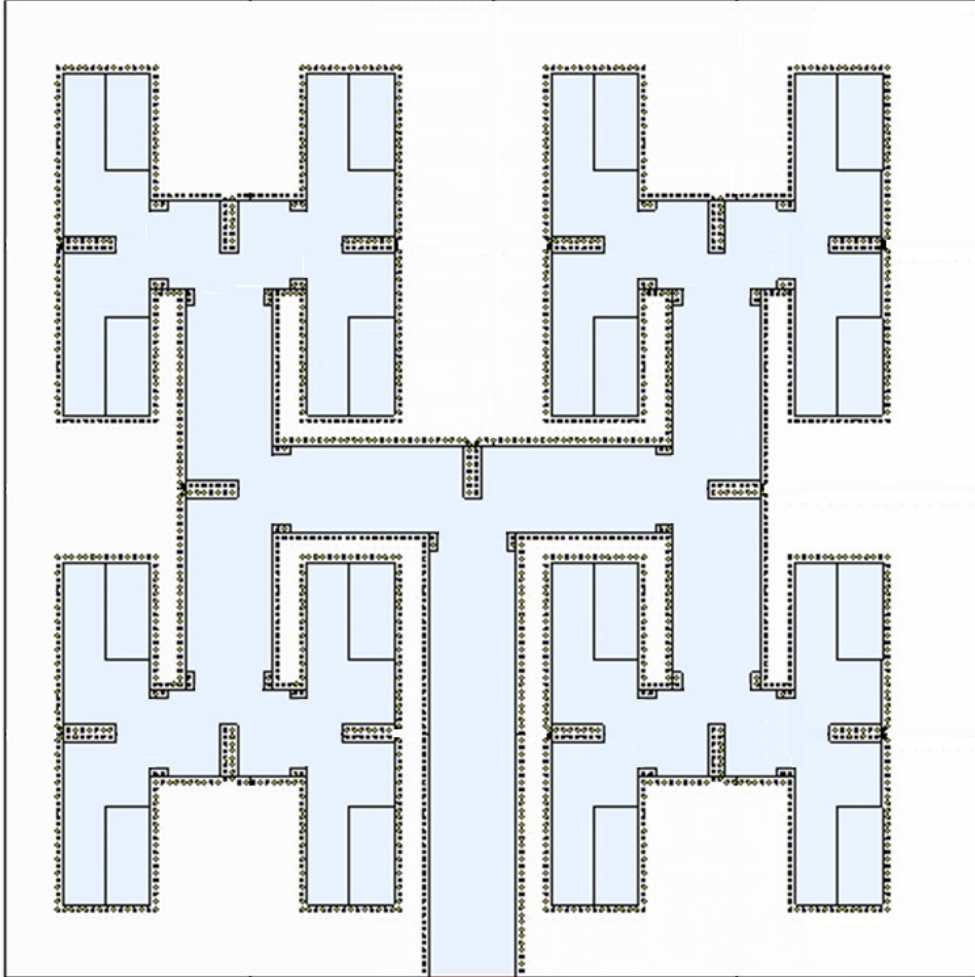


Fig. 3.16. Geometry of the feeding network for the 8×8 slot array.

Fig. 3.17 shows the modulus of the scattering parameter S_{11} as a function of the frequency f , for the optimized 8×8 slot array antenna. It exhibits a bandwidth $BW = 8.4 \text{ GHz}$, corresponding to a percentage bandwidth $BW_{\%} = 14 \%$.

Fig. 3.18 shows the gain as a function of the angle θ , for $\varphi = 0^\circ$ and $\varphi = 90^\circ$, at frequency $f = 60 \text{ GHz}$. The maximum gain in the broadside direction is $G = 25.3 \text{ dB}$ and efficiency $\eta = 88\%$.

For the 8×8 slot, the thickness $t_w = 0.1 \text{ mm}$ allows total losses reduction from about $\alpha_t = 19.6\%$, for full substrate case, to $\alpha_t = 11.4\%$.

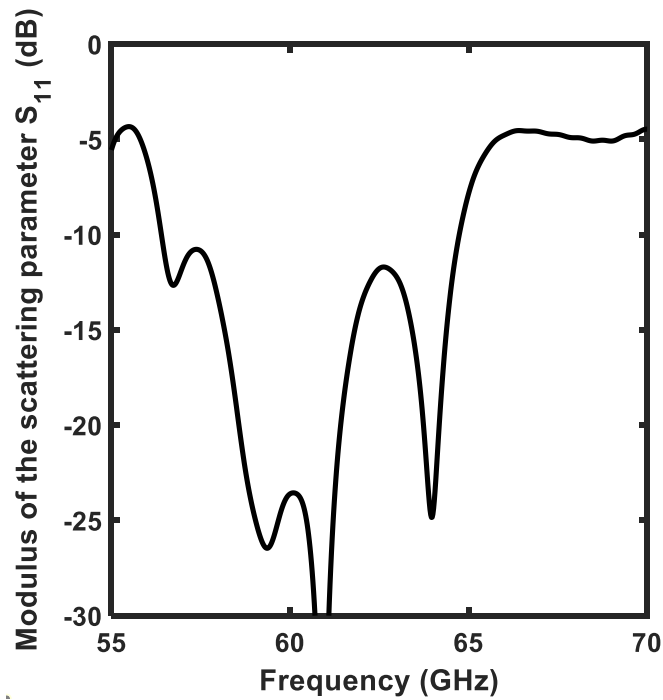


Fig. 3.17. Modulus of the scattering parameter S_{11} as a function of the frequency f , for the optimized 8×8 slot array.

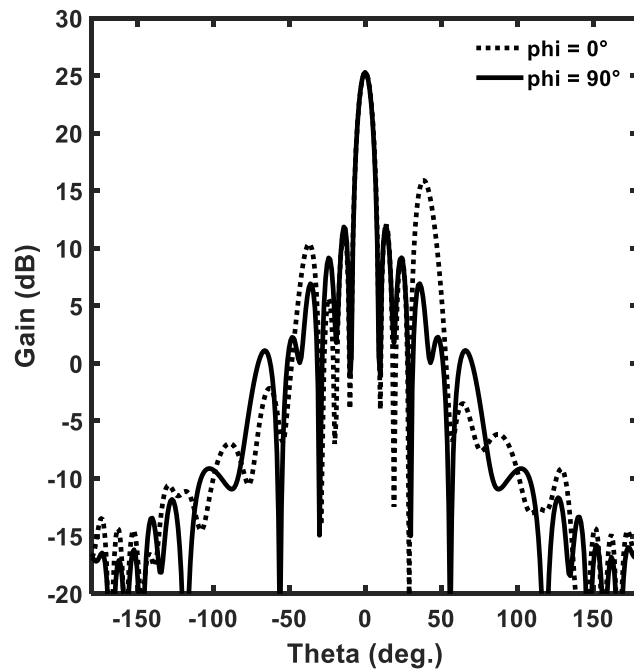


Fig. 3.18. Gain G as a function of the angle θ , for $\phi = 0^\circ$ (dotted line) and $\phi = 90^\circ$ (solid line), at frequency $f = 60$ GHz.

3.4 Connector to air-filled SIW transition

In order to feed the antenna with a coaxial connector, a grounded coplanar waveguide (GCPW) to SIW transition has been designed and optimized.

3.4.1 Connector

The chosen connector is Southwest Microwave 1892-04A-9, working from DC to $f = 67 \text{ GHz}$, shown in Fig. 3.19. It has input impedance $Z_0 = 50 \Omega$.



Fig. 3.19. Connector Southwest Microwave 1892-04A-9 [85].

It is a removable connector that does not need soldering and will be employed at IETR for the antenna characterization. It has been simulated in CST Studio software with the GCPW transition to ensure an accurate design.

Its CST scheme is shown in Fig. 3.20.

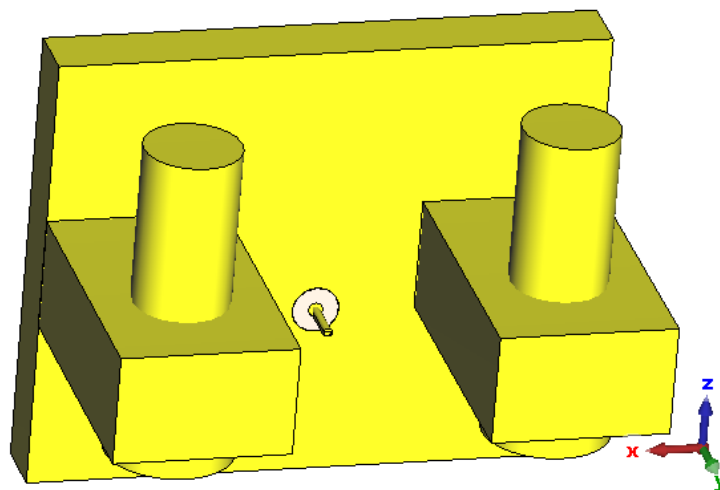


Fig. 3.20. Scheme of the connector Southwest Microwave 1892-04A-9 in CST Studio.

3.4.2 Connector-to-GCPW transition

The transition from the connector to the GCPW is shown in Fig. 3.21, reporting the main geometrical parameters. The optimized values are reported in Table 3.VII.

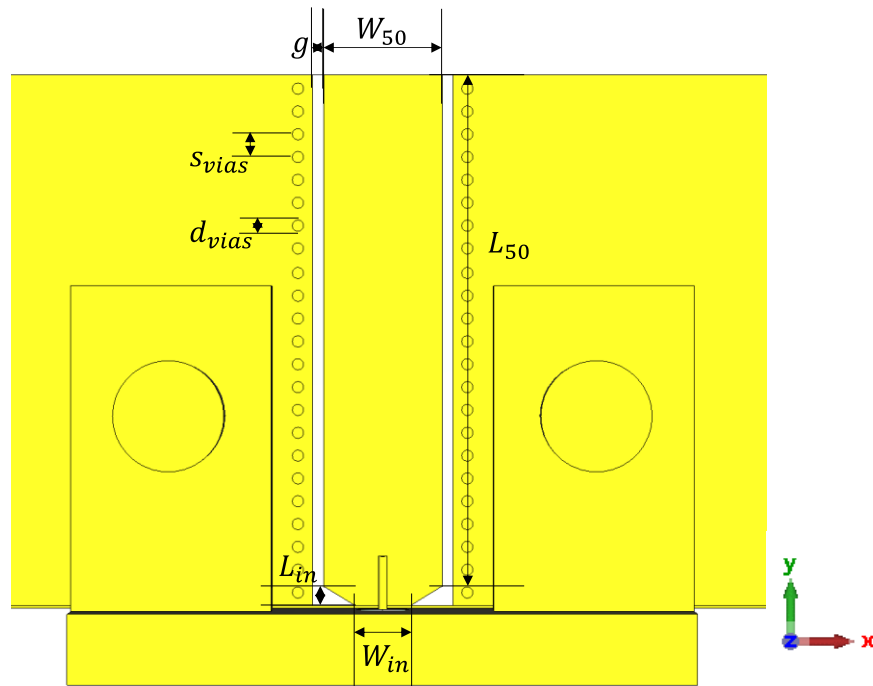


Fig. 3.21. Scheme of the Connector-to-GCPW transition.

TABLE 3.VII
OPTIMIZED GEOMETRICAL PARAMETERS OF THE CONNECTOR-TO-GCPW TRANSITION.

Symbol	Value	Description
W_{in}	0.96 mm	Input width
L_{in}	0.29 mm	Input length
W_{50}	1.5 mm	Width of line at 50 Ω
L_{50}	2 mm	Length of line at 50 Ω
g	0.2 mm	GCPW gap
s_{vias}	0.4 mm	Center-center distance between vias
d_{vias}	0.2 mm	Vias diameter

3.4.3 Wide GCPW-to-small GCPW transition

The transition from wide GCPW to small GCPW is shown in Fig. 3.22, reporting the main geometrical parameters. The optimized values are reported in Table 3.VIII.

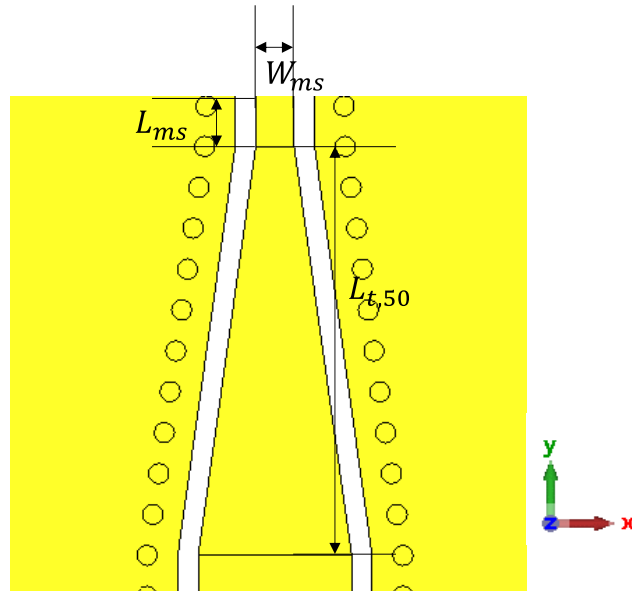


Fig. 3.22. Scheme of the wide GCPW-to-small GCPW transition.

TABLE 3.VIII
OPTIMIZED GEOMETRICAL PARAMETERS OF THE WIDE GCPW-TO-SMALL GCPW
TRANSITION.

Symbol	Value	Description
W_{ms}	0.375 mm	Small GCPW width
L_{ms}	0.4 mm	Small GCPW length
$L_{t,50}$	4 mm	Wide GCPW-to-small GCPW transition length

3.4.4 Small GCPW-to-SIW transition

The transition from small GCPW to SIW is shown in Fig. 3.23, reporting the main geometrical parameters. The optimized values are reported in Table 3.IX. The SIW has the same sizes of the feeding SIW of the antenna.

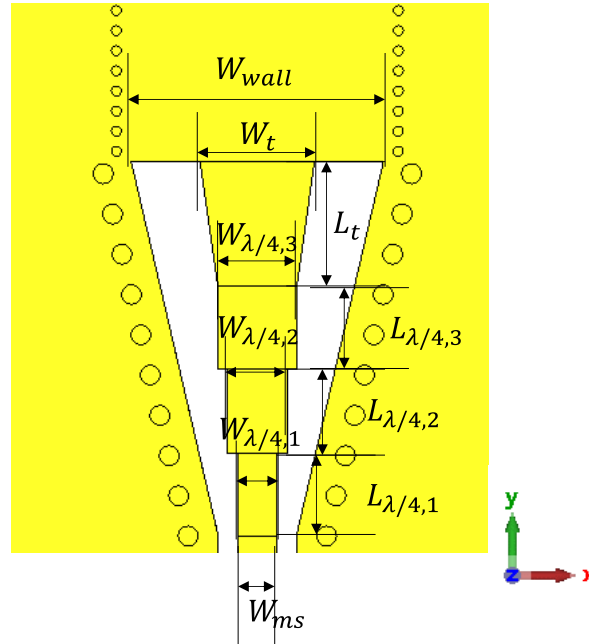


Fig. 3.23. Scheme of the small GCPW-to-SIW transition.

TABLE 3.IX

OPTIMIZED GEOMETRICAL PARAMETERS OF THE SMALL GCPW-TO-SIW TRANSITION.

Symbol	Value	Description
$W_{\lambda/4,1}$	0.39 mm	Width of the first quarter wavelength line
$W_{\lambda/4,2}$	0.6 mm	Width of the second quarter wavelength line
$W_{\lambda/4,3}$	0.783 mm	Width of the third quarter wavelength line
$L_{\lambda/4,1}$	0.83 mm	Length of the first quarter wavelength line
$L_{\lambda/4,2}$	0.83 mm	Length of the second quarter wavelength line
$L_{\lambda/4,3}$	0.83 mm	Length of the third quarter wavelength line
W_t	1.136 mm	Transition width
L_t	1.24 mm	Transition length
W_{wall}	2.5 mm	Wall width

3.4.5 SIW-to-air-filled SIW transition

To assure a good impedance matching, a suitable transition from full substrate SIW to air-filled SIW has been designed, by minimizing the confinement losses. The transition from SIW to air-filled SIW is shown in Fig. 3.24, reporting the main geometrical parameters. The optimized values are reported in Table 3.X. The SIW has the same sizes of the feeding SIW of the antenna.

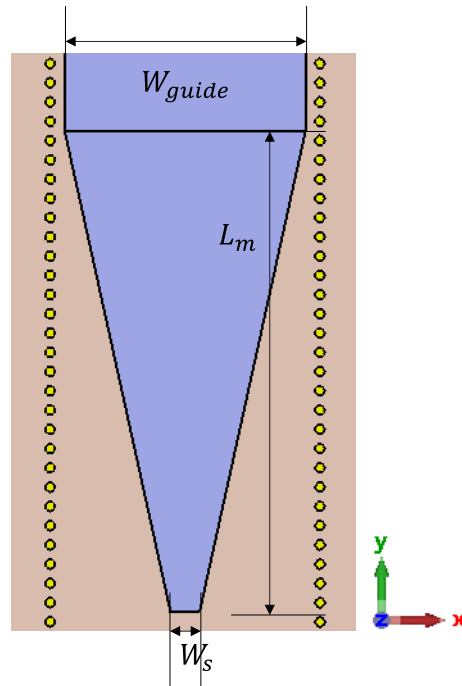


Fig. 3.24. Scheme of the SIW-to-air-filled SIW transition.

TABLE 3.X
OPTIMIZED GEOMETRICAL PARAMETERS OF THE SIW-TO-AIR-FILLED SIW TRANSITION.

Symbol	Value	Description
W_{guide}	2.5 mm	Air guide width
L_m	5 mm	Air transition length
W_s	0.3 mm	Air transition minimum width

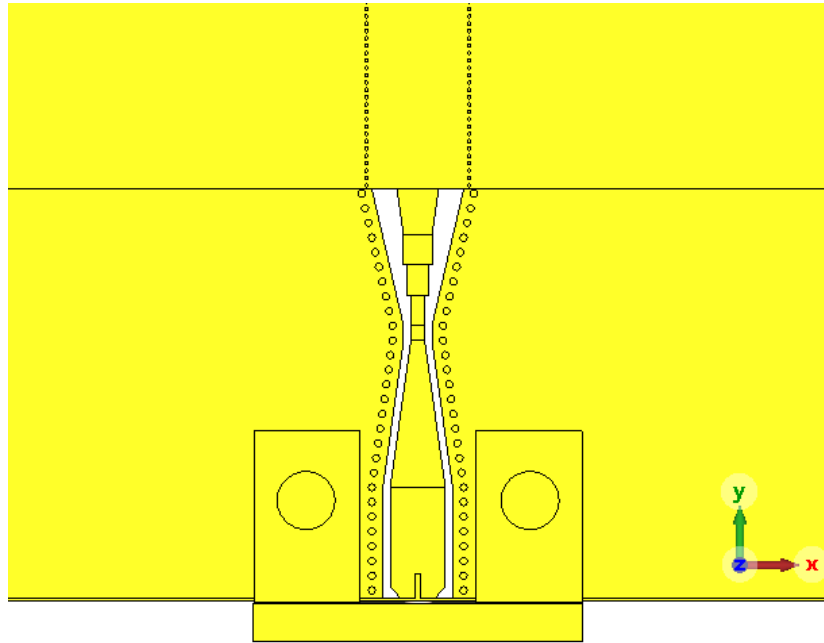
3.4.6 Connector-to-air-filled SIW transition

The complete transition from connector to air-filled SIW, obtained composing the previous segments, is shown in Fig. 3.25. In particular, Fig. 3.25(a) shows the top layer of the transition, whereas Fig. 3.25(b) shows the transition from the full substrate to the air-filled SIW.

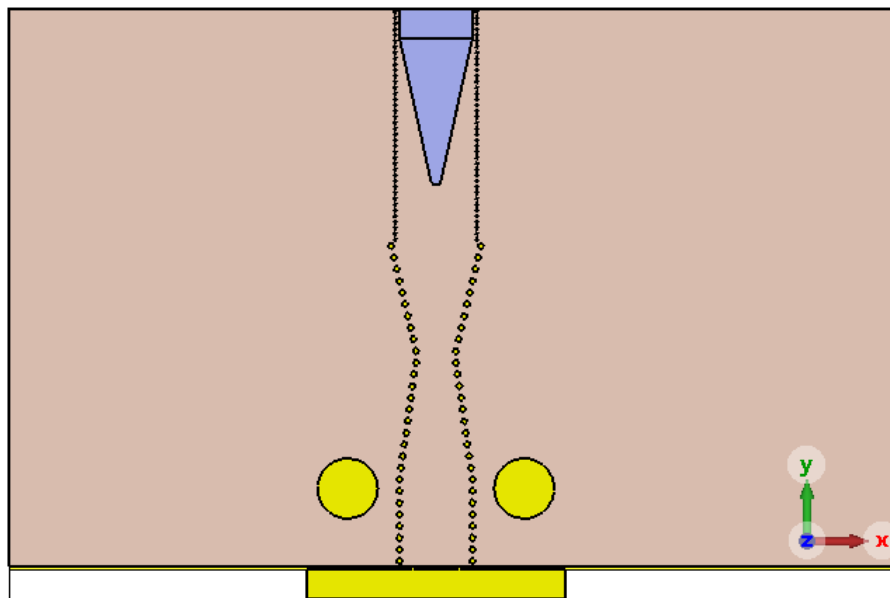
The complete structure has been optimized to obtain the best impedance matching and the best power delivery. Fig. 3.26 shows the modulus of the scattering parameters S_{11} and S_{21} as a function of the frequency in the working bandwidth, confirming the good behavior of the transition.

As a last step, the antenna fed with the connector has been simulated and compared with the same antenna fed by a CST Waveguide Port. Fig. 3.27 reports

the modulus of the scattering parameter S_{11} as a function of frequency f for the two cases. Table 3.XI reports the performances comparison of the 8×8 slot antenna with and without the connector.



(a)



(b)

Fig. 3.25. Connector-to-SIW transition. (a) top layer, (b) full substrate to air-filled SIW.

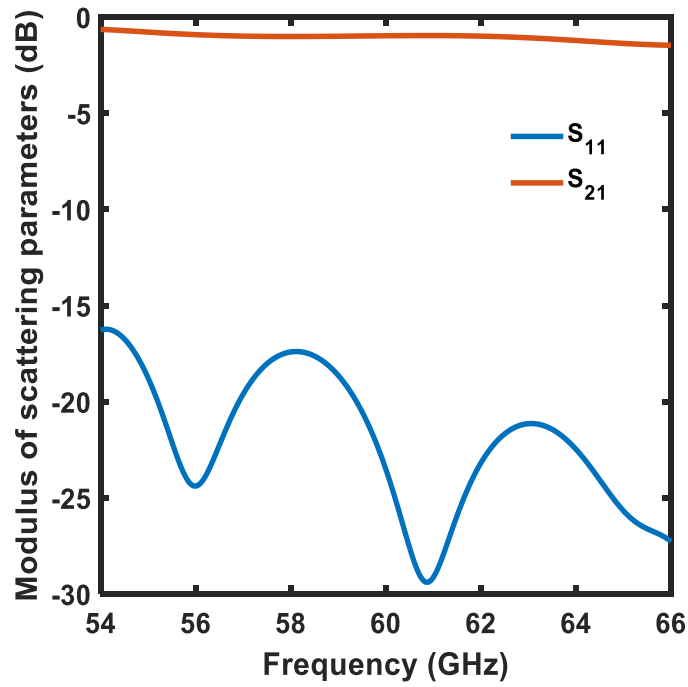


Fig. 3.26. Modulus of the scattering parameters S_{11} (blue curve) and S_{21} (red curve) as a function of the frequency f for the optimized transition.

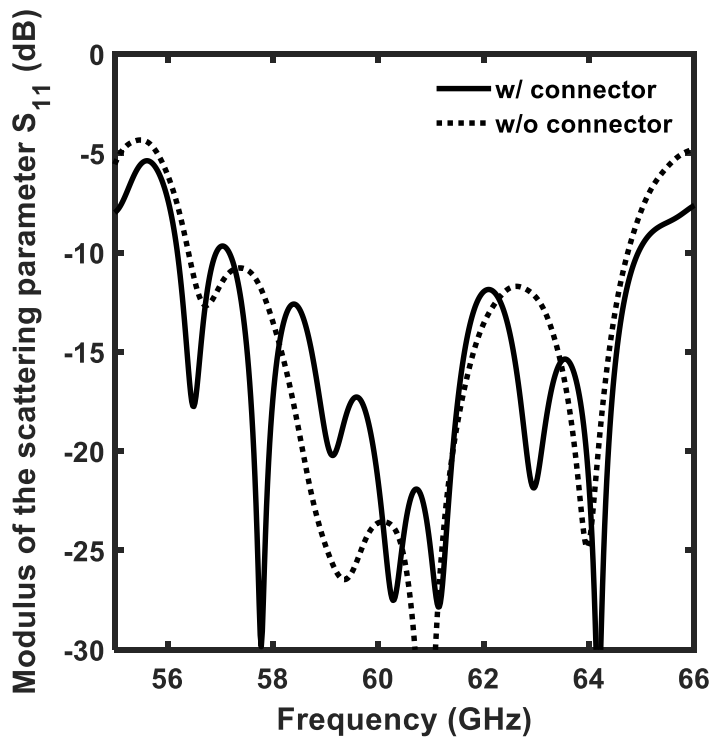


Fig. 3.26. Modulus of the scattering parameters S_{11} as a function of the frequency f , for the 8×8 slot antenna fed with the connector (solid curve) and with a CST Waveguide Port (dotted curve).

TABLE 3.XI
PERFORMANCES COMPARISON OF THE 8×8 SLOT ANTENNA WITH AND WITHOUT
CONNECTOR.

	With connector	Without connector
Gain G	24.3 <i>dB</i>	25.3 <i>dB</i>
Efficiency η	85 %	88 %
Percentage bandwidth $BW_{\%}$	13.3%	13.3 %

3.5 Conclusions

An air-filled SIW array antenna has been designed and optimized to operate at $f = 60$ GHz, employing a multilayer structure. Gain $G = 24.3$ dB, efficiency $\eta = 85\%$, and percentage bandwidth $BW_{\%} = 13.3\%$ have been obtained for the 8×8 slot antenna. The proposed technology can be considered a good alternative to full-metallic antennas or LTCC antennas, thanks to simple construction process, reduced fabrication costs, and good performances. The prototype will be soon fabricated and characterized at the Institut d'Electronique et des Technologies du numéRique (IETR).

4 Design of a Substrate Integrated Waveguide microwave sensor for water-in-fuel applications

4.1 Introduction

In this chapter, a water-in-diesel microwave sensor based on a Substrate Integrated Waveguide (SIW) microwave applicator is designed and characterized in this study. Thanks to SIW technology, the integration with the well-consolidated Printed Circuit Board (PCB) technology allows a feasible and low-cost interconnection with suitable optics and electronics. This opens the way to IoT applications with high compactness and integration.

The monitoring of hydrocarbon quality is an important goal, not only for modern automotive, industrial, and aerospace applications, but also in view of the next uses of biodiesel fuel generation [86-87]. There are many different contaminants that can compromise hydrocarbon quality, such as alcohol, water, ethanol, and oils [86-88]. Monitoring should be fast, accurate and real time, because these contaminants could alter the lubrication properties of fuel and reduce motor performance. In particular, they could alter the viscosity, density, and boiling point of the hydrocarbons. In general, traditional laboratory techniques, such as an evaporation test, distillation, gas chromatography, useful to identify the quality of petroleum liquid and its derivative products, are more expensive and introduce a delay time for analysis. Microwave sensor techniques provide an interesting alternative approach [89-91].

The interaction between the microwave electromagnetic field and the diesel fuel contaminated with small concentrations of water is obtained via suitable radiating slots placed on the top of an SIW waveguiding structure. The SIW applicator working frequency is chosen by observing the behavior of the complex dielectric permittivity of the fuel–water blend based on a preliminary wide band investigation. The performances of the SIW microwave sensor are evaluated in terms of scattering parameter modulus $|S_{21}|$ as a function of the water

concentration in ppm. The best sensitivity $\frac{\Delta|S_{21}|}{\Delta\rho} = 1.42 \text{ mdB/ppm}$ is obtained at a frequency $f = 9.76 \text{ GHz}$, with a coefficient of determination $R^2 = 0.94$. The sensor is low-cost, low profile and ensures a good sensitivity for constant and real-time monitoring.

4.2 Water-fuel blend characterization

The SIW microwave applicator is designed to work in the frequency range $f = 9 - 11 \text{ GHz}$ with CST Studio Suite[®] software. This frequency range was chosen by observing the behavior of the complex dielectric permittivity of the fuel–water blend, on the basis of a wide-band investigation performed with a SPEAG DAK 3.5 probe [92] and a N9927A FieldFox Handheld Microwave Vector Analyzer by Keysight [93]. This preliminary investigation has highlighted changes in complex dielectric permittivity at the aforementioned frequencies, thus promising potential applications for sensing.

Five fuel samples were prepared containing different concentrations of contaminant water. In particular, $\rho = 0 \text{ ppm}$ (pure diesel), $\rho = 50 \text{ ppm}$, $\rho = 200 \text{ ppm}$, $\rho = 500 \text{ ppm}$, and $\rho = 1000 \text{ ppm}$ of water were prepared. Water concentrations higher than $\rho = 500 \text{ ppm}$ were not investigated because they are not interesting for practical applications, as they are over the acceptable limits regarding water contamination. The concentration $\rho = 1000 \text{ ppm}$ has been taken into account to verify the characteristics slope for extreme contaminations. Fig. 4.1 shows the SPEAG DAK 3.5 probe-N9927A VNA characterization set-up. For each sample, the dielectric constant measurement was repeated seven times. These measurement results have been averaged to reduce measurement noise and fitted with a polynomial. Table 4.I reports the order and the coefficient of determination R^2 of the polynomial fitting the five measured dielectric constant curves. The fitting order has been chosen to maximize R^2 .

TABLE 4.I
ORDER AND COEFFICIENT OF DETERMINATION R^2 OF THE POLYNOMIAL FITTING THE MEASURED DIELECTRIC CONSTANT CURVES

Sample	Fitting Order	R^2 of the Polynomial Fitting
$\rho = 0 \text{ ppm}$	8	0.95
$\rho = 50 \text{ ppm}$	3	0.93
$\rho = 200 \text{ ppm}$	3	0.97
$\rho = 500 \text{ ppm}$	9	0.91
$\rho = 1000 \text{ ppm}$	8	0.90

The measured complex dielectric constants for the five samples as functions of the frequency are reported in Fig. 4.2 (real part ϵ') and Fig. 4.3 (imaginary part ϵ'').

It is worth observing that the real part ϵ' increases as the water concentration increases in a wide frequency range, $f = 8 - 13 \text{ GHz}$. To obtain reference values for the ad hoc-designed water–diesel fuel blend SIW applicator, we directly considered the SPEAG DAK 3.5 probe-N9927A VNA-measured characteristics. In particular, by choosing different frequencies, e.g., $f = 9, 10, 11, 12, 13 \text{ GHz}$, different sensing characteristics, i.e., regression curves, can be drawn, as reported in Fig. 4.4. At these frequencies, a direct proportionality between the water concentration ρ and the real part ϵ' occurs. Therefore, they are of interest for sensing applications. On the contrary, the frequencies $f < 7 \text{ GHz}$ or $f > 14 \text{ GHz}$ are not considered. The characteristics are quite similar, even if with a different coefficient of determination R^2 , indicating the proportionate amount of variation in the response variable explained by the independent variable in the linear regression model. We underline that this preliminary investigation has been performed to roughly identify a frequency range where the variation in the complex dielectric constant with water concentration promises potential applications to be investigated.

Table 4.II reports the measured sensitivities for the five curves of Fig. 4.4, confirming this observation. The direct proportionality between the real part ϵ' and the water concentration ρ pave the way to design an ad hoc water in diesel microwave sensor.



Fig. 4.1. Characterization set-up with VNA Keysight N9927A FieldFox and DAK 3.5 probe.

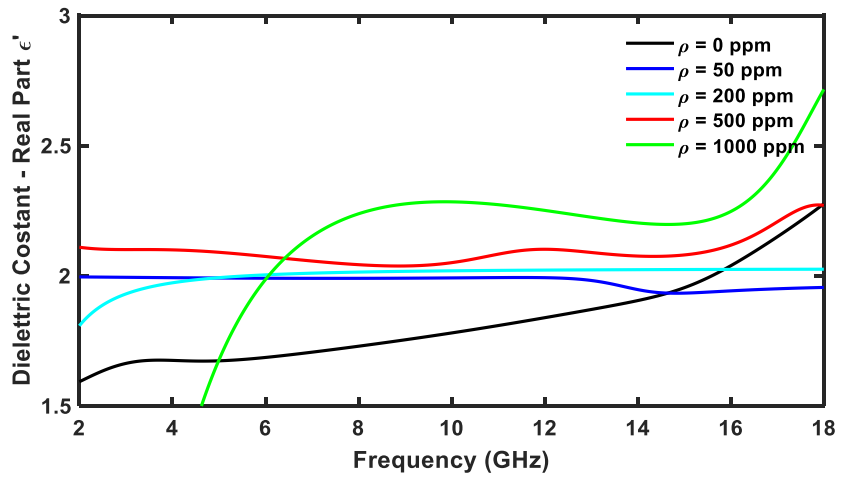


Fig. 4.2. Measured real part ϵ' of the dielectric constant as a function of the frequency f for different water concentrations ρ in diesel.

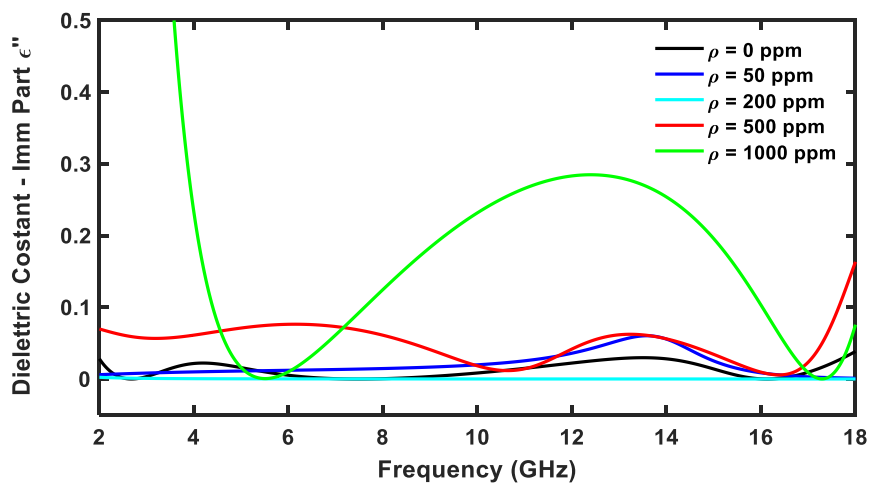


Fig. 4.3. Measured imaginary part ϵ'' of the dielectric constant as a function of the frequency f for different water concentrations ρ in diesel.

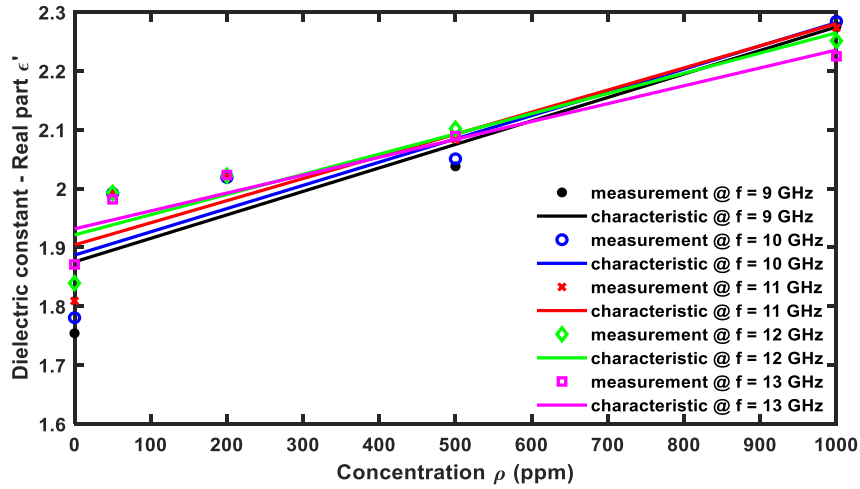


Fig. 4.4. Real part ϵ' of the dielectric constant, measured with SPEAG DAK 3.5 probe-N9927A VNA, as a function of the water concentration ρ in diesel, for different frequencies.

TABLE 4.II
SENSITIVITIES OF THE SPEAG DAK 3.5 PROBE-N9927A VNA AS A WATER-IN-FUEL SENSOR FOR DIFFERENT FREQUENCIES

Frequency (GHz)	Sensitivity $\frac{\Delta\epsilon_r}{\Delta\rho} (\times 10^{-3}/ppm)$	R^2
9	0.399	0.79
10	0.395	0.82
11	0.376	0.86
12	0.344	0.88
13	0.304	0.91

4.3 Applicator design

The aim of the design is to obtain a low cost, planar/low-profile and compact (of few square centimeters) microwave applicator, providing good performance in terms of sensitivity and resolution, even if operating at a single frequency, to be employed in a simple online set-up, for example including a microwave source and a microwave power meter.

The employed dielectric substrate is Rogers RT/duroid 5880 ($\epsilon_r = 2.2$, $\tan\delta = 0.0009$) of commercial thickness $h_{sub} = 1.575 \text{ mm}$, whereas metallic parts are made of copper ($\sigma = 5.8 \times 10^7 \text{ S/m}$) with thickness $h = 0.035 \text{ mm}$.

The design and characterization of the SIW applicator is performed with reference to both the air and water-in-diesel surrounding medium (background). In the case of the water-in-diesel background, the measured complex dielectric constant of Fig. 4.2 and 4.3 have been considered.

4.3.1 Single slot SIW applicator in air

The first geometry, reporting the main parameters, is shown in Fig. 4.5. The preliminary values of the geometric parameters are reported in Table 4.III. The geometry depicted in Fig. 4.5 is obtained considering an SIW guide fed by a microstrip line. The strip line sizes W_{feed} and L_{feed} are designed to ensure a characteristic impedance $Z_0 = 50 \Omega$ [94]. The vias diameter d , the center-center distance s , and the other preliminary geometrical values are chosen following formulas of paragraph 2.1. The slot ensures the radiation of the EM field and its interaction with the fuel samples.

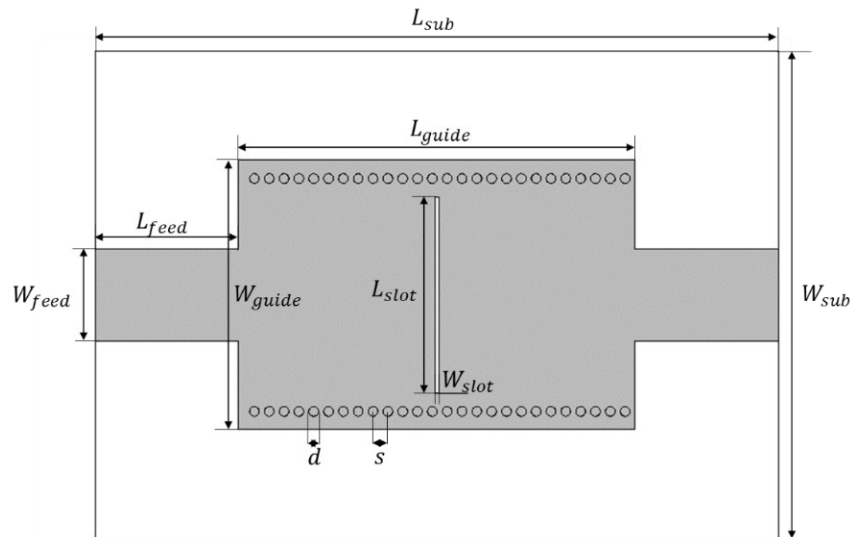


Fig. 4.5. Scheme of the designed single-slot SIW applicator in air.

Fig. 4.6 shows the equivalent circuit of the single-slot SIW applicator [43–45]. The distributed-constants network, modelling the input and output microstrip transmission lines, includes the series impedance $Z = R + j\omega L$ per unit length and the shunt admittance $Y = G + j\omega C$ per unit length. The inductance L_s and the capacity C_s model the transverse slot [95].

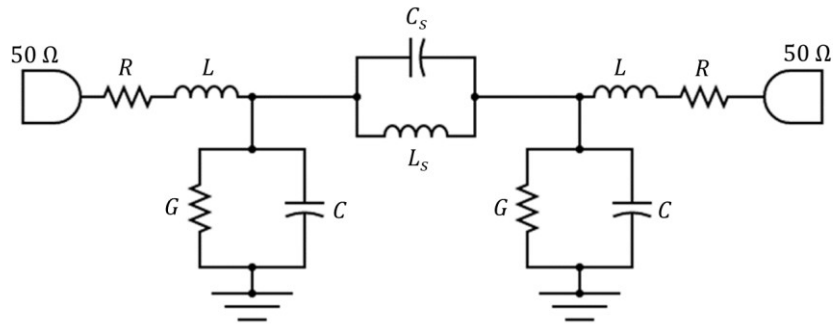


Fig. 4.6. Equivalent circuit of the single-slot SIW applicator.

Fig. 4.7 shows the distribution of the modulus of the electric field irradiated by the slot in the xy plane, i.e., at the upper metal layer. The discontinuity between the feeding microstrip line and the SIW tends to confine the electric field near to the slot, as in a slotted resonant-like structure, improving the interaction with the fuel samples.

TABLE 4.III

MAIN GEOMETRIC PARAMETERS OF THE DESIGNED SINGLE-SLOT SIW APPLICATOR IN AIR

Parameter	Value	Description
L_{sub}	35 mm	Substrate length
W_{sub}	25 mm	Substrate width
L_{guide}	14.3 mm	SIW length
W_{guide}	13.8 mm	SIW width
W_{feed}	4.7 mm	Microstrip line width
L_{feed}	10.35 mm	Microstrip line length
W_{slot}	0.3 mm	Slot width
L_{slot}	10.05 mm	Slot length
s	0.75 mm	Center-center distance of vias
d	0.5 mm	Vias diameter

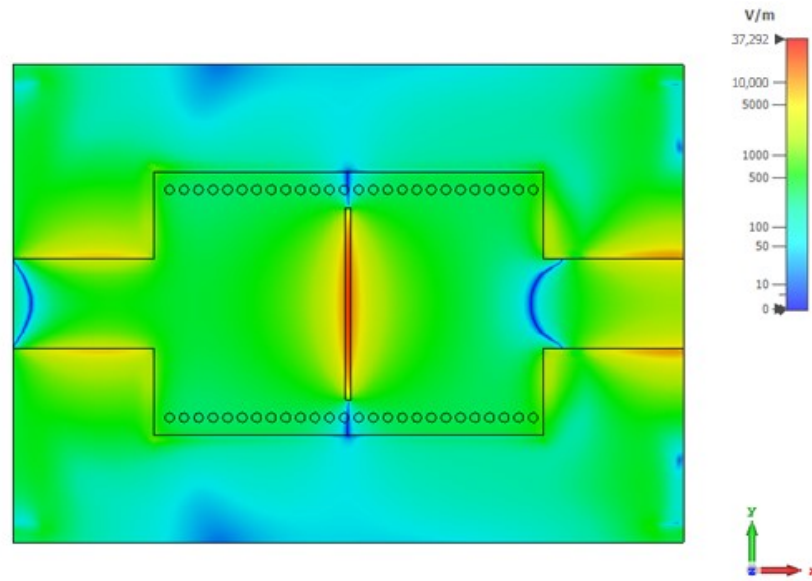


Fig. 4.7. Modulus of the electric field irradiated by the slot in the xy plane, single-slot SIW applicator in air.

The first optimization regards the SIW length L_{guide} . Starting from the preliminary value reported in Table 4.III, $L_{guide} = 14 \text{ mm}$, larger values have been simulated until $L_{guide} = 20 \text{ mm}$, by considering a change step $\Delta L_{guide} = 2 \text{ mm}$. The extreme of the range $L_{guide} = 20 \text{ mm}$ is arbitrarily fixed to guarantee a high compactness degree.

The modulus of the scattering parameters S_{11} and S_{21} as a function of frequency f for different values of the SIW length L_{guide} has exhibited a bandwidth increase and an increased impedance matching at the fixed extreme value $L_{guide} = 20 \text{ mm}$. The optimization of the radiating slot is performed with the aim of further improving the device operation. Fig. 4.8 shows the modulus of the scattering parameters S_{11} (solid curves) and S_{21} (dotted curves) as a function of frequency f for different values of the slot width W_{slot} . As the slot width becomes smaller, a better impedance matching can be observed. However, the extreme $W_{slot} = 0.2 \text{ mm}$ was arbitrarily fixed to allow a sufficient interaction between measurand background and EM field. Many other optimizations were performed by varying slot length L_{slot} , center-center vias distance s , and vias diameter d , but the performances were worse.

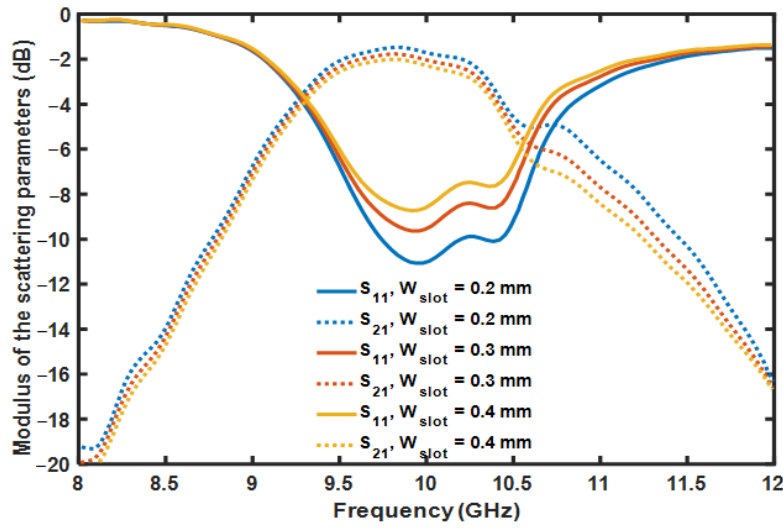


Fig. 4.8. Modulus of the scattering parameters S_{11} (solid curves) and S_{21} (dotted curves) as a function of frequency f for different values of the slot width W_{slot} .

4.3.2 Cross slot SIW applicator in air

The SIW applicator geometry is modified with the aim to improve the sensing performances. Two half geometries, allowing half mode behavior, of the previous applicator are placed in close position and coupled via a gap, named the horizontal slot. The further, horizontal, slot is designed to enhance the interaction between the EM field and the fuel samples. The new geometry, reporting the main parameters, is shown in Fig. 4.9. The preliminary values of the geometric parameters are reported in Table 4.IV. For this SIW applicator, asymmetric input and output microstrip lines are designed. This is justified by considering that it is similar to the composition of two half-mode structures.

Fig. 4.10 shows the equivalent circuit of the cross-slot SIW applicator. The equivalent circuit is composed by two circuits similar to the previous one. Each of them refers to one of the two half-mode structures. The proximity coupling is modelled via the mutual inductance of M_{12} , the effect of the cut on the half-mode structure is modeled by a properly high value load impedance Z_L .

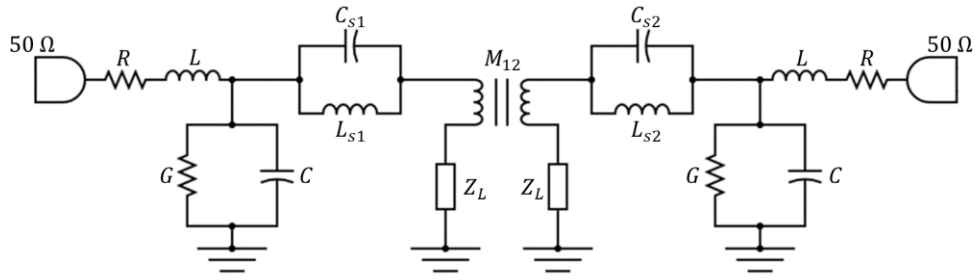


Fig. 4.10. Equivalent circuit of the cross slot SIW applicator.

The SIW length is again set at $L_{guide} = 20 \text{ mm}$. The optimization has regarded the parameters of slot width W_{slot} , slot length L_{slot} , and gap width W_{gap} .

For the slot width W_{slot} , the parametric investigation is performed in the range $W_{slot} = 0.2 - 0.4 \text{ mm}$. The modulus of the scattering parameters S_{11} and S_{21} as a function of the frequency f for different values of slot width W_{slot} is simulated. As the slot width W_{slot} decreases, the impedance matching increases. The best value is $W_{slot} = 0.2 \text{ mm}$. This value is a trade-off. A narrower slot is not investigated, as previously discussed in Section 4.1. Moreover, good impedance matching with $|S_{11}| = -22 \text{ dB}$ at the frequency of $f = 9.6 \text{ GHz}$ is reached. A further decrease in the length of W_{slot} is not interesting and could cause an interaction reduction with the background.

The gap width W_{gap} is varied in the range of $W_{gap} = 0.2 - 0.4 \text{ mm}$. Fig. 4.11 shows the modulus of the simulated scattering parameters S_{11} (solid curves) and S_{21} (dotted curves) as a function of the frequency f for different values of gap width W_{gap} . Additionally, the gap width modifies the applicator impedance matching. The best value is $W_{gap} = 0.2 \text{ mm}$, ensuring the maximum transmission bandwidth and the minimum scattering parameter modulus $|S_{11}|$. The impedance matching with $|S_{11}| = -23 \text{ dB}$ at the frequency $f = 9.6 \text{ GHz}$ is obtained.

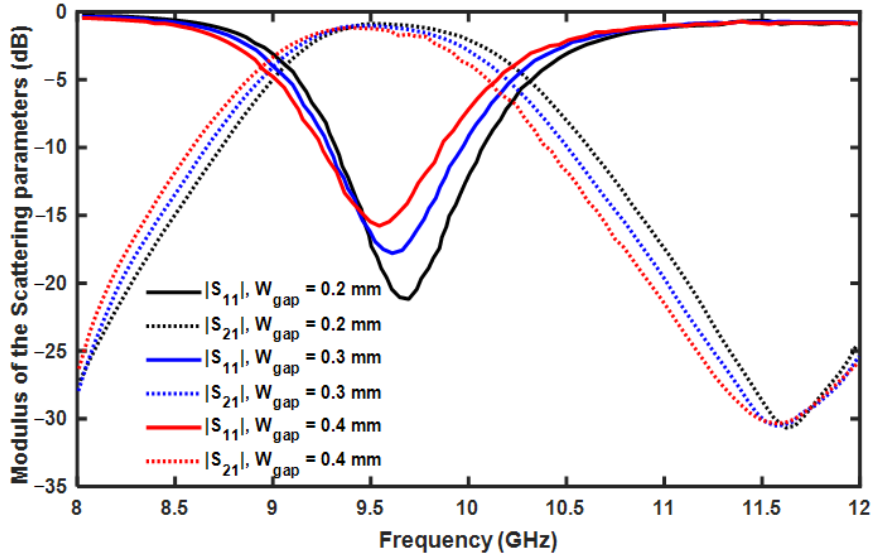


Fig. 4.11. Modulus of the simulated scattering parameters S_{11} (solid curves) and S_{21} (dotted curves) as a function of the frequency f for different values of W_{gap} .

The slot length L_{slot} is varied in the range of $L_{slot} = 4.9 - 5.3 \text{ mm}$ in order to ensure the maximum interaction between the fuel sample and the sensor. The modulus of the scattering parameters S_{11} and S_{21} as a function of the frequency f has been simulated for different values of L_{slot} . As the slot length L_{slot} decreases, the impedance matching increases, and the bandwidth becomes larger. The impedance matching with $|S_{11}| = -19 \text{ dB}$ at the frequency of $f = 9.6 \text{ GHz}$ is simulated for $L_{slot} = 4.9 \text{ mm}$.

After all the optimizations, the optimal geometrical dimensions for the cross-slot SIW device are reported in Table 4.V. These values ensure a good impedance matching and the wide bandwidth in the 9–10 GHz range. The device is also compact and low-profile.

TABLE 4.V
OPTIMIZED GEOMETRIC PARAMETERS OF THE DESIGNED CROSS-SLOT SIW APPLICATOR

Parameter	Value	Description
L_{sub}	35 mm	Substrate length
W_{sub}	25 mm	Substrate width
L_{guide}	20 mm	SIW length
$W_{guide/2}$	6.9 mm	Half SIW width
W_{feed}	4.7 mm	Microstrip line width
L_{feed}	7.5 mm	Microstrip line length
W_{slot}	0.2 mm	Slot width
L_{slot}	4.9 mm	Slot length
gap	0.2 mm	Gap distance
s	0.75 mm	Center-center distance of vias
d	0.5 mm	Vias diameter

4.4 Simulation of cross-slot SIW applicator as sensor, water-in-diesel background

To evaluate the cross-slot SIW applicator performances as a water-in-fuel sensor, the measured dielectric constants of the five samples were imported into the simulation CST Studio Suite[®] software. A similar investigation to that reported in Section 4.3 was performed, showing that the same SIW structure could be employed with a water-in-diesel background, allowing a promising performance without further refinement. In other words, the dielectric constant of air and the real part ϵ' of the diesel dielectric constant at the considered frequencies f are sufficiently close.

In fact, Fig. 4.12 illustrates the modulus of the scattering parameters S_{11} (solid curves) and S_{21} (dotted curves) as a function of the frequency f for air (black curve) and pure diesel (blue curve) backgrounds. The impedance matching with $|S_{11}| = -18 \text{ dB}$ at the frequency $f = 9.5 \text{ GHz}$ for the diesel background is good enough.

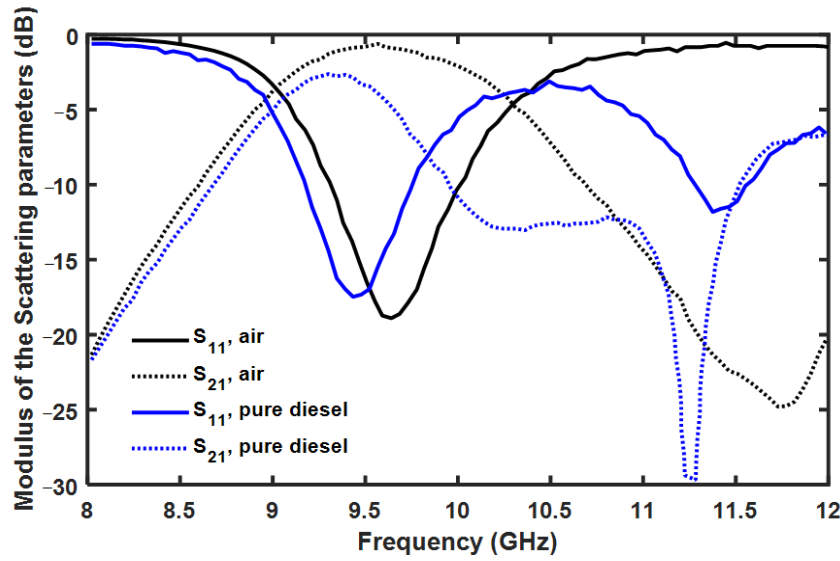


Fig. 4.12. Cross-slot SIW applicator. Modulus of the simulated scattering parameters S_{11} (solid curves) and S_{21} (dotted curves) as a function of the frequency f for air (black curves) and pure diesel (blue curves) backgrounds.

The percentage change on the modulus of the scattering parameter S_{21} , obtained by simulating the diesel sample (i) in contact and (ii) placed at the distance $d_{air} = 0.1 \text{ mm}$ from the top metallic layer, is below $\Delta S_{21} = 9\%$. However, the distance d_{air} can be eliminated in practical application after an easy mechanical optimization.

The percentage change in the modulus of the scattering parameter S_{21} obtained by simulating the diesel sample in contact with the top metallic layer and the radiating slots (iii) filled with diesel and (iv) filled with air is of the order of $\Delta S_{21} = 1.3\%$. Additionally, this error can be eliminated by a direct contact of the applicator with diesel flux.

Fig. 4.13(a) shows the modulus of the simulated scattering parameter S_{21} as a function of the frequency f for the five different water concentrations. Fig. 4.13(b) is a magnified view of the matching frequency $f = 9.5 \text{ GHz}$. It shows that, as the water concentration increases, the modulus of the scattering parameter S_{21} decreases. The variation is quite linear. The values of the modulus of the scattering parameter S_{21} for the five water concentrations at frequency $f = 9.2 \text{ GHz}$ are listed in Table 4.VI.

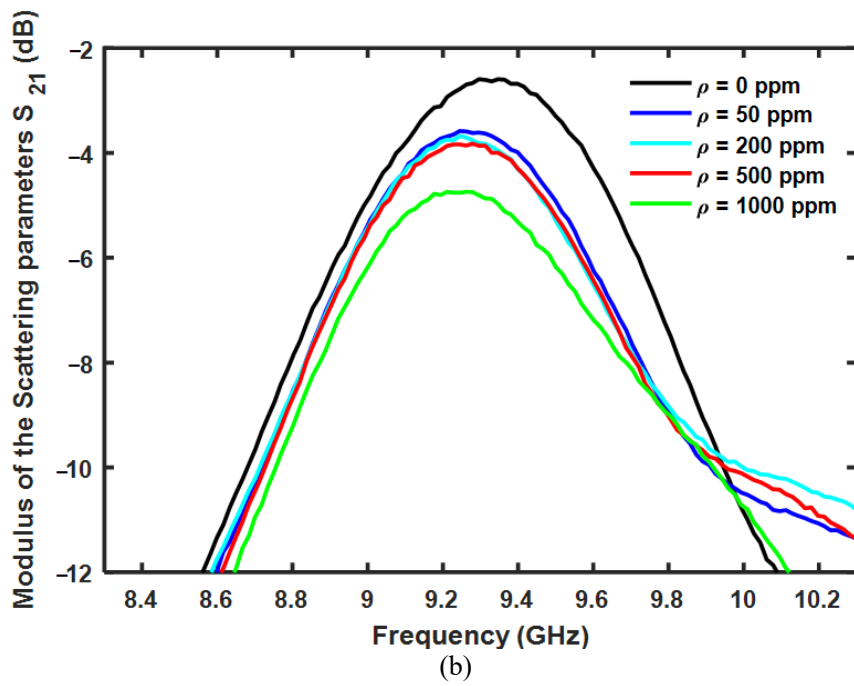
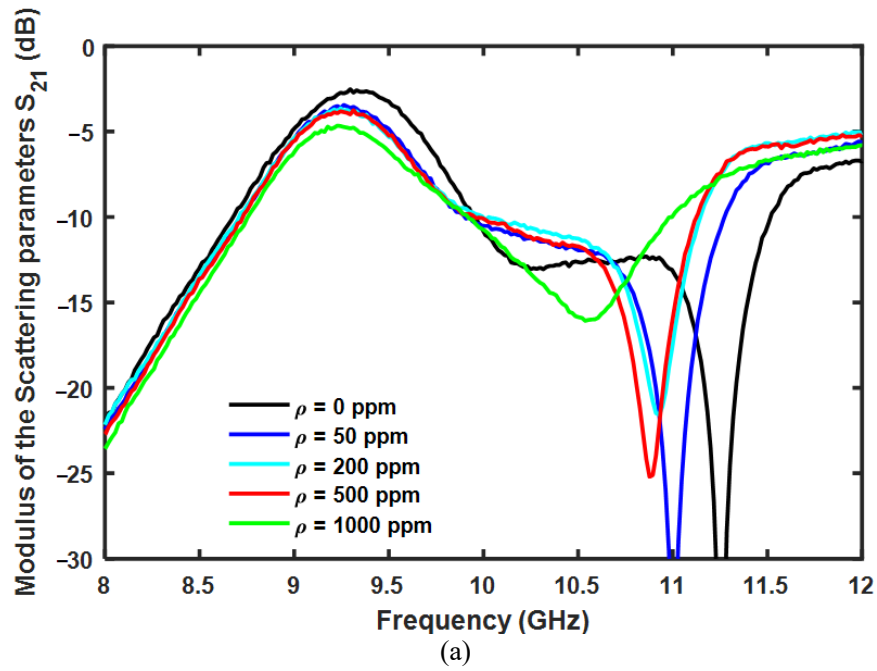


Fig. 4.13. Cross-slot SIW applicator. (a) Modulus of the simulated scattering parameters S_{21} as a function of the frequency f for different water concentrations. (b) Zoom around $f = 8.3 - 10.3$ GHz.

TABLE 4.VI
OPTIMIZED GEOMETRIC PARAMETERS OF THE DESIGNED CROSS-SLOT SIW APPLICATOR

Water Concentration ρ (ppm)	$ S_{21} @9.2 \text{ GHz}$ (dB)
0	-3.033
50	-3.718
200	-3.827
500	-3.930
1000	-4.778

The simulated sensor sensitivity can be calculated as

$$\frac{\Delta|S_{21}|}{\Delta\rho} = 1.39 \text{ mdB/ppm @ } 9.2 \text{ GHz} \quad (4.1)$$

The coefficient of determination is $R^2 = 0.85$, which is quite good.

4.5 Cross-slot SIW applicator characterization, air background

The cross-slot SIW applicator was constructed and characterized. Fig. 4.14 shows the fabricated device.

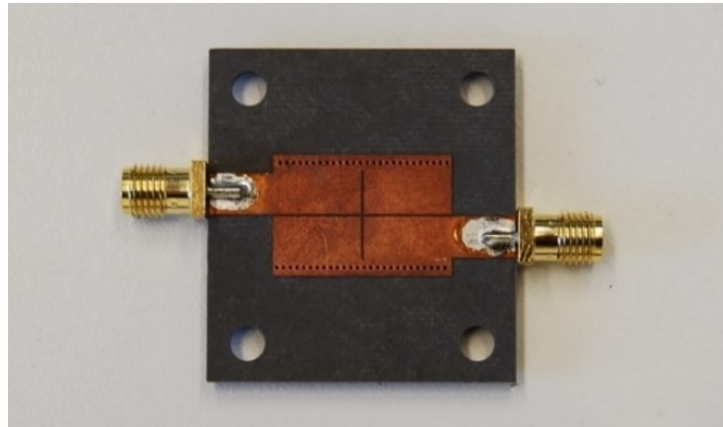


Fig. 4.14. Constructed cross-slot SIW applicator.

The cross-slot SIW applicator was characterized with air as the background, i.e., without considering the fuel sample to be detected, with the VNA Keysight FieldFox. The measured modulus of the scattering parameters S_{11} and S_{21} as a

function of the frequency f is shown in Fig. 4.15 (solid curves) and compared with the simulated parameters (dotted curves). The results are in agreement with the simulations. A right shift of about $\Delta f = 0.5 \text{ GHz}$ can be seen for both S_{11} and S_{21} curves. This behavior can be caused by the fabrication tolerance leading to a little mismatch between the geometric dimensions of the fabricated device and the nominal/optimized ones reported in Table 4.V.

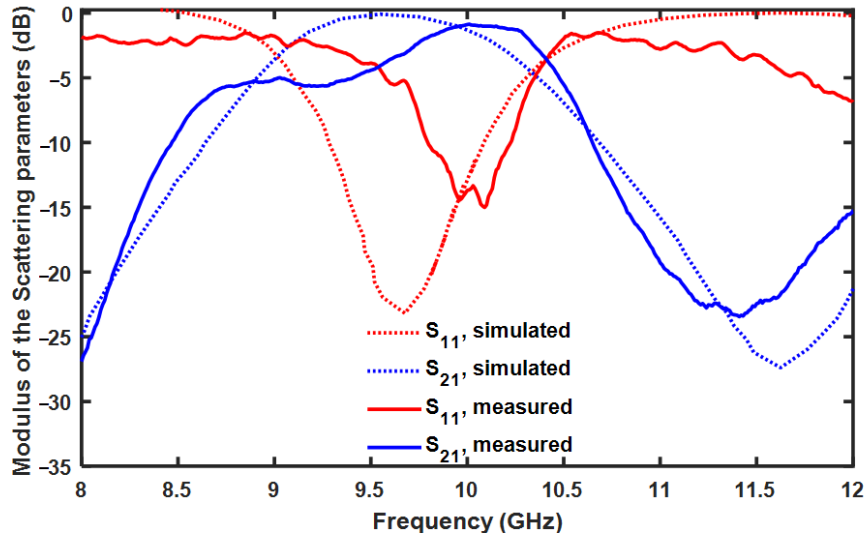


Fig. 4.15. Cross-slot SIW. Modulus of the scattering parameters S_{11} and S_{21} as a function of the frequency f for measured (solid curves) and simulated (dotted curves).

4.6 Cross-slot SIW applicator characterization, water-in-diesel background

The same fuel samples, characterized in paragraph 4.2 and simulated in paragraph 4.4, were used for testing the cross-slot SIW applicator as a water-in-fuel sensor. The bag containing the fuel samples is constituted by polyethylene. Fig. 4.16 shows measurements proving that it can be considered transparent, allowing complete radiating field transmission, and does not affect the water-in-diesel characterization.

The complete measurement set-up is shown in Fig. 4.17(a). It is composed by the VNA Keysight FieldFox, connected to the constructed cross-slot SIW applicator. Fig. 4.17(b) shows the plastic bag as transparent at microwave frequencies and placed on the applicator. Its stability is ensured by an appropriate support.

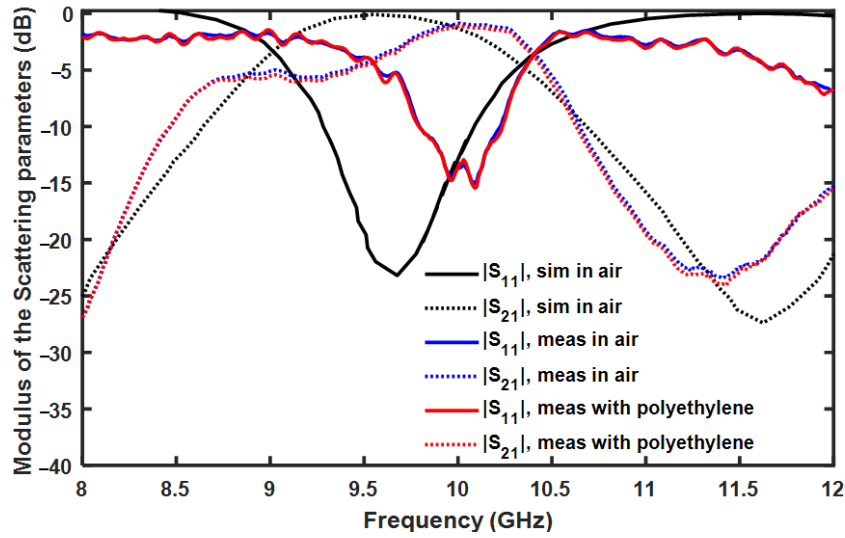


Fig. 4.16. Cross-slot SIW. Modulus of the scattering parameters S_{11} (solid curves) and S_{21} (dotted curves) as a function of the frequency f measured in air (blue curves), measured with polyethylene (red curve), and simulated (black curves).

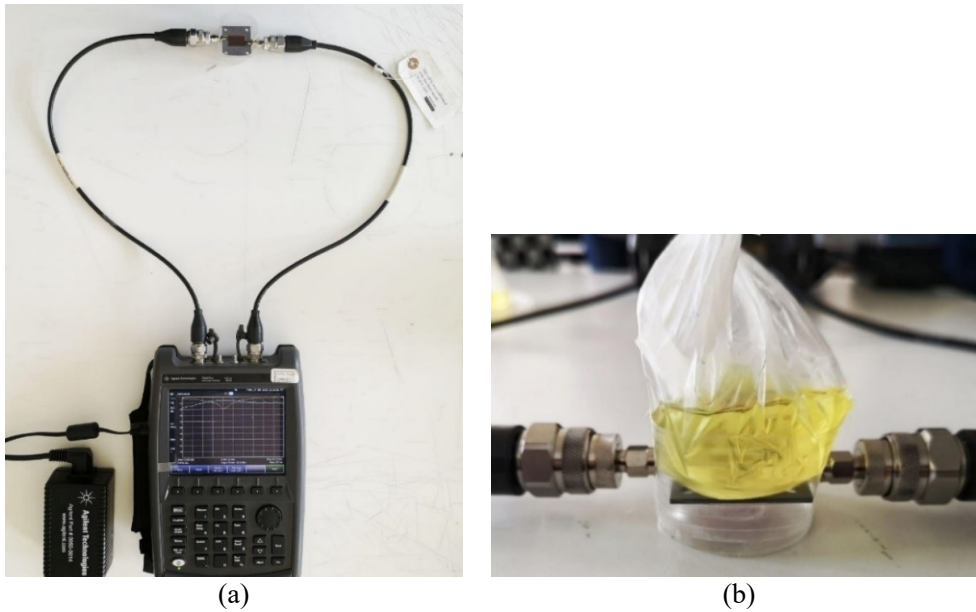
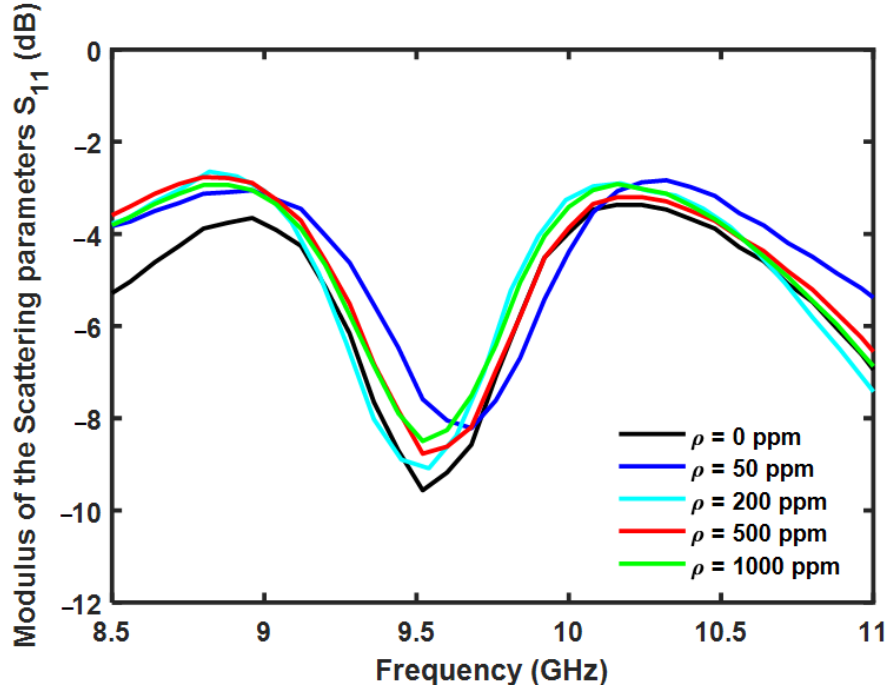


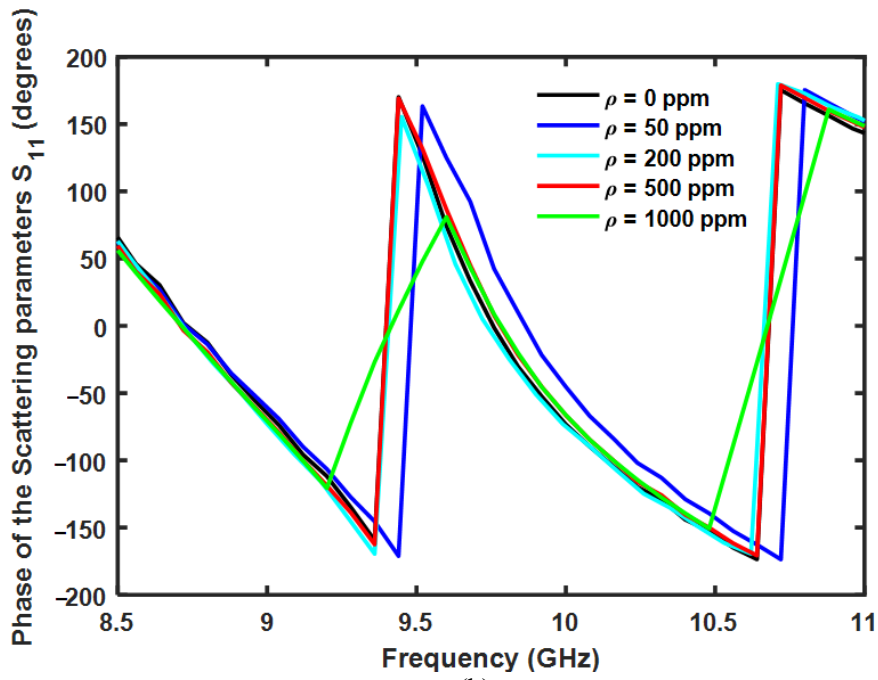
Fig. 4.17. (a) Measurement set-up using the Keysight VNA N9927A FieldFox and the constructed cross-slot SIW applicator as a water-in-fuel sensor; (b) magnified view of one of the measured fuel samples.

Fig. 4.18(a) shows the measured modulus and Fig. 4.18(b) the measured phase of the scattering parameter S_{11} as a function of the frequency, for the five different water concentrations ρ . These curves do not allow us to easily obtain a

sensing characteristic since no change proportional with the water concentration is observed.



(a)



(b)

Fig. 4.18. (a) Measured modulus of the scattering parameter S_{11} as a function of the frequency and (b) measured phase of the scattering parameter S_{11} as a function of the frequency for the five different water concentrations ρ .

Fig. 4.19(a) shows the measured modulus and Fig. 4.19(b) the measured phase of the scattering parameter S_{21} as a function of the frequency f for the five different water concentrations ρ .

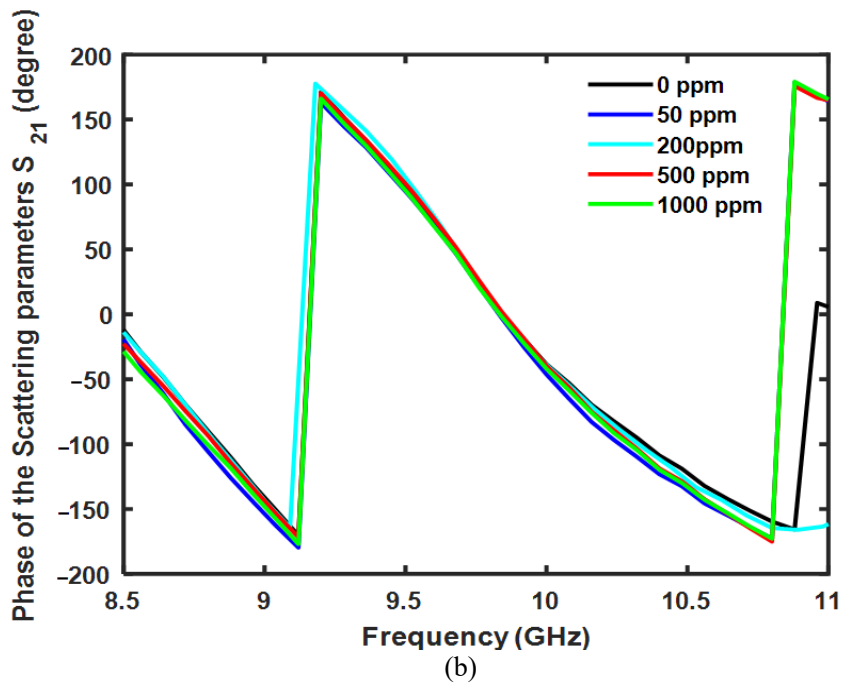
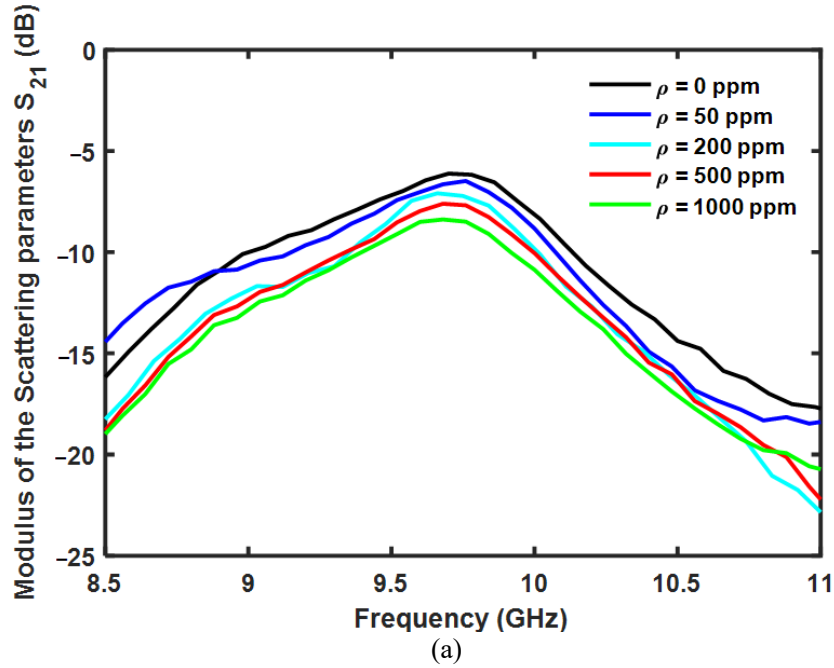


Fig. 4.19. (a) Measured modulus of the scattering parameter S_{21} as a function of the frequency and (b) measured phase of the scattering parameter S_{21} as a function of the frequency for the five different water concentrations ρ .

As expected, no S_{21} phase shift can be observed with variations in water concentration. On the contrary, the measured modulus varies quite linearly, as predicted by simulations. It is affected by the radiated power interacting with the sample, which allows the sensor operation. As for the simulated parameters of Fig. 4.15, the modulus of the scattering parameter S_{21} decreases as the water concentration increases, showing an inverse proportionality.

Table 4.VII reports the values of the measured modulus of the scattering parameter S_{21} for the different concentrations at a frequency of $f = 9.76 \text{ GHz}$, where the $|S_{21}|$ is maximized for all the five curves.

TABLE 4.VII
MEASURED MODULUS OF THE SCATTERING PARAMETER S_{21} FOR THE FIVE WATER CONCENTRATIONS AT A FREQUENCY OF $f = 9.76 \text{ GHz}$.

Water Concentration ρ (ppm)	$ S_{21} @9.2 \text{ GHz}$ (dB)
0	-6.17
50	-6.48
200	-7.21
500	-7.68
1000	-8.49

Fig. 4.20 shows the measured modulus of the scattering parameter S_{21} as a function of the water concentration. The proportionality is quite linear, so it is possible to calculate the sensitivity as

$$\frac{\Delta|S_{21}|}{\Delta\rho} = 1.42 \text{ mdB/ppm @ } 9.76 \text{ GHz} \quad (4.2)$$

The coefficient of determination is $R^2 = 0.94$, which is in excellent agreement with the simulation illustrated in Section 4.4. Considering the VNA N9927A resolution $\Delta S_{21} = 0.01 \text{ dB}$, the proposed set-up is able to measure a minimum variation in water concentration of $\Delta\rho \approx 7 \text{ ppm}$ [93]. The SIW applicator is intriguing for its compactness and performances even when compared with the literature [96-97]. It could be employed with a single frequency source and an MW power meter in order to obtain an online and low-cost system for diesel quality detection.

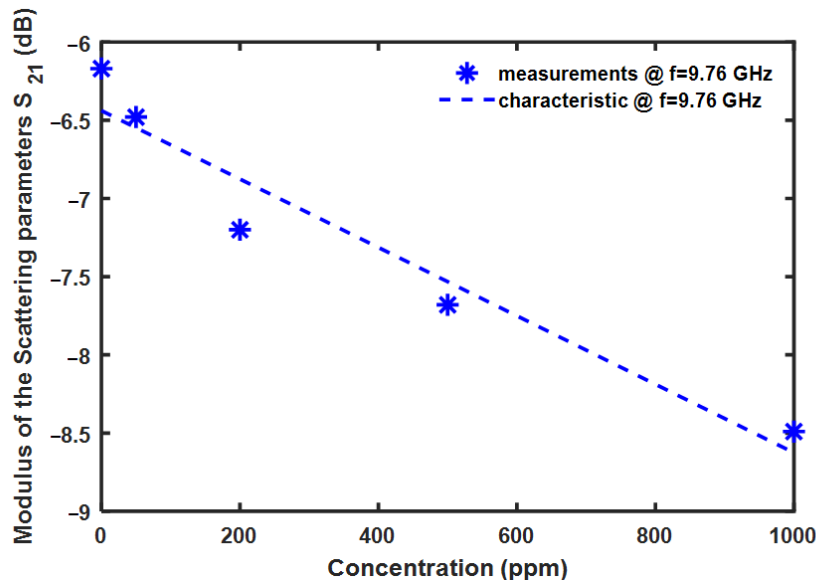


Fig. 4.20. Measured modulus of the scattering parameters S_{21} as a function of water concentration ρ at frequency $f = 9.76 \text{ GHz}$.

The response of the microwave sensor is practically immediate due to the instantaneous interaction of the microwave with the sample. It is worth noting that a potential industrial application for on-time/online measurement could be feasible if the water-in-diesel solution flowed in a microwave-transparent tube, in contact with the sensor like the bag used in this paper. In this case, the tube walls should be continuously washed and in contact with the flow to be monitored, thus allowing an instantaneous sensor response.

The influence of temperature on the applicator response is not significant for relatively large changes. In fact, the thermal expansion causes a negligible variation in the sensor size and, as a consequence, a negligible variation in the chosen resonant frequency. This slight variation does not affect the applicator performance since it can operate over the wide frequency range of $f = 9 - 11 \text{ GHz}$. Due to the temperature dispersion of the complex dielectric constant of the samples, a calibration could be required for large temperature changes.

The main limitation of the proposed applicator is the low selectivity. Generally, microwave sensors are characterized by a low selectivity, since they are based on the dielectric constant variation of the measured sample. Dielectric constant variation can depend on a number of potential contaminants/concentrations for a given wavelength. However, water contamination is the predominant one occurring in the diesel production/supply chain, and the proposed microwave monitoring is interesting in practical application.

Table 4.VIII reports the comparison between the proposed applicator and the literature results. The proposed sensor exhibits the best sensitivity $\Delta|S_{21}|/\Delta\rho$ [96-97].

TABLE 4.VIII
COMPARISON BETWEEN THIS WORK RESULTS AND LITERATURE RESULTS.

References	Sensitivity $\frac{\Delta S_{21} }{\Delta\rho}$ (mdB/ppm)
[96]	0.6
[97]	0.0872
This work	1.42

4.7 Conclusions

A water-in-diesel sensor based on an SIW microwave applicator has been designed, constructed, and characterized. This characterization has confirmed the simulated performances in terms of bandwidth and impedance matching. Five water-contaminated fuel samples have been characterized in terms of dielectric constant frequency dispersion with a SPEAG DAK 3.5 probe. The same samples were detected with the designed SIW applicator allowing a water-in-diesel monitoring with a sensitivity of $\Delta|S_{21}|/\Delta\rho = 1.42 \text{ mdB/ppm}$ at a frequency of $f = 9.76 \text{ GHz}$ with a coefficient of determination $R^2 = 0.94$. The minimum variation in water concentration with the proposed set-up is $\Delta\rho = 7 \text{ ppm}$. The applicator is interesting because it is low-cost and low-profile, and it could be employed with a single frequency source and a microwave power meter.

5 Design of low-cost mini-invasive needle applicators for cancer thermal ablation

5.1 Introduction

IoT networks aim to connect different devices to provide new services to the user. They find many applications, including medicine, for which IoT systems could allow telemedicine, patient monitoring, and mini-invasive operation, oriented to the patient wellness. The development of devices and techniques alternative to the conventional surgery, as the microwave applicator for ablation, allows controlling of a specific parameter as temperature, session time, and power which could be monitored and tuned within a IoT for medicine system.

In this chapter, the design and characterization of low-cost mini-invasive needle applicator prototypes for hyperthermia therapy of cancer are performed, after the investigation of different approaches, focused to increase the device feasibility and miniaturization and to improve patient wellness. The needle applicator is a coaxial antenna operating at frequency $f = 2.45 \text{ GHz}$ in the Industrial, Scientific, and Medical (ISM) frequency band. Many simulations are performed with the aim of investigating different geometries, impedance matching techniques, possible 3D-printing biocompatible materials, and radiating configurations fitting 14-gauge (14G) and 16-gauge (16G) hypodermic tube sizes. Also, a cooling circuit is investigated to maintain the patient healthy tissues at lower temperature, during the ablation session. As last step, prototypes of 14G and 16G applicators have been constructed and characterized.

5.2 Applicators design

The designed microwave (MW) applicator consists of a coaxial antenna working at $f = 2.45 \text{ GHz}$, in the Industrial, Scientific, and Medical (ISM)

frequency band. It is designed for the thermal hepatic tumour ablation [25,26,30,31]; see Fig. 5.1. The design is based on both electromagnetic and thermal simulations, by using the Microwave and Multiphysics modules of CST Studio Suite®. The electromagnetic design of the applicator allows to choose the geometrical parameters values with the aim of minimizing the modulus of the scattering parameter S_{11} . The impedance matching is optimized by varying the geometrical size of the slot, choke, sub-tip. The distribution of the electromagnetic field is also used to evaluate the specific absorption rate (SAR) [98,99]. Thermal design has been carried out considering an in-vivo animal model taking into account blood perfusion effects. Temperature distribution inside the target tissue is estimated via the bio-heat equation (BHE) [100]. The actual volumetric density, heat capacity, thermal conductivity, and blood-flow coefficient of the liver tissue have been considered, as well as the dielectric and physical features of the different materials constituting the applicator.

The effects of a cooling circuit are investigated to minimize the temperature increase of non-target tissues surrounding the external part (called shaft) of the applicator. To allow the antenna to fit a 14G and a 16G metallic hypodermic tube, different radiating sections have been designed. SAR distribution, temperature variation, size, and shape of the ablated zone at $T = 50\text{ }^{\circ}\text{C}$ are simulated and compared for the designed applicators. The thermal lesion shape is identified by isothermal lines at the temperature $T = 50\text{ }^{\circ}\text{C}$.

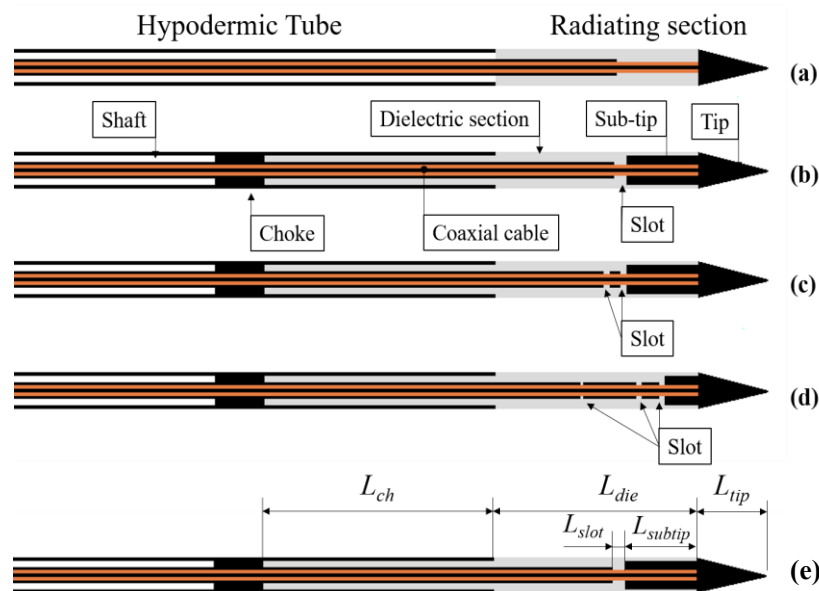


Fig. 5.1. Drafts of the designed applicators: (a) starting, (b) choked single slot, (c) choked double slot, (d) choked triple slot, and (e) dimensions reported in Table 5.I.

Fig. 5.2 shows how lesion diameter and longitudinal length have been determined. Since the ablation region is desired to be as spherical as possible, the axial ratio of the thermal lesion, defined as the ratio of the lesion diameter to the lesion longitudinal length, has been evaluated. The liver tissue is modelled as a cube with side $L_{liver} = 100 \text{ mm}$. The tumour is modelled as a sphere with diameter $d_{tumour} = 15 \text{ mm}$. The dielectric and other physical parameters of hepatic tissue and tumour have been taken from literature [101-103]. However, these features may vary on the patient age, health condition, and gender. In the simulations, the applicator is inserted into the liver tissue cube at depth $D_T = 65 \text{ mm}$.

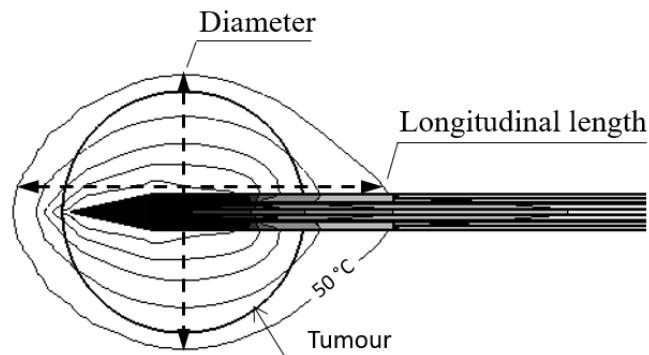


Fig. 5.2. Scheme of the ablation zone. The 50 °C isothermal lines determinate the boundary of the thermal lesion.

5.2.1 Geometrical investigation

The draft of the first designed applicator is shown in Fig. 5.1(a). It consists of a coaxial antenna soldered to a metallic conical tip. The radiating section is covered by a dielectric biocompatible material to help applicator insertion into the biological tissue. It also provides mechanical protection, avoids the adhesion to the necrotized tissue, and improves power coupling with the biological medium. The considered dielectric material is polytetrafluoroethylene (PTFE). The non-radiating section is inserted into a steel hypodermic tube (shaft) to form a triaxial configuration [25]. It also gives robustness to the applicator. The parameters for the applicators are listed in Table 5.I. Their values are identified after several preliminary simulations and by considering fabrication constraints. The applicator lengths are shown in Fig. 5.1(e).

TABLE 5.I
NOMINAL VALUES FOR THE PARAMETERS OF THE 16G APPLICATOR

Parameter	Nominal value (mm)	Description
L_{tip}	5	Tip length
L_{sh}	200	Shaft length
L_{die}	15	Dielectric section length
L_{coax}	215	Coaxial cable length
L_{slot}	1	Gap between the tip base and the coaxial outer conductor into the dielectric section
L_{subtip}	5	Sub-tip length
L_{ch}	21.1	Choke length
r_{tip}	0.86	Base tip radius
r_{die}	0.86	Dielectric section radius
$r_{in,sh}$	0.70	Shaft inner radius
$r_{out,sh}$	0.86	Shaft outer radius
r_{cable}	0.3935	Coaxial cable outer conductor maximum radius
$r_{out,coax}$	0.3013	Coaxial cable outer conductor minimum radius
$r_{in,coax}$	0.1016	Coaxial cable inner conductor radius

5.2.1.1 16G applicator

Fig. 5.3 shows the modulus of the scattering parameter S_{11} vs. the frequency f for the starting applicator reported in Fig. 5.1(a), for different L_{slot} values. As expected, the value and the position of the minimum of modulus of the scattering parameter S_{11} varies with L_{slot} . The slot is the antenna aperture providing the electromagnetic power irradiation, its optimal length is strictly related to the operating wavelength, the dielectric properties of the materials, the biological load.

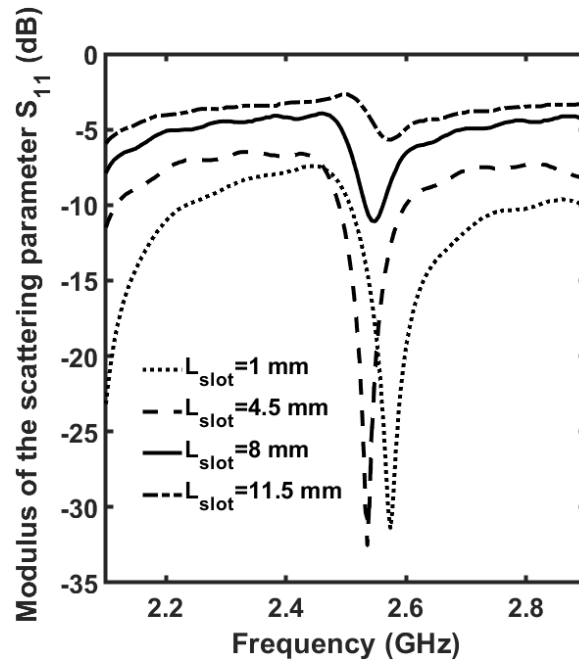


Fig. 5.3. Modulus of the simulated scattering parameter S_{11} vs. frequency f , for different L_{slot} values. Starting designed 16G MW applicator, Fig. 5.1(a).

Since the metallic shaft causes undesired coupling with the external conductor of the coaxial cable, a choke balun has been introduced, by soldering the hypodermic tube inner surface and the outer conductor of the coaxial cable at a distance of one-quarter wavelength from the radiating section [102], as shown in Fig. 1(b). This configuration improves axial ratio and homogeneity of the thermal lesions and aids the impedance matching. Fig. 5.4 reports the modulus of the scattering parameter S_{11} as a function of the frequency f for different L_{slot} values, for the choked applicator. The best result corresponds to $L_{slot} = 8$ mm (solid curve). However, the minimum S_{11} does not correspond to the desired frequency $f = 2.45$ GHz. Therefore, further refinements must be considered.

A steel cylinder covering the coaxial cable in the radiating section, called *sub-tip* [102,104], with length $L_{subtip} = 5$ mm, has been added to maximize power delivery to under treatment tissues, see Fig. 5.1(b). Fig. 5.5 illustrates the modulus of the scattering parameter S_{11} as a function of the frequency f for different values of L_{slot} , for the choked applicator with sub-tip. The best impedance matching occurs for $L_{slot} = 1$ mm. The simulation for an *in-vivo* model is performed to evaluate the thermal behaviour of the optimized applicator.

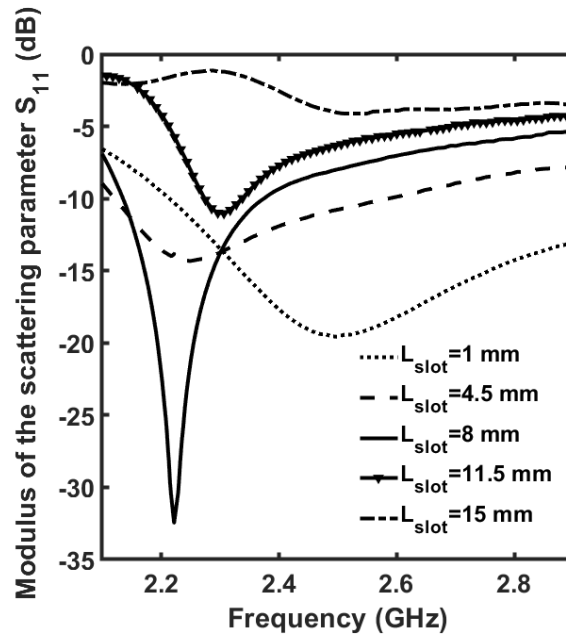


Fig. 5.4. Modulus of the simulated scattering parameter S_{11} vs. frequency f , for different L_{slot} values. Choked applicator 16G MW applicator.

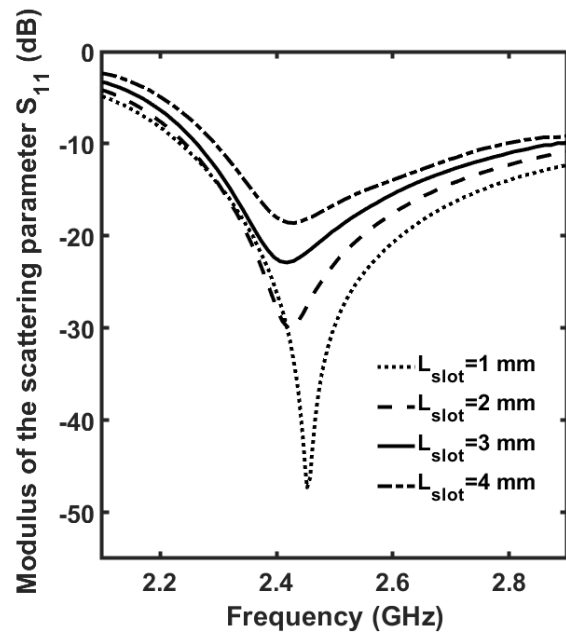


Fig. 5.5. Modulus of the simulated scattering parameter S_{11} vs. frequency f , for different L_{slot} values. 16G MW applicator, Fig. 5.1(b).

Fig. 5.6 shows the longitudinal (up) and transversal (down) distribution of the temperature after an ablation time duration $t = 200$ s. The simulation is carried out considering an average input power $P_{avg} = 20$ W. The suitable input average power P_{avg} should be chosen considering the desired thermal lesion size. By

simulation results, the minimum average power to ablate the whole cancer sphere of diameter $d_{tumour} = 15\text{ mm}$ is $P_{avg} = 20\text{ W}$, since the thermal lesion is defined with the isothermal line at $T = 50^\circ\text{ C}$. This value is identified via a number of simulations by increasing the input average power in the range from $P_{avg} = 2\text{ W}$ to $P_{avg} = 30\text{ W}$. The choked applicator has a simpler geometry than that of the choked applicator with sub-tip. It has been investigated with the aim to identify an easier construction geometry. However, its response is strongly affected by slot length. Consequently, the optimized choked applicator with sub-tip has been considered.

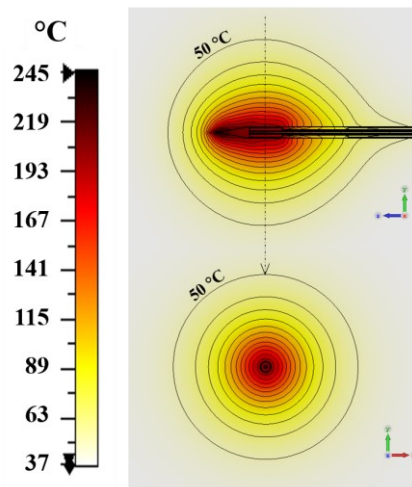


Fig. 5.6. Temperature distribution simulated into the hepatic tissue after an ablation time duration $t = 200\text{ s}$, for average power $P_{avg} = 20\text{ W}$. 16G MW applicator, Fig. 1(b).

5.2.1.2 14G applicator

An antenna to fit a 14G hypodermic tube has been investigated, to reduce construction costs, while obtaining comparable performances and maintaining mini-invasive design. Its slightly bigger radius allows a simpler assembly operation and an easier implementation of a cooling circuit. The 14G hypodermic tube has inner radius $r_{in,sh} = 0.87\text{ mm}$ and outer radius $r_{out,sh} = 1.1\text{ mm}$. Three multi-slot applicators have been designed: choked single, double, and triple slot antennas, illustrated in Fig. 5.1(b), 5.1(c) and 5.1(d), respectively. They have been optimized and their performances in terms of impedance matching with the biological tissue and axial ratio of the thermal lesion are compared with the 16G choked single slot applicator.

Fig. 5.7 shows the comparison of the modulus of the scattering parameters S_{11} for the three geometries of the 14G applicator and the single slot 16G applicator; the simulated scattering parameters at $f = 2.45\text{ GHz}$ are $S_{11} =$

-28.75 dB , $S_{11} = -56.43 \text{ dB}$, and $S_{11} = -39.55 \text{ dB}$, $S_{11} = -47.34 \text{ dB}$ for 14G choked single slot, 14G double slot, 14G triple slot, and 16G single slot antennas respectively. The ablated zone sizes for single, double, and triple configurations as a function of the ablation time duration t has been evaluated via an accurate simulation.

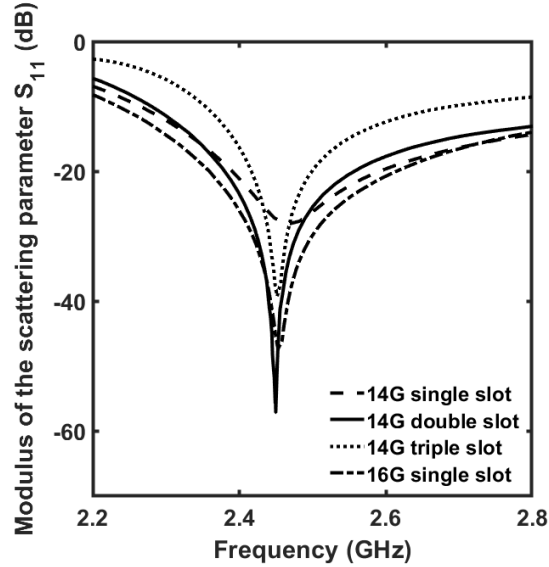


Fig. 5.7. Modulus of the simulated scattering parameter S_{11} vs. frequency f , average input power $P_{avg} = 20 \text{ W}$. 16G MW applicator, Fig. 1(b) vs. 14G MW applicator, Fig. 1(b), 14G MW applicator, Fig. 1(c), and 14G MW applicator, Fig. 1(d).

Fig. 5.8 shows the axial ratio for the three configurations as a function of the ablation ratio for the three configurations as a function of the ablation time duration t , when the applicator is fed by an average input power $P_{avg} = 20 \text{ W}$. The 14G single slot and the 14G double slot applicators allow an axial ratio bigger than that obtained with the 14G triple slot one, whereas the 16G single slot antenna shows the best result. The 14G applicator demonstrates a good impedance matching with the biological load also when the tumour diameter varies. The applicator impedance matching when it is inserted into four different tumour diameters is depicted in Fig. 5.9.

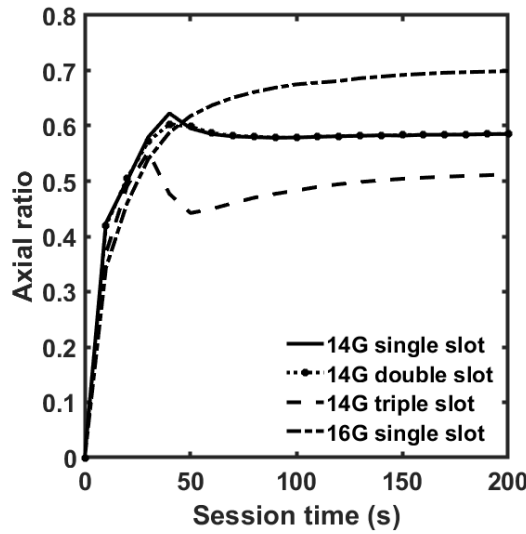


Fig. 5.8. Simulated axial ratio of the thermal lesion vs. ablation time duration t , average input power $P_{avg} = 20 W$. 16G MW applicator, Fig. 5.1(b) vs. 14G MW applicator, Fig. 5.1(b), 14G MW applicator, Fig. 5.1(c), and 14G MW applicator, Fig. 5.1(d).

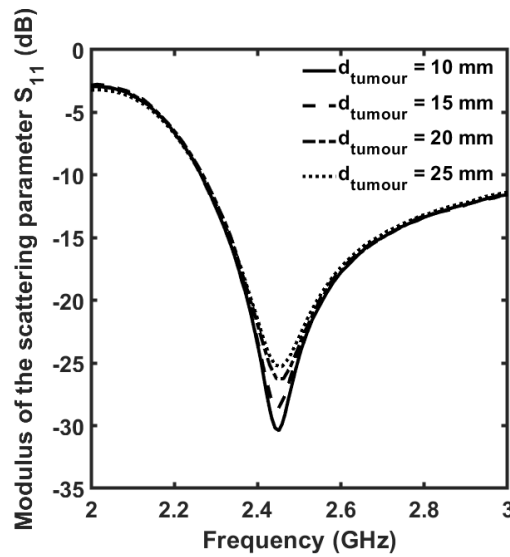


Fig. 5.9. Modulus of the simulated scattering parameter S_{11} vs. frequency f , for different tumour diameters d_{tumour} . 14G MW applicator, Fig. 5.1(b).

5.2.2 Dielectric materials: analysis and characterization

In the simulations, PTFE with a nominal permittivity of $\epsilon_r = 2.1$ is used for the dielectric section. However, to evaluate the possibility of fabricating this section by 3D-printing technology, the effects of the changes in the physical parameters of the dielectric section on the applicator performance have been examined. In particular, the dielectric constant ϵ_r , thermal conductivity k and thermal capacity c variations have been investigated.

5.2.2.1 Study on the permittivity of the dielectric section

Changes in the dielectric constant of $\pm 20\%$ around the nominal value $\epsilon_r = 2.1$ is examined. The geometrical dimensions of the applicator are $r_{in,sh} = 0.87 \text{ mm}$, $r_{out,sh} = 1.1 \text{ mm}$, $r_{in,coax} = 0.1767 \text{ mm}$, $r_{out,coax} = 0.4825 \text{ mm}$, $r_{cable} = 0.595 \text{ mm}$, $r_{tip} = 1.1 \text{ mm}$, and $L_{slot} = 1 \text{ mm}$. Fig. 5.10 shows the modulus of scattering parameter S_{11} as a function of frequency f , when different dielectric section permittivity ϵ_r values are considered. A bigger dielectric constant allows smaller devices. For the permittivity value of $\epsilon_r = 2.52$ a suitable choke length, equal to $L_{ch} = 19.1 \text{ mm}$ is identified, instead of $L_{ch} = 21.1 \text{ mm}$ identified for $\epsilon_r = 2.1$ for the same operation frequency $f = 2.45 \text{ GHz}$.

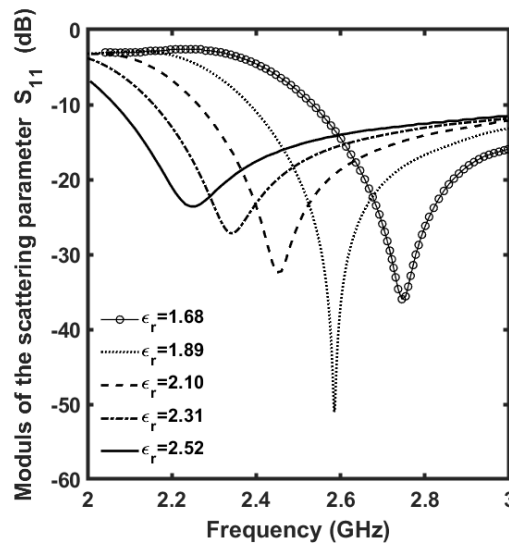


Fig. 5.10. Modulus of the simulated scattering parameter S_{11} vs. frequency f , as the dielectric section permittivity varies. 14G MW applicator, Fig. 5.1(b).

5.2.2.2 Study on the thermal conductivity and capacity of the dielectric section

The effects of the change in the thermal conductivity and capacity of $\pm 10\%$ around the nominal values of $k = 0.2 \text{ W m}^{-1}\text{K}^{-1}$ and $c = 1 \text{ kJ K}^{-1}\text{kg}^{-1}$ are examined. The geometrical dimensions of the applicator are the same of the section 5.2.2.2. Fig. 5.11 depicts the dimensions and axial ratio of the thermal lesion as a function of the ablation time duration t , when different thermal conductivity k values are considered, keeping the thermal capacity c constant at the nominal value. Fig. 5.12 depicts the dimensions and axial ratio of the thermal lesion as a function of the ablation time duration t , when different thermal capacity c values are considered, keeping the thermal conductivity k constant at the nominal value. By considering the thermal lesion sizes and the axial ratio at session time $t = 200 \text{ s}$, the following evidences can be observed:

- i) for an increase of +10% of thermal conductivity k , an increase of +1.7% of the thermal lesion longitudinal length is obtained, the diameter of the thermal lesion does not vary, thus the axial ratio decreases of -1.07%;
- ii) for an increase of +10% of the thermal capacity c an increase of +1.05% of the thermal lesion longitudinal length and of +0.65% of the thermal lesion diameter is obtained, thus the axial ratio increases of +0.4%.

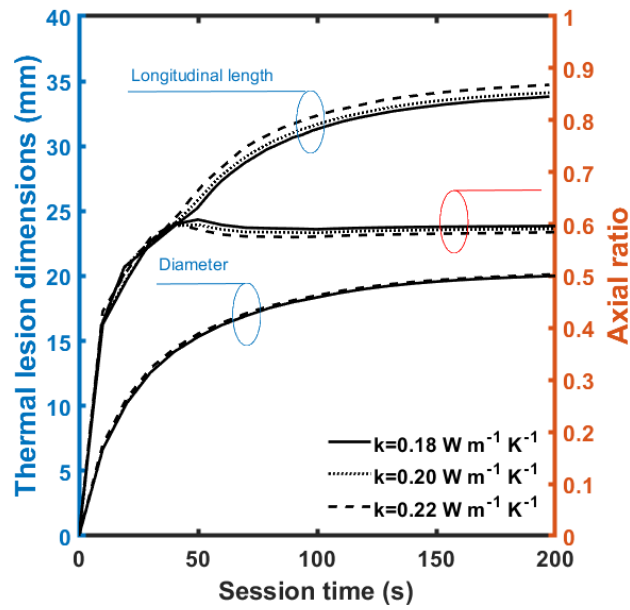


Fig. 5.11. Simulated dimensions and axial ratio of the thermal lesion vs. ablation time duration t , for different values of thermal conductivity k ; $c = 1 \text{ kJ K}^{-1} \text{ kg}^{-1}$; average power $P_{avg} = 20 \text{ W}$. 14G MW applicator, Fig. 5.1(b).

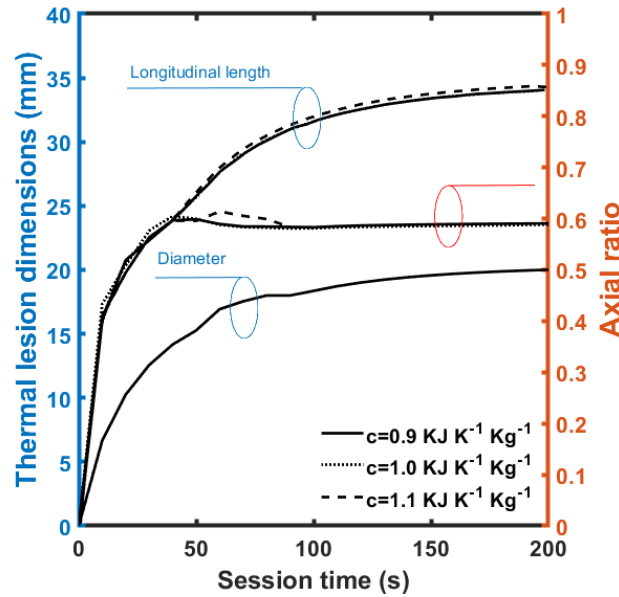


Fig. 5.12. Simulated dimensions and axial ratio of the thermal lesion vs. the ablation time duration t , for different values of thermal capacity c ; $k = 0.2 \text{ W m}^{-1}\text{K}^{-1}$; average power $P_{avg} = 20 \text{ W}$. 14G MW applicator, Fig. 5.1(b).

5.2.2.3 Study on the material of the dielectric section

To evaluate the feasibility of ad-hoc constructed dielectric sections, the E-Shell 300 biocompatible 3D printing material is considered instead of the PTFE. The new material has been characterized, via a dielectric measurement set-up based on open-ended coaxial probes, SPEAG DAK probe, and a vector network analyser (VNA) Field Fox Keysight Technologies [92,93]. The measured real permittivity and loss tangent of the E-Shell 300 in the frequency range $f = 2 - 3 \text{ GHz}$ are $\epsilon_r = 2.73$ and $\tan\delta = 0.0278$. Fig. 5.13 shows the simulated modulus of scattering parameter S_{11} as a function of the frequency f , for the dielectric section made of PTFE (solid curve) and the E-Shell 300 series (dash-dot curve). The impedance matching with E-Shell 300 has been optimized, varying the choke length L_{ch} . The minimum of the scattering parameter is $S_{11} = -27.2 \text{ dB}$, for $L_{ch} = 18 \text{ mm}$. Fig. 5.14 shows the axial ratio of the thermal lesion as a function of the ablation time duration t . It is bigger for the PTFE case, allowing a thermal lesion closer to a theoretical sphere. This condition is more convenient, because allows to avoid damage of healthy tissue along the needle applicator.

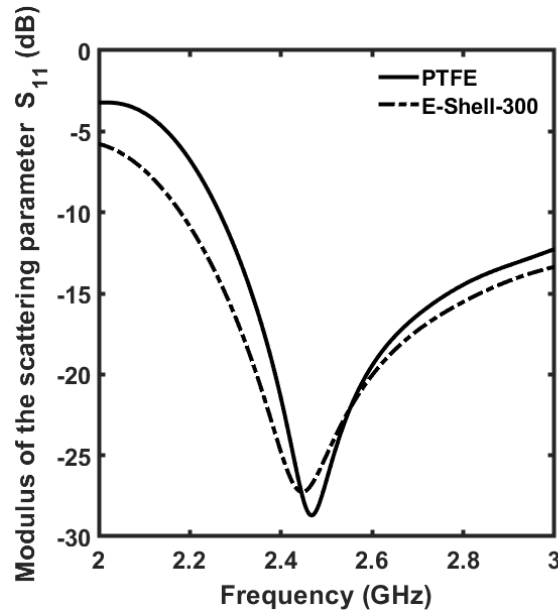


Fig. 5.13. Modulus of the simulated scattering parameter S_{11} vs. frequency f , for PTFE (solid curve) and E-Shell 300 (dash-dot curve). 14G MW applicator, Fig. 5.1(b).

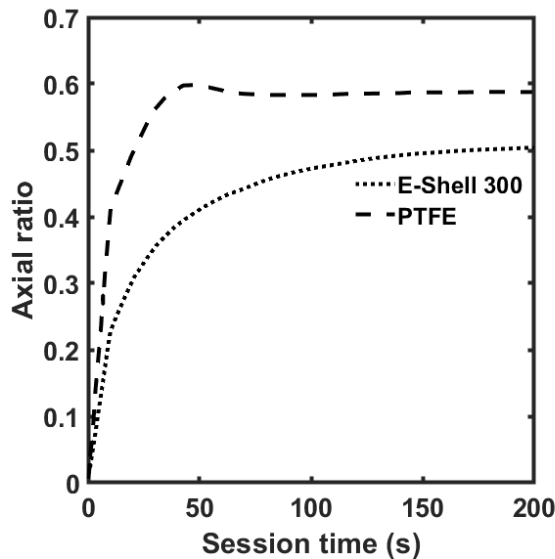


Fig. 5.14. Simulated axial ratio of the thermal lesion vs. ablation time duration t , average power $P_{avg} = 20 W$. 14G MW applicator, Fig. 5.1(b).

5.2.3 Influence of the cooling circuit on microwave heating

To improve the axial ratio of the ablation zone by minimizing the harmful overheating of the biological tissue adjacent to the shaft, caused by the by thermal propagation and by the formation of parasite currents, a cooling circuit has been considered. The cooling is typically obtained with the flow of a refrigerant fluid in cooling channels located into the hypodermic tube. In particular, an

open-loop cooling circuit, employing a peristaltic pump and allowing a suitable flux of saline solution, is designed in order to stabilize the temperature at $T = 37^\circ\text{C}$ in the needle shaft. In the simulations, the cooling circuit model has been approximated with an ideal constant temperature source put into the hypodermic tube. In particular, the cooled region goes from the microwave generator to the choke, i.e., the area to the left of the choke in Fig. 5.1(b), Fig. 5.1(c), and Fig. 5.1(d). The considered cooling fluid is water with a temperature fixed to $T_b = 37^\circ\text{C}$, close to the normal body temperature. The effects of the cooling circuit on the thermal performance of the 14G and 16G single slot microwave applicators of Fig. 5.1(b) have been evaluated by simulations with and without the cooling circuit.

Fig. 5.15 shows the isothermal curves simulated in the case of the 14G applicator. The thermal lesion shape obtained for the needle with cooling circuit is more spherical (Fig. 5.15(a)) than that pertaining to other case (Fig. 5.15(b)), where the typical comet-tail profile can be observed. To further increase the thermal lesion sphericity, the simulated cooling circuit has been extended to the radiating section.

Temperature distribution, shape and dimensions of the thermal lesion change due to the extended cooling circuit increase as shown in Fig. 5.16. The axial ratio for the applicator with extended cooling circuit is $AR = 0.73$. The sequence of the investigation results reported in the previous sections A-C constitute the basis of a *trial-and-error* design approach, allowing to optimize the geometries of these antennas.

In Table 5.II, the simulation results related to all designed applicators are reported. The choked single slot with sub-tip version is chosen for the construction.

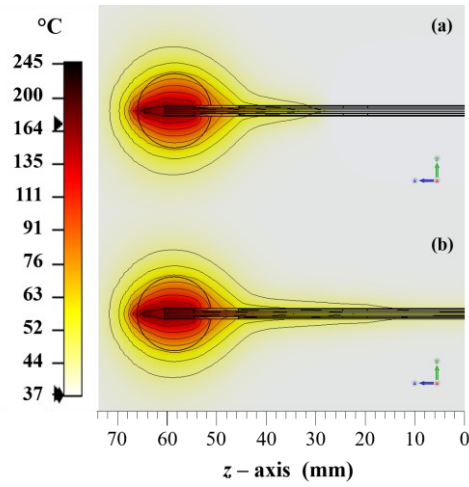


Fig. 5.15. Temperature distribution of the irradiated tissue simulated in the longitudinal section with an average power in input of $P_{avg} = 20 W$. 14G microwave applicator, Fig. 5.1(b), (a) with and (b) without cooler circuit.

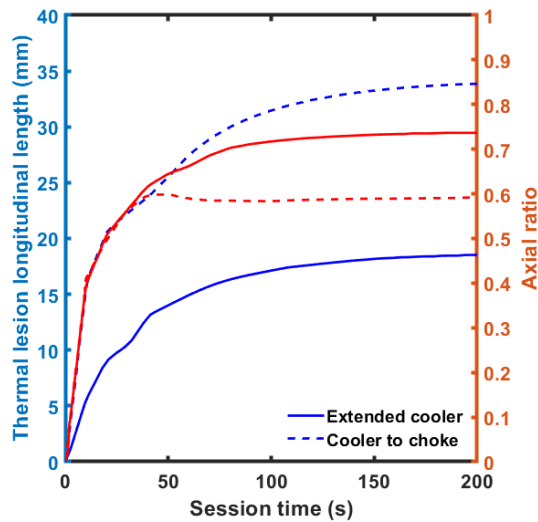


Fig. 5.16. Simulated longitudinal length and axial ratio of the thermal lesion vs. ablation time duration t of the 14G MW applicator, Fig. 5.1(b), with cooler stopped at choke (dashed line) and extended at slot (continuous line), average power $P_{avg} = 20 W$.

TABLE 5.II
SIMULATION RESULTS WITH DIFFERENT ANTENNA GEOMETRIES

Parameter	Type of applicator				
	16G single slot	14G single slot	14G single slot with E-shell 300	14G dual slot	14G triple slot
Minimum scattering parameter modulus (dB)	-47.3	-28.7	-27.2	-56.4	-39.6
Maximum SAR (averaged over the mass $m = 1\text{ g}$, at $P_{avg} = 20\text{ W}$) (kW/kg)	5.61	5.19	5.12	5.12	4.97
Maximum temperature (at $P_{avg} = 20\text{ W}$, $t = 200\text{ s}$) ($^{\circ}\text{C}$)	244	184	172	182	175
Lesion longitudinal length (at $P_{avg} = 20\text{ W}$, $t = 200\text{ s}$) (mm)	36.7	34.2	39.0	34.3	39.2
Lesion diameter (at $P_{avg} = 20\text{ W}$, $t = 200\text{ s}$) (mm)	28.2	20.0	19.8	20.1	20.1
Axial Ratio (at $P_{avg} = 20\text{ W}$, $t = 200\text{ s}$) (mm)	0.77	0.58	0.51	0.59	0.51

5.3 Expertiment and prototype characterization

The Micro-Coax UT047C-ULL cable has been chosen for the 14G prototype fabrication. Its nominal radius $r_{cable} = 0.595\text{ mm}$ allows to fit it in the hypodermic tube of 14 gauge. Moreover, the low loss ultralow density PTFE (ULD PTFE) of the dielectric part permits a more thermal stability than solid PTFE, lowering of the power dissipations. This coax cable resists to an operating temperature until $T_{max} = 250\text{ }^{\circ}\text{C}$. The antenna was fabricated by stripping the cable shielding conductor to make the slot and soldering the internal conductor to the metallic tip. The applicator radiating part was embedded in a tube of PTFE. The modulus of the measured scattering parameter S_{11} as a function of the frequency for various biological load conditions is shown in Fig. 5.17, with a biological load located from the tip till the radiating slot (dashed line), with a biological load located on overall the radiating part till the shaft (continuous line) and by immersing the prototype in a water filled vessel (dot line). In particular, the biological load was obtained by keeping the applicator between hand fingers, with

the aim of a preliminary characterization close to the in-vivo condition. The impedance matching is good, also changing load conditions. In the best load condition, the modulus of the scattering parameter measured at the operating frequency $f = 2.45 \text{ GHz}$ was $|S_{11}| \approx -40 \text{ dB}$.

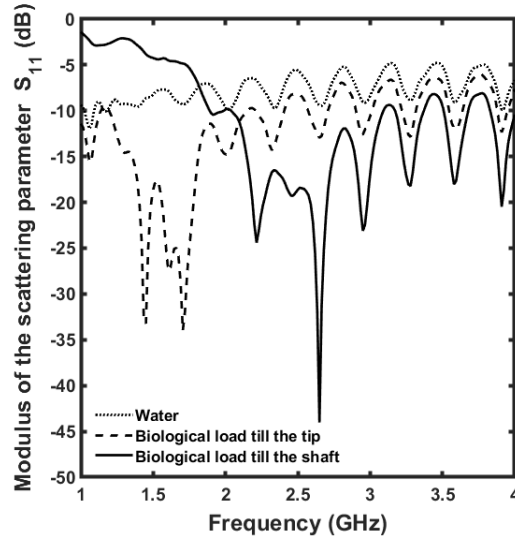


Fig. 5.17. Characterization of the 14G MW applicator prototype, Fig. 5.1(b). Measured modulus of the scattering parameter S_{11} vs. frequency for different biological load.

The applicator is put into a bovine liver and fed by a MW source with an average power $P_{avg} = 10 \text{ W}$ for 180 seconds, to carry out the *ex-vivo* validation. The obtained thermal lesion, identified by the tissue discolouration caused by the high temperature, is shown in Fig. 5.18. The decolorated area has longitudinal length of 32 mm , diameter of 19 mm , and axial ratio $AR = 0.59$, in good agreement with simulations. The microwave applicator designed provides good results. Ablation zone with well-defined contours into the biological tissue can be achieved by controlling the temperature increase. The surrounding healthy tissues are not damaged by the ablation session, confirming that this method preserves mini-invasive and patient wellness-oriented characteristics. Almost coincident performances are found for the smaller 16G prototype, fed by Micro-Coax UT-031-LL coaxial cable. Further improvements can be achieved employing a double source system, e.g., by including a fiber laser source in the medium infrared (Mid-IR) wavelength range, where the biological tissues exhibit strong absorption [28-30], and by introducing a temperature monitor system based, as example, on optical fiber sensor [106].



Fig. 5.18. Characterization of the 14G MW applicator prototype, Fig. 1(b). Measured modulus of the scattering parameter S_{11} vs. frequency for different biological load.

5.4 Conclusions

An extensive analysis of various design solutions aimed to the fabrication of low-cost MW needle applicators for hyperthermia tumour therapy was proposed. 14G and 16G MW applicator prototypes are designed, fabricated, and characterized. Their employment can be considered as a good alternative to surgical resection, reducing side effects to healthy tissues and increasing patient wellness, as mini-invasive approach. The 14G applicator having relatively larger size is simpler to be constructed and allow a cost reduction during its mechanical assembling. The simplified geometry, obtained with the fabrication of a proper dielectric section via 3D printing technique, allows a cost reduction also in the case of the most compact 16G version. Further point of investigation to be developed in the future consists in the design of an optical fiber temperature sensor to be integrated with the MW applicator for an accurate thermal monitoring of the ablation session in real-time.

6 Design of a Split Ring Resonator-based metamaterial for microwave impedance matching with biological tissue

6.1 Introduction

Metamaterials can be employed in the 5G and beyond 5G communication systems with different aims including the optimization of the antenna radiation properties via metamaterial lens and the development of novel reflective and reconfigurable intelligent surfaces (RIS). They can also be employed to miniaturize antennas keeping comparable performances.

In this chapter, a metamaterial lens based on a split ring resonator (SRR) array has been designed and optimized to improve the focusing and the penetration depth in human biological tissue of a microwave beam irradiated by a substrate integrated waveguide (SIW) cavity backed patch antenna. The impedance matching of the antenna loaded with human tissue is strongly improved. The device could be promising in medicine applications exploiting the IoT approach as illustrated in the previous Chapter 5.

The simulations have been performed by using CST Microwave Studio®. A prototype of the device has been fabricated with the printed board circuits (PCB) process and has been characterized using a VNA and an antenna measurement system in anechoic chamber. A novel microwave applicator for hyperthermia therapy of skin cancer could be developed. The performances of the proposed applicator have been evaluated in terms of measured S_{11} scattering parameter modulus and simulated power loss density. The obtained results indicate that an SRR-based metamaterial is a promising solution for external microwave applicators to employ in dermatology.

The theoretical model for the metamaterial design is reported in paragraph 2.2.

6.2 Microwave applicator design

The considered microwave applicator, depicted in Fig. 6.1, is an SIW cavity-backed patch antenna, designed and optimized for Ku-Band applications (10.7–12.7 GHz). It consists of a stack structure: a microstrip patch antenna coupled with a circular resonant cavity based on SIW technology. The substrate Rogers duroid RT/5880 with low dielectric constant $\epsilon_r = 2.2$ and low losses $\tan \delta = 0.0009$ has been considered for both layers. This antenna combines the attractive features of both SIW cavity-backed and patch antennas with truncated corners. The design has been performed by varying the size of the cavity, the hole diameters, the hole pitch, and the patch geometry. All the details pertaining to designs of this kind of antenna are reported in [9]; they are not reported for shortness. The two cuts on the sides of the rectangular patch were designed to provide a wider frequency band and a frequency downshift. This allows a more compact size. The metallized cavity further broadens the bandwidth and improves the gain of the antenna; furthermore, the SIW technology offers the typical advantages of the standard PCB processes, such as easiness of fabrication, low cost, compact size, and high integration with the planar circuits. Fig. 6.2 shows the layout of an SIW cavity-backed patch antenna, the geometric parameters of which are listed in Table 6.I.

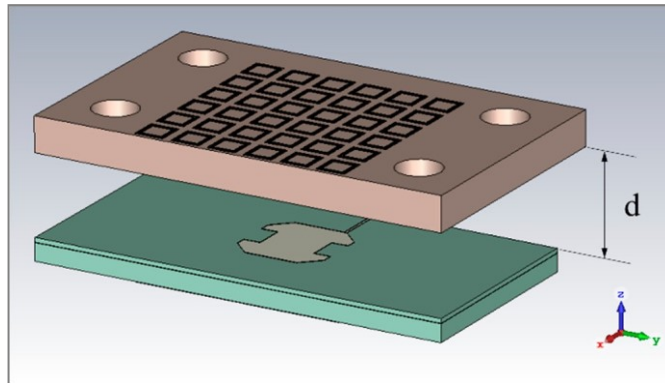


Fig. 6.1. Layout 3D view of the microwave applicator with the split ring resonator-based metamaterial superstrate placed on the substrate integrated waveguide (SIW) cavity-backed patch antenna at a distance d .

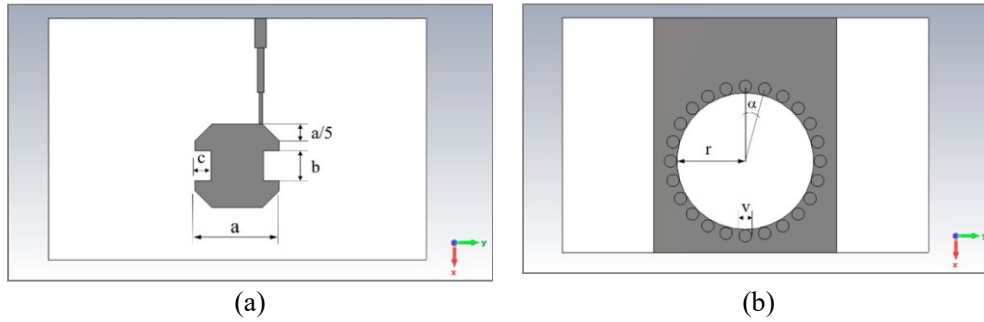


Fig. 6.2. Layout of SIW cavity-backed patch antenna. (a) Top view of the patch antenna and (b) top view of the SIW circular resonant cavity.

The metamaterial theory reported in Section has been applied to roughly identify the geometric parameters of the metamaterial operating at the Ku-band. The analytical model for simple split ring resonators has been employed in order to obtain simple and preliminary line guides for the actual design, which is numerically performed via CST Microwave Studio. The employed dielectric substrate is Rogers RO4350B with dielectric constant $\epsilon_r = 3.48$ and dissipation factor of $\tan \delta = 0.004$.

The geometry of the SRR unit cell has been suitably modified and scaled with respect to the literature [82] in order to operate at the resonance frequency of the SIW microwave applicator. Moreover, with respect to [82], the unit cell of the proposed SRR presents a further double ring with splits placed on the opposite side and operates at a different frequency. A complementary configuration, i.e., a couples of coplanar rings written symmetrically with respect to the common center, has been considered to obtain a resonance frequency close to that of a single ring with the same dimensions, but with a larger magnetic moment due to higher current density. Since they are written on both sides of a dielectric substrate, they are broadside coupled. The analytical model of a single (not complementary) broadside coupled SRR satisfactorily approximates the complementary configuration when the couple of rings are very close each other. The metamaterial considered in this paper consists of an array of complementary broadside coupled split square-rings. The lattice of this inhomogeneous structure is shorter than the guided wavelength of antenna radiation, so the composite behaves as an effective homogeneous medium.

The design and optimization of the metamaterial lens has been numerically performed via CST Microwave Studio®. After several simulations, in which the SRR geometry and cell size have been parametrically changed, the optimized

geometric parameters are listed in Table 6.II. The optimized SRR metamaterial exhibits resonant frequency range overlapping the operating frequency range of the SIW cavity-backed patch antenna. Fig. 6.3 shows the 3D view (a) and plan front view (b) of the unit cell of the SRR, respectively. The metamaterial lens used as superstrate of the SIW cavity-backed patch antenna is shown in Fig. 6.4.

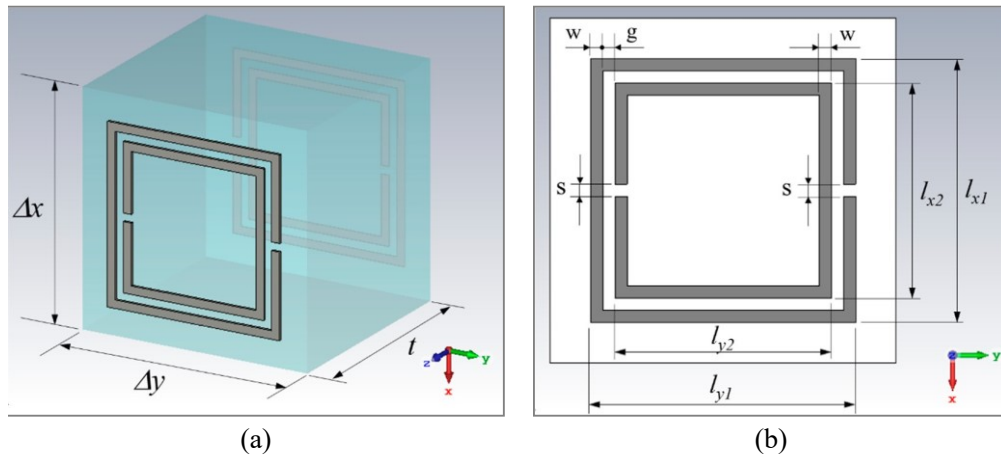


Fig. 6.3. 3D model of complementary broadside coupled SRR unit cell designed in CST Microwave Studio®. (a) 3D view and (b) top view.

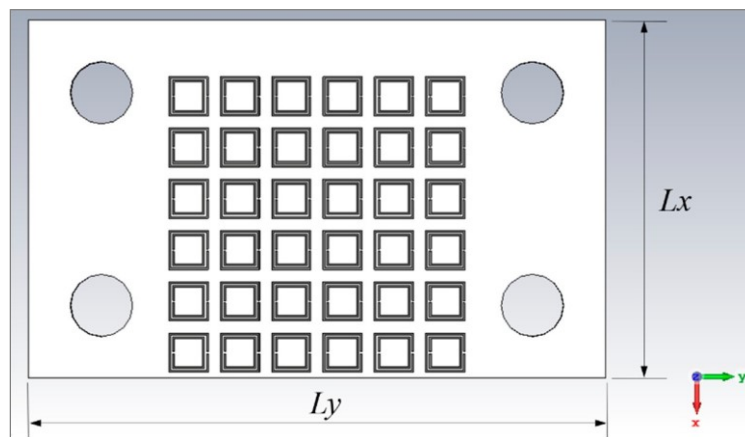


Fig. 6.4. Layout of the SRR metamaterial placed as the patch antenna superstrate.

The scattering parameter S_{11} of the microwave applicator placed at distance D from a model of human tissue is simulated to evaluate the lens metamaterial behavior as impedance matching layer. Fig. 6.5 shows the sideview of the layout of SIW cavity-backed patch antenna covered by the metamaterial lens and at distance D from the biological tissue. The biological tissue considered in the

simulation is a slab of skin-fat-muscle, whose electromagnetic parameters at the $f = 11 \text{ GHz}$ frequency are listed in Table 6.II [106].

TABLE 6.I
LIST OF THE GEOMETRIC PARAMETERS OF THE SRR UNIT CELL OF FIGS. 6.1, 6.3, AND 6.4.

Symbol	Value (mm)	Description
Δx	3.20	Length of the unit cell in the x direction
Δy	3.20	Length of the unit cell in the y direction
l_{x1}	2.45	Length of the external SRR in the x direction
l_{y1}	2.45	Length of the external SRR in the y direction
l_{x2}	2.00	Length of the internal SRR in the x direction
l_{y2}	2.00	Length of the internal SRR in the y direction
s	0.11	Split gap of the SRR
w	0.11	Width of the SRR
g	0.11	Distance between the complementary SRRs in the xy plane
t	3.04	Distance between the broadside coupled SRRs in the z direction
d	6.90	Distance between the SIW antenna and the metamaterial lens
L_x	22.40	Length of the metamaterial lens in the x direction
L_y	36.00	Length of the metamaterial lens in the y direction

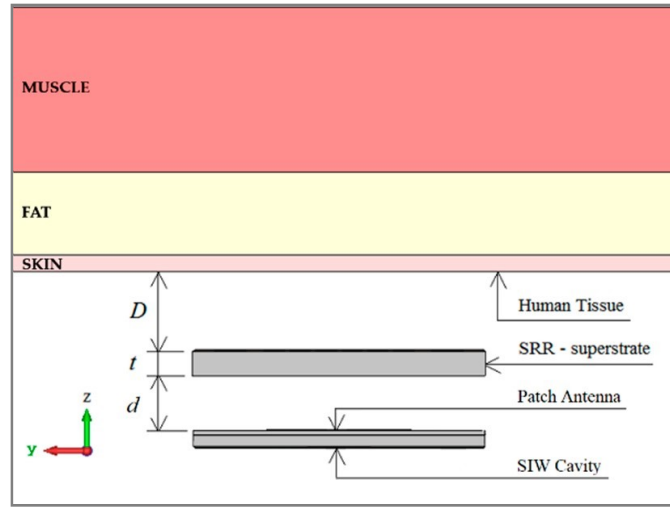


Fig. 6.5. Sideview of SIW cavity-backed patch antenna with SRR superstrate placed at distance D from human tissue.

TABLE 6.II
ELECTROMAGNETIC PARAMETERS OF HUMAN TISSUES AT $f = 11 \text{ GHz}$

Biological Tissue	El. Conductivity (σ) ($S \cdot m^{-1}$)	Permittivity (ϵ_r)
Skin	9.1658	30.313
Fat	0.6567	4.5278
Muscle	12.083	41.419

The scattering parameter modulus $|S_{11}|$ of the SIW cavity-backed patch antenna with SRR superstrate has been simulated for different distances from the biological tissue, and the obtained results are compared in Fig. 6.6(a). It is apparent that the metamaterial placed at distance $D = 10 \text{ mm}$ allows the best impedance matching with the biological tissue. It is worthwhile noting that even if Fig. 6.6(a) shows a narrow dip at $f = 10.9 \text{ GHz}$, the overall operating bandwidth is typically defined at $|S_{11}| = -10 \text{ dB}$ level. Therefore, a very large frequency range of about 2 GHz can be exploited.

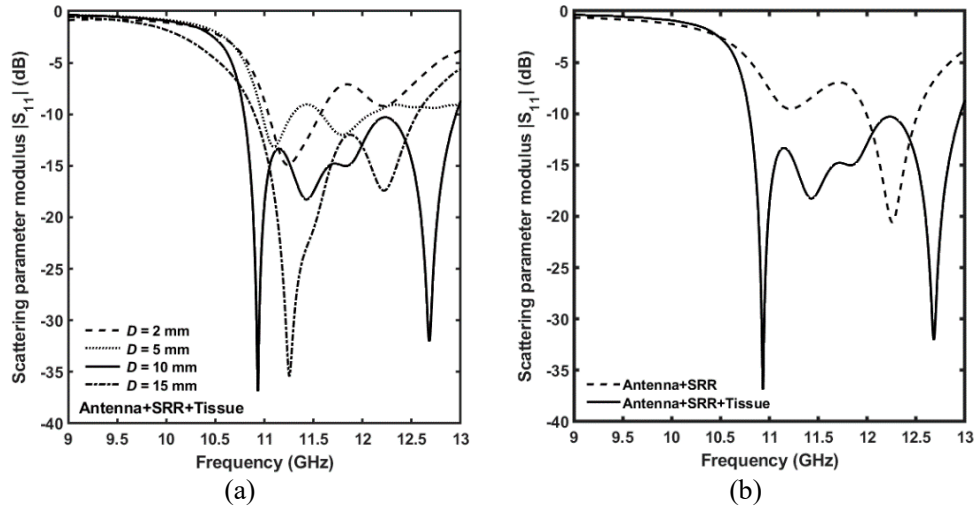


Fig. 6.6. Simulated scattering parameter modulus $|S_{11}|$ (a) of the SIW cavity-backed patch antenna with SRR superstrate placed at different distances from the biological tissue and (b) of the SIW cavity-backed patch antenna with SRR superstrate placed at distance $D = 10$ mm from the human tissue (continuous line) and of the SIW cavity-backed patch antenna with SRR superstrate without tissue (dashed line).

By considering the strong change of scattering parameter modulus $|S_{11}|$ with respect to the distance D , the following considerations can be inferred:

- (i) the distance D change induces the radiation impedance transformation of the applicator;
- (ii) the distance D could be optimized starting from the nominal value of $D = 10$ mm, by considering the particular biological tissue;
- (iii) suitable mechanical spacers could be finely controlled, e.g., by ad-hoc dielectric screws to optimize the microwave radiation.

Fig. 6.6(b) illustrates the simulated scattering parameter modulus $|S_{11}|$ of the SIW cavity-backed patch antenna with SRR superstrate placed at distance $D = 10$ mm from the human tissue (continuous line) and of the SIW cavity-backed patch antenna with SRR superstrate without tissue (dashed line). The reduction in the scattering parameter modulus $|S_{11}|$ can be observed over almost the entire frequency range, the metamaterial strongly improves the impedance matching.

The electric field distribution has been simulated in order to evaluate the ability of the proposed microwave applicator to focus the electromagnetic field into biological tissue. Simulated electric field 2D distribution in the yz plane at $f = 11$ GHz is reported in Fig. 6.7.

The metamaterial lens produces a focusing improvement of the electromagnetic field into the skin model. In particular, in the case of SRR superstrate

placed at distance $D = 10 \text{ mm}$ from the human tissue, the electric field modulus better penetrates along z -direction, in both the skin and fat layers, with respect to the case without SRR superstrate. Moreover, the region where the electric field modulus is close to $|E| = 300 \text{ Vm}^{-1}$ is more homogeneous in the presence of SRR superstrate (Fig. 6.7(a)). It is worth noting the nodal surfaces due to a stationary electromagnetic wave in absence of SRR metamaterial (Fig. 6.7(b)).

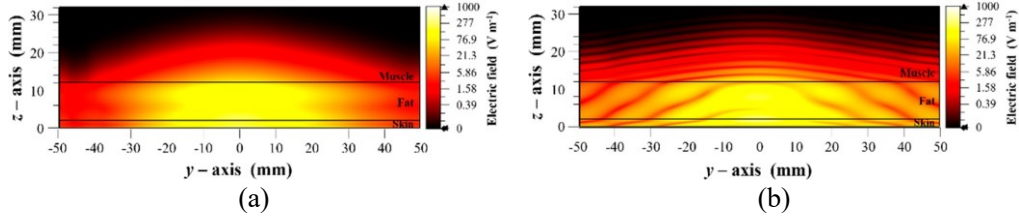


Fig. 6.7. Simulated electric field 2D distribution in the yz plane at the frequency $f = 11 \text{ GHz}$; (a) SIW cavity-backed patch antenna with SRR superstrate placed at distance $D = 10 \text{ mm}$ from the human tissue; (b) SIW cavity-backed patch antenna placed at distance $D = 10 \text{ mm}$ from the human tissue without SRR superstrate.

6.3 Experimental

The antenna and metamaterial prototypes have been fabricated by employing the dielectric substrates Rogers duroid RT/5880 with $\epsilon_r = 2.2$ and $\tan \delta = 0.0009$ and Rogers RO4350B with $\epsilon_r = 3.48$ and $\tan \delta = 0.004$, respectively, and by using a standard PCB process.

Top-views of the SIW cavity-backed antenna and the metamaterial lens are shown in Fig. 6.8(a), the four holes are fabricated to fixing with suitable screws the metamaterial lens to the SIW antenna and the nuts are screwed in order to obtain the distance $d = 6.9 \text{ mm}$, as shown in Fig. 6.8(b). The designed thickness of the metamaterial lens, $t = 3.04 \text{ mm}$, is achieved by overlaying two layers of dielectric substrate each of thickness 1.52 mm . The scattering parameter S_{11} of the device has been measured with the Agilent Technologies N5224A VNA.

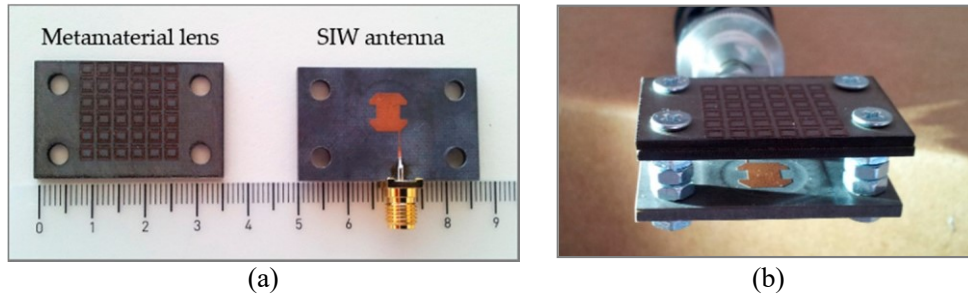


Fig. 6.8. (a) The metamaterial lens (at left) and SIW cavity-backed patch antenna (at right) prototypes. (b) SIW antenna and metamaterial superstrate assembled and connected to the Agilent Technologies N5224A VNA.

In Fig. 6.9, the scattering parameter modulus $|S_{11}|$ of the SIW antenna versus the frequency with metamaterial lens is illustrated, the measurement is performed with the device that irradiates in air (dashed line) and in the biological tissue of a hand (continuous line) placed at a distance close to $D = 10 \text{ mm}$ from the SRR superstrate. The comparison highlights a good impedance matching of the microwave applicator loaded with the biological tissue in the frequency range $10.4 - 11.5 \text{ GHz}$. A minimum of scattering parameter modulus $|S_{11}| = -42 \text{ dB}$ at the $f = 10.6 \text{ GHz}$ has been measured. Moreover, the measured results are in good agreement with simulated one of Fig. 6.6(b), although a shift of the resonance frequency of few hundred of MHz can be observed. In fact, a scattering parameter modulus minimum $|S_{11}| = -36.9 \text{ dB}$ at the $f = 10.9 \text{ GHz}$ has been simulated. The second resonance frequency at $f = 12.7 \text{ GHz}$ of the simulated results is less pronounced respect to the experimental results around at $f = 12.3 \text{ GHz}$. These differences may be due to manufacturing tolerances and the possible air film between the two layers of the dielectric that constitute the metamaterial lens.

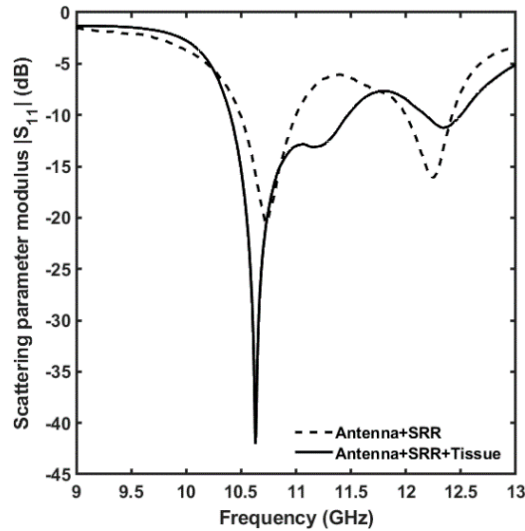


Fig. 6.9. Measured scattering parameter modulus $|S_{11}|$ versus frequency of SIW cavity-backed patch antenna with metamaterial lens, that irradiates in biological tissue (continuous line) and in air (dashed line).

Fig. 6.10 shows the measured scattering parameter modulus $|S_{11}|$ of the SIW cavity-backed patch antenna, with (continuous line) and without (dashed line) the metamaterial superstrate that irradiates in the biological tissue. The electromagnetic field of the antenna without the metamaterial lens is almost completely reflected from human tissue. The measured scattering parameter modulus $|S_{11}|$ in the case of the antenna with SRR metamaterial and tissue (solid curve) exhibits a strong dip close to the frequency $f = 10.7 \text{ GHz}$. At the frequency $f = 11 \text{ GHz}$, the impedance matching is good enough since the measured scattering parameter modulus is close to $|S_{11}| = -14 \text{ dB}$. In fact, Fig. 6.7(a) shows a homogeneous propagation/distribution of the simulated electromagnetic field. Moreover, Fig. 6.10 shows that the measured scattering parameter modulus in the case of antenna and tissue without SRR metamaterial (dashed curve) is close to $|S_{11}| = -4 \text{ dB}$. This implies an impedance mismatch, the presence of the stationary wave and a not homogeneous distribution of the simulated electromagnetic field with nodal regions. It is in perfect agreement with the simulation of Fig. 6.7(b). Therefore, the SRR metamaterial provides an impedance matching and a consequent suppression of the reflected wave.

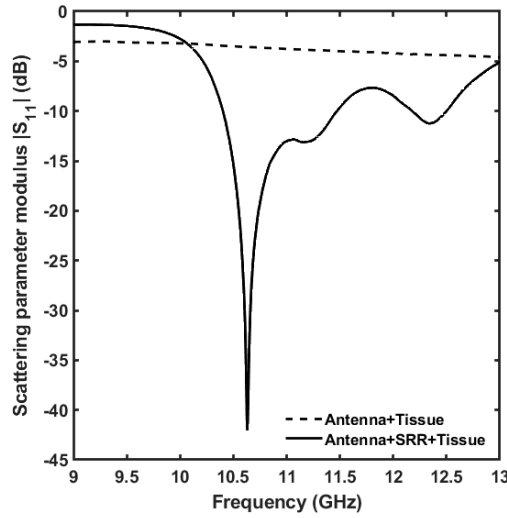


Fig. 6.10. Measured scattering parameter modulus $|S_{11}|$ versus frequency of SIW cavity-backed patch antenna with (continuous line) and without (dashed line) the metamaterial superstrate that irradiates in the biological tissue.

The SIW antenna covered by the metamaterial layer has been characterized with the antenna measurement system in anechoic chamber, StarLab SATIMO, shown in Fig. 6.11. The measured gain of the antenna with and without the metamaterial is illustrated in Fig. 6.12. The SRR superstrate produces an improvement of the gain in the frequency range over $f = 11 \text{ GHz}$ with an increase of $\Delta G = 4 \text{ dB}$ at $f = 12.2 \text{ GHz}$.

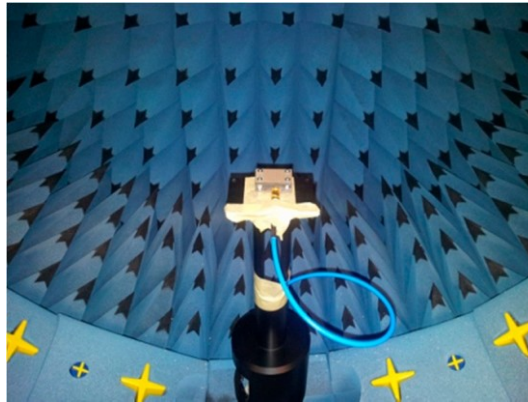


Fig. 6.11. SIW cavity-backed patch antenna with metamaterial lens in the anechoic chamber StarLab SATIMO.

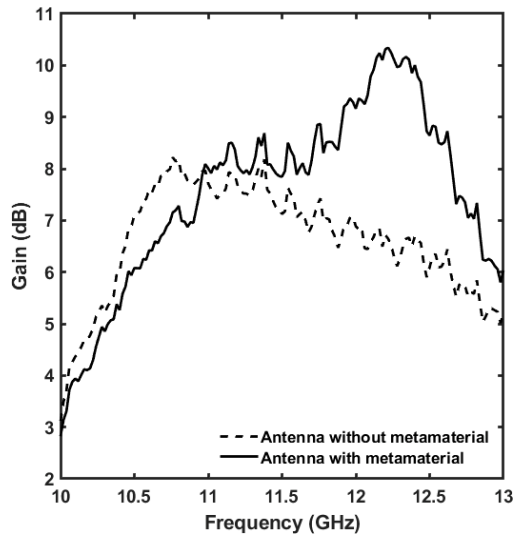


Fig. 6.12. Measured gain versus frequency of SIW cavity-backed patch antenna with and without metamaterial.

6.4 Comparison with literature

A comparison with other microwave applicators is complex, due to the large variety of parameters characterizing the investigations reported in literature, among which the kind of antenna, frequency, kind of metamaterial, applied microwave power and obtained performances characterized in terms of Heating Zone Dimension (HZD), SAR zone, maximum temperature at focusing depth, etc. For the proposed applicator, the peak SAR averaged over the mass $m = 1\text{ g}$ and over the mass $m = 10\text{ g}$, the 50% SAR zone, the $42\text{ }^{\circ}\text{C}$ HZD, for an input power $P = 1\text{ W}$ at $f = 11\text{ GHz}$ frequency are evaluated, in the case of the microwave applicator placed at distance $D = 10\text{ mm}$ from the skin surface of the human tissue. Table 6.III shows that the obtained results are interesting if compared with those from the literature. The reduced HZD zone and high SAR peak evidence the strong focusing obtained via the designed SRR metamaterial. This paves the way for promising novel applications.

TABLE 6.III
COMPARISON WITH OTHER MICROWAVE APPLICATORS FOR CANCER THERAPY

Ref/Year	Antenna/ Frequency	Metamaterial	Biological Tissue	Results
[107] 2009	Line source extended in- finitely/2.45 GHz	Flat left-handed metamaterial (LHM)	Superficial tumor	$T_{max} = 44.7^\circ C$ at 0.71 cm below skin surface 42 °C HZD of 1 cm × 1.2 cm Electromagnetic field source 43.44 Vcm ⁻¹
[108] 2011	Dipole an- tenna/ 4.15 GHz	Flat left-handed metamaterial (LHM)	Breast tissue	$T_{max} = 44.7^\circ C$ at 7.5 cm from the border of the LHM lens Input power $P = 8 W$
[109] 2012	Multiple Line source extended in- finitely/ 2.45GHz	Flat left-handed metamaterial (LHM)	Superficial tumor	42 °C HZD of 6.2 cm × 1.3 cm
[110] 2014	Zero-order resonator an- tenna/ 434 MHz	Zero-order reso- nator (ZOR) metamaterial	Superficial tumor	50% SAR zone of 6 cm × 24 cm
[111] 2015	Multiple mi- crowave sources/ 6 GHz	Flat left-handed metamaterial (LHM)	Breast tissue	42 °C HZD of 0.87 cm × 0.87 cm × 0.61 cm, four lenses
[112] 2016	Microstrip antenna/ 2.45 GHz	Electromagnetic bandgap (EBG)	Breast tissue	Peak $SAR_{1g} = 25 mW g^{-1}$ Peak $SAR_{10g} =$ 4.54 $mW g^{-1}$ Input power $P = 1 W$
[113] 2017	Coaxial an- tenna/ 2.45 GHz	Flat left-handed metamaterial (LHM)	Superficial tumor	50% SAR zone of 1.81 cm × 0.32 cm
This work	SIW cavity backed patch antenna/ Ku-band	Split ring reso- nator (SSR)	Superficial tumor	Peak $SAR_{1g} =$ 51.1 $mW g^{-1}$ Peak $SAR_{10g} =$ 14.2 $mW g^{-1}$ 50% SAR zone of 1.6 × 0.2 cm 42 °C HZD of 1.4 cm × 1.3 cm × 0.4 cm Input power $P = 1 W$ at $f = 11 GHz$

6.5 Conclusions

A metamaterial lens based on SRR has been designed to be employed as a lens to be put on an SIW cavity-backed patch antenna in order to improve the impedance matching of the antenna when loaded with human tissue and to enhance the focusing of the electromagnetic field into the biological tissue to be treated. A prototype has been fabricated employing the standard, low-cost PCB technology and has been characterized by using a Network Analyzer. The simulated scattering parameter modulus of the antenna loaded with the biological tissue with and without metamaterial lens is $|S_{11}| = -37 \text{ dB}$ and $|S_{11}| = -14 \text{ dB}$ at the $f = 11 \text{ GHz}$ frequency, respectively. The measured minimum of the scattering parameter modulus $|S_{11}| = -42 \text{ dB}$ has been measured at the $f = 10.6 \text{ GHz}$ frequency. The experimental results are in good agreement the simulations. The impedance matching improvement has been proved. The electromagnetic field distributions simulated have highlighted the focusing capability of the metamaterial lens. The antenna measurement in the anechoic chamber has confirmed that this kind of SRR lens can find actual application to focus the electromagnetic field of microwave applicators used in dermatology for the thermal therapy of skin cancer.

7 Design of a Mid-IR laser based on a Ho:Nd-codoped fluorindate fiber

7.1 Introduction

The range of application of the optical sources in the Mid-IR wavelength spectrum includes monitoring of atmosphere contaminants, laser surgery, and high-rate communications.

In this chapter, a novel mid-infrared continuous wave laser, based on a fluorindate fiber co-doped with holmium and neodymium, is designed to emit at $\lambda_s = 3.92 \mu m$, when pumped at $\lambda_p = 808 nm$. The laser is modeled considering a nine-level system, by taking into account experimental spectroscopical parameters. Since the energy transfer coefficients are unknown, they have been evaluated starting from the measured emission spectra of the bulk glass, reported in literature, and comparing their ratio with respect to the ratio between the simulated signal gain coefficients. The designed laser promises higher slope efficiency and power threshold lower than those obtainable with a holmium-heavily-doped fiber, having same fiber section geometry, same refractive indices and pumped at $\lambda_p = 888 nm$. Slope efficiency $\eta = 16.67\%$ and input power threshold $P_{th} = 0.2 W$ are obtained for the fiber length $L_{fiber} = 0.4 m$, dopants concentrations $N_{Ho} = 8 \times 10^{26} ions/m^3$ and $N_{Nd} = 1 \times 10^{26} ions/m^3$, and output mirror reflectivity $R_{out} = 60\%$. This result encourages the fabrication of a continuous wave laser based on a Ho:Nd-codoped fluorindate fiber.

The theoretical model for the laser design is reported in paragraph 2.3.1.

7.2 Energy transfer coefficients recovering

The considered fiber is a step-index double-cladding fluorindate (InF_3) glass fiber, doped with Ho^{3+} and Nd^{3+} ions. Its transverse section is shown in Fig. 7.1. The core diameter is $d_{co} = 16 \mu\text{m}$. The cladding is 2-D shaped, obtained with circular diameter $d_{cl1} = 100 \mu\text{m}$ truncated by two parallel planes at a distance $d = 90 \mu\text{m}$, to enhance cladding pump absorption. The second cladding, made of low index resin, has diameter $d_{cl2} = 155 \mu\text{m}$. The inner and outer numerical apertures are $NA_1 = 0.2$ and $NA_2 = 0.5$, respectively. The optical losses are conservatively considered $\alpha = 0.2 \text{ dB/m}$ for both pump and signal wavelengths, according to the measurement reported in [60]. This kind of double cladding fiber doped with holmium is produced by Le Verre Fluoré [60, 61]. In the following, the co-doping with Ho^{3+} and Nd^{3+} ions is supposed. The pump and signal wavelengths are $\lambda_p = 808 \text{ nm}$ and $\lambda_s = 3920 \text{ nm}$, respectively. The pump wavelength is feasible, since obtainable with commercial pigtailed semiconductor lasers.

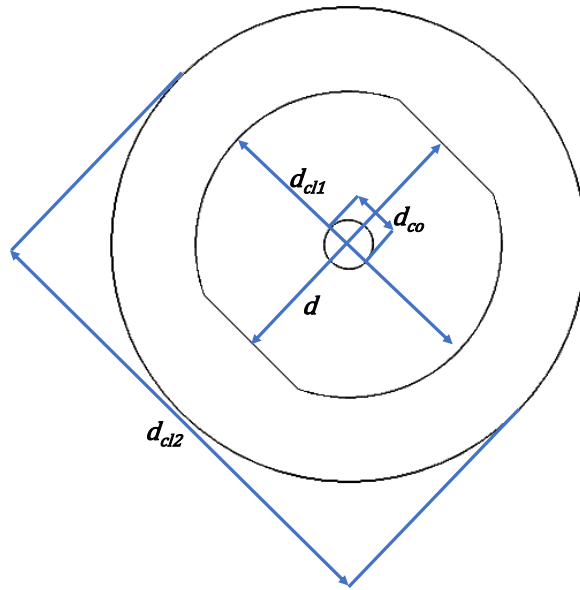


Fig. 7.1. Transverse section of the employed double cladding fiber.

The electromagnetic investigation, performed with a commercial Finite Element Method (FEM) solver, has shown that the fiber is slightly multimode at the normalized frequency number $V = 2.56$ of the signal wavelength. However, the second order mode can be neglected in the laser operation since its overlapping coefficient Γ_s is less than a half of the one of the fundamental mode; its contribution in the laser operation is not considered without significant error, as

confirmed by preliminary simulation performed without any approximation [24].

The spectroscopic parameters used in the simulations are listed in Table 7.I. They are taken from [67,70,76,114-117]. The ion rate equations and the power propagation equations are implemented in a home-made computer code to simulate the optical gain and the laser behavior. Since energy transfer (ET) coefficients K_{ET1} and K_{ET2} are not available from literature, they have been evaluated starting from measured emission spectra from [76] of the bulk glass and comparing their ratio with respect to the gain coefficient ratio simulated for the fiber laser, as reported below. This approach was proposed in a previous work [118]. The aforesaid comparison is feasible in the linear region of the laser characteristic.

TABLE 7.I
SPECTROSCOPIC PARAMETERS OF CO-DOPED Ho:Nd FLUOROINDATE GLASS FIBER

Symbol	Value	Description
$\sigma_{15}(\lambda_p)$	$3.51 \times 10^{-24} \text{ m}^2$ [114]	Absorption cross section Nd: $I_{9/2} \rightarrow F_{5/2}$
$\sigma_{51}(\lambda_p)$	$3.51 \times 10^{-24} \text{ m}^2$ [114]	Emission cross section Nd: $F_{5/2} \rightarrow I_{9/2}$
$\sigma_{98}(\lambda_s)$	$3.4 \times 10^{-25} \text{ m}^2$ [70]	Absorption cross section Ho: $I_6 \rightarrow I_5$
$\sigma_{89}(\lambda_s)$	$3.4 \times 10^{-25} \text{ m}^2$ [70]	Emission cross section Ho: $I_5 \rightarrow I_6$
τ_{R2}	$\approx 0.01 \text{ ms}$ [115]	Nd: $I_{11/2}$ radiative lifetime
τ_{R4}	0.943 ms [114]	Nd: $F_{3/2}$ radiative lifetime
τ_{R5}	0.315 ms [114]	Nd: $F_{5/2}$ radiative lifetime
τ_{R7}	9.09 ms [67]	Ho: I_7 radiative lifetime
τ_{R8}	3.66 ms [76]	Ho: I_6 radiative lifetime
τ_{R9}	0.29 ms [76]	Ho: I_5 radiative lifetime
β_{21}	100% [114]	Nd: $I_{11/2} \rightarrow I_{9/2}$ branching ratio
β_{41}	63.7% [114]	Nd: $F_{3/2} \rightarrow I_{9/2}$ branching ratio
β_{42}	36.3% [114]	Nd: $F_{3/2} \rightarrow I_{11/2}$ branching ratio
β_{43}	$\approx 0\%$ [114]	Nd: $F_{3/2} \rightarrow I_{15/2}$ branching ratio
β_{51}	62.6% [114]	Nd: $F_{5/2} \rightarrow I_{9/2}$ branching ratio
β_{52}	37.4% [114]	Nd: $F_{5/2} \rightarrow I_{11/2}$ branching ratio
β_{53}	$\approx 0\%$ [114]	Nd: $F_{5/2} \rightarrow I_{15/2}$ branching ratio
β_{54}	$\approx 0\%$ [114]	Nd: $F_{5/2} \rightarrow F_{3/2}$ branching ratio
β_{76}	100% [70]	Ho: $I_7 \rightarrow I_8$ branching ratio
β_{86}	94.0% [70]	Ho: $I_6 \rightarrow I_8$ branching ratio
β_{87}	6.00% [70]	Ho: $I_6 \rightarrow I_7$ branching ratio
β_{96}	55.7% [70]	Ho: $I_5 \rightarrow I_8$ branching ratio
β_{97}	43.0% [70]	Ho: $I_5 \rightarrow I_7$ branching ratio
β_{98}	1.30% [70]	Ho: $I_5 \rightarrow I_6$ branching ratio
W_{NR}	$\approx 10^8 \text{ s}^{-1}$ [116][117]	Non-radiative rates Nd: $F_{5/2} \rightarrow F_{3/2}$ and Nd: $F_{15/2} \rightarrow F_{11/2}$

Fig. 7.2 shows the measured emission spectra intensities $s_{sn}(\lambda)$ for different Ho^{3+} concentrations [76], normalized with respect to $s_{s1}(\lambda)$ for a better reading; the Nd^{3+} concentration is set to $N_{Nd} = 2 \times 10^{26} \text{ ions/m}^3$ (1 mol.%). In particular, $s_{s1}(\lambda)$ is the normalized emission spectrum intensity for $N_{Ho} = 2 \times 10^{26} \text{ ions/m}^3$ (1 mol.%) (blue curve), $s_{s2}(\lambda)$ for $N_{Ho} = 1 \times 10^{26} \text{ ions/m}^3$ (0.5 mol.%) (red curve), and $s_{s3}(\lambda)$ for $N_{Ho} = 4 \times 10^{25} \text{ ions/m}^3$ (0.2 mol.%) (yellow curve). The ratios R_n between measured emission spectra at $\lambda_s = 3920 \text{ nm}$ are defined as in Table 7.II. The signal gains coefficients $g_{s1}(\lambda_s)$, $g_{s2}(\lambda_s)$, and $g_{s3}(\lambda_s)$ refer to $N_{Ho} = 2 \times 10^{26} \text{ ions/m}^3$ (1 mol.%), $N_{Ho} = 1 \times 10^{26} \text{ ions/m}^3$ (0.5 mol.%), and $N_{Ho} = 4 \times 10^{25} \text{ ions/m}^3$ (0.2 mol.%), respectively. The ratios RG_n are defined as follows $RG_1 = g_{s1}(\lambda_s)/g_{s3}(\lambda_s)$; $RG_2 = g_{s1}(\lambda_s)/g_{s2}(\lambda_s)$; $RG_3 = g_{s2}(\lambda_s)/g_{s3}(\lambda_s)$.

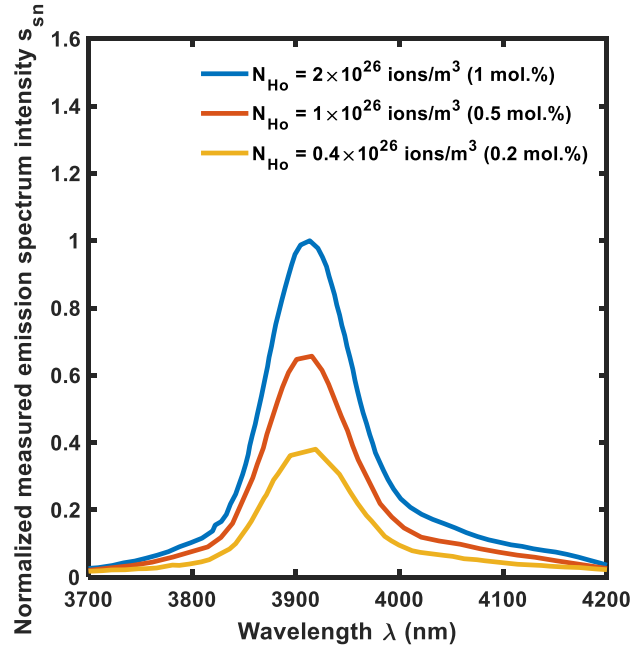


Fig. 7.2. Normalized measured emission spectra intensities s_{sn} as a function of the wavelength λ , for different Ho^{3+} concentrations; Nd^{3+} concentration is set to $N_{Nd} = 2 \times 10^{26} \text{ ions/m}^3$ (1 mol.%) [76].

TABLE 7.II
EMISSION SPECTRA RATIOS

Symbol	Expression	Description
R_1	$s_{s1}(\lambda_s)/s_{s3}(\lambda_s)$	Ratio between the normalized emission spectra at signal wavelength for $N_{Ho} = 2 \times 10^{26} \text{ ions/m}^3$ and $N_{Ho} = 4 \times 10^{25} \text{ ions/m}^3$
R_2	$s_{s1}(\lambda_s)/s_{s2}(\lambda_s)$	Ratio between the normalized emission spectra at signal wavelength for $N_{Ho} = 2 \times 10^{26} \text{ ions/m}^3$ and $N_{Ho} = 1 \times 10^{26} \text{ ions/m}^3$
R_3	$s_{s2}(\lambda_s)/s_{s3}(\lambda_s)$	Ratio between the normalized emission spectra at signal wavelength for $N_{Ho} = 1 \times 10^{26} \text{ ions/m}^3$ and $N_{Ho} = 4 \times 10^{25} \text{ ions/m}^3$

Fig. 7.3(a), Fig. 7.3(b), and Fig. 7.3(c) show the colormaps of the percentage difference between the ratios $(R_n - RG_n)/R_n$ as a function of the trial energy transfer coefficients K_{ET1} and K_{ET2} .

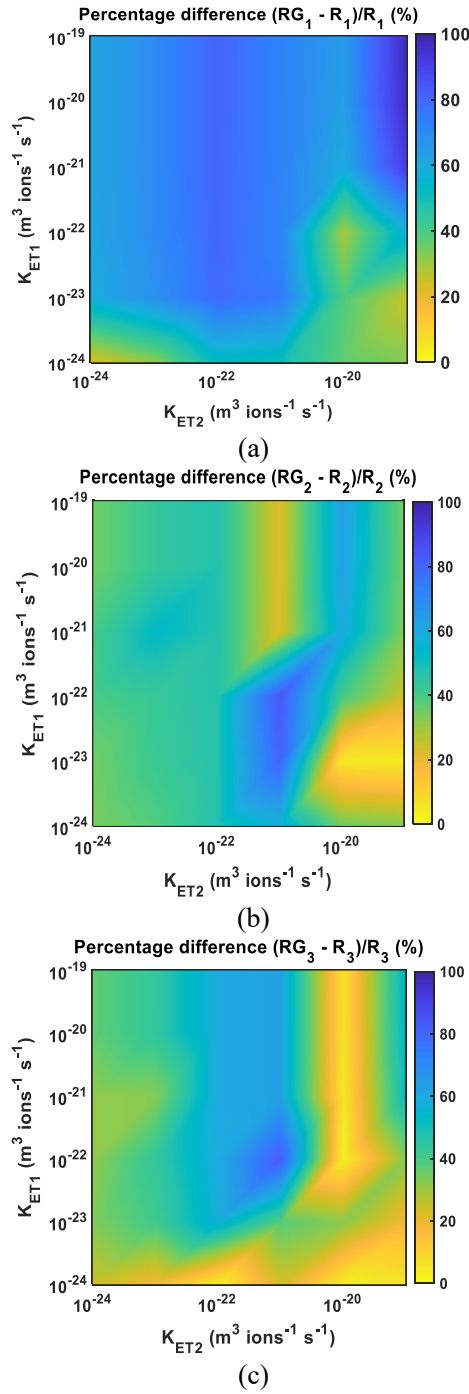


Fig. 7.3. (a) Percentage difference $(RG_1 - R_1)/R_1$, (b) percentage difference $(RG_2 - R_2)/R_2$, and (c) percentage difference $(RG_3 - R_3)/R_3$ as a function of energy transfer coefficients K_{ET1} and K_{ET2} .

These three percentage differences must be contemporarily minimized. This condition is obtained for $K_{ET1} = 4 \times 10^{-22} \text{ m}^3 \text{ ions}^{-1} \text{ s}^{-1}$ and $K_{ET2} = 6 \times 10^{-21} \text{ m}^3 \text{ ions}^{-1} \text{ s}^{-1}$, for which $(R_1 - RG_1)/R_1 = 8 \%$, $(R_2 - RG_2)/$

$R_2 = 1\%$, and $(R_3 - RG_3)/R_3 = 0.7\%$. Table 7.III reports the simulated signal gain coefficient ratios RG_n for the recovered $K_{ET1} = 4 \times 10^{-22} \text{ m}^3 \text{ ions}^{-1} \text{ s}^{-1}$ and $K_{ET2} = 6 \times 10^{-21} \text{ m}^3 \text{ ions}^{-1} \text{ s}^{-1}$ compared to the measured emission spectra ratios R_n . The signal gain coefficient ratios RG_n are obtained considering the same average pump energy of [76], i.e., $P_p = 0.4 \text{ W}$, neodymium concentration $N_{Nd} = 2 \times 10^{26} \text{ ions/m}^3$ (1 mol.%), and holmium concentrations $N_{Ho} = 2 \times 10^{26} \text{ ions/m}^3$ (1 mol.%), $N_{Ho} = 1 \times 10^{26} \text{ ions/m}^3$ (0.5 mol.%), and $N_{Ho} = 0.4 \times 10^{26} \text{ ions/m}^3$ (0.2 mol.%). This allows a proper comparison with R_n .

TABLE 7.III
EMISSION SPECTRA AND SIGNAL GAIN COEFFICIENT RATIOS COMPARISON

Emission spectra ratio R_n	Signal gain coefficient ratio RG_n
$R_1 = 2.63$	$RG_1 = 2.42$
$R_2 = 1.54$	$RG_2 = 1.51$
$R_3 = 1.62$	$RG_3 = 1.61$

To validate these results, the global $Ho:I_5$ level lifetime τ'_{R9} and the global $Ho:I_6$ level lifetime τ'_{R8} have been simulated and compared with the experimental ones taken from literature [76], for different holmium concentrations N_{Ho} . The lifetimes have been simulated solving the rate equations (2.17a)-(2.17j) as a function of time, pumping the system until the ion populations steady-state condition. Then, the pump power is turned off, setting $P_p = 0 \text{ W}$, and the simulated population exponential decays are observed. The level lifetimes are calculated as the time constants of the obtained exponential curves.

Fig. 7.4 shows the $Ho:I_5$ level lifetime τ'_{R9} and the $Ho:I_6$ level lifetime τ'_{R8} simulated (blue) and measured (red) [76] as a function of the holmium concentration N_{Ho} . The good accordance confirms that the recovered energy transfer coefficients K_{ET1} and K_{ET2} are correct.

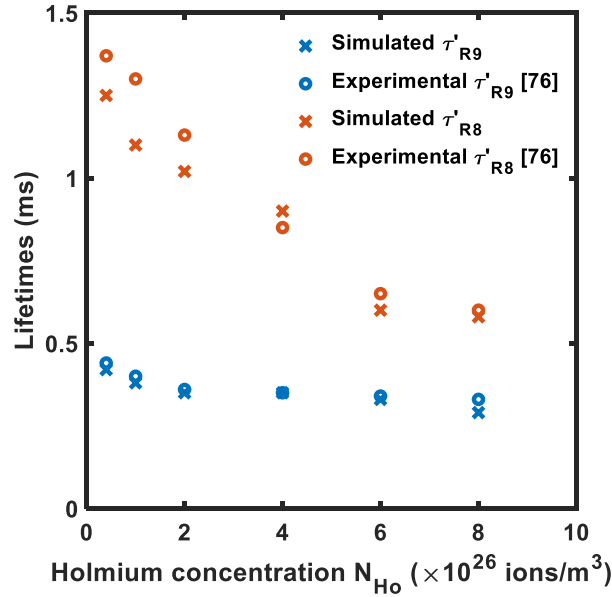


Fig. 7.4. $Ho:I_5$ level lifetime τ'_{R9} and the $Ho:I_6$ level lifetime τ'_{R8} as a function of the holmium concentration N_{Ho} , comparing simulated (blue) and measured [76] (red) values; $N_{Nd} = 2 \times 10^{26}$ ions/m³ (1 mol.%).

7.3 Laser design

In the design, a deep investigation of the laser output signal power P_s versus: i) the laser fiber length L_{fiber} ; ii) the dopants concentration N_{Nd} and N_{Ho} ; iii) the output mirror reflectivity R_2 is carried out, in order to identify the configuration allowing the maximum slope efficiency η and the minimum threshold power P_{th} .

Fig. 7.5 shows the output power P_s as a function of the input pump power P_p , for different values of the fiber length L_{fiber} . The characteristics show a discontinuity with a sawtooth shape in all cases. The reason behind this behavior will be deeply investigated in section V. The discontinuity shifts towards higher pump power as the fiber length L_{fiber} increases. Moreover, the slope efficiency η slightly decreases, while the input pump threshold is close to $P_{th} = 0.5$ W in all cases. It is worthy to observe that experiments in literature suggest avoiding input power larger than $P_p = 6$ W in typical fluoroindate fibers [61]. In a lightly doped fiber higher pumping levels could be potentially employed. Therefore, a different cavity optimization could be required. A good trade-off length is $L_{fiber} = 0.4$ m, for which the discontinuity occurs beyond the realis-

tic range of power, i.e., for $P_p = 8\text{ W}$, and for which the efficiency $\eta = 8.47\%$ is obtained. The slope efficiency is calculated after the threshold, between $P_p = 1\text{ W}$ and $P_p = 1.5\text{ W}$.

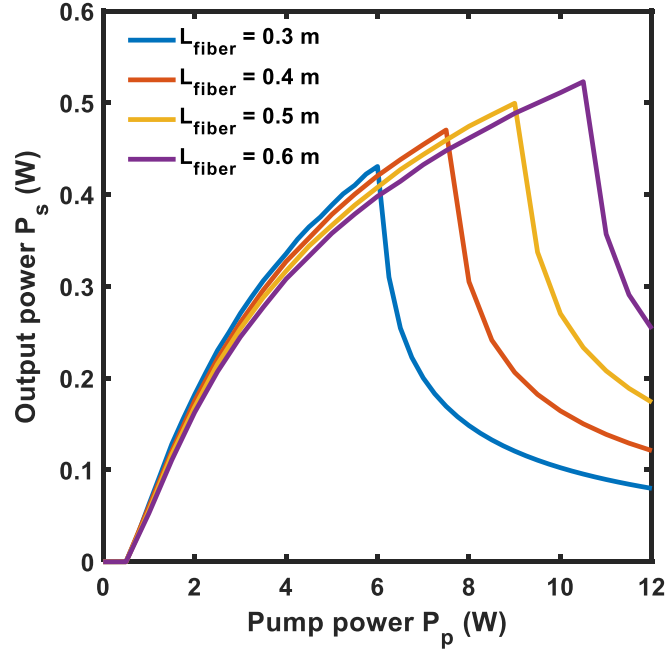


Fig. 7.5. Output power P_s as a function of the input pump power P_p , for different values of the fiber length L_{fiber} . Holmium concentration $N_{Ho} = 2 \times 10^{26}\text{ ions}/m^3$ (1 mol.%), neodymium concentration $N_{Nd} = 2 \times 10^{26}\text{ ions}/m^3$ (1 mol.%), input mirror reflectivity $R_{in} = 99\%$, output mirror reflectivity $R_{out} = 70\%$.

Fig. 7.6 shows the output power P_s as a function of the input pump power P_p , for different values of the holmium concentration N_{Ho} . As the concentration increases, the slope efficiency η also increases and the discontinuity shifts to higher input pump powers. The input pump threshold decreases to $P_{th} = 0.1\text{ W}$. The optimal holmium concentration is the maximum considered in the simulations $N_{Ho} = 8 \times 10^{26}\text{ ions}/m^3$ (4 mol.%) (purple curve). Generally, higher holmium concentrations are not used in practice to avoid second order phenomena, such as cross-relaxation or up-conversion.

Fig. 7.7 shows the output power P_s as a function of the input pump power P_p , for different values of neodymium concentration N_{Nd} . As the concentration increases, the slope efficiency η slightly increases until $N_{Nd} = 1 \times 10^{26}\text{ ions}/m^3$ (0.5 mol.%) (yellow curve), while the input pump threshold P_{th} always decreases. The value $N_{Nd} = 1 \times 10^{26}\text{ ions}/m^3$ (0.5 mol.%) can be considered as optimized, allowing the highest efficiency and a good input pump threshold $P_{th} = 0.15\text{ W}$.

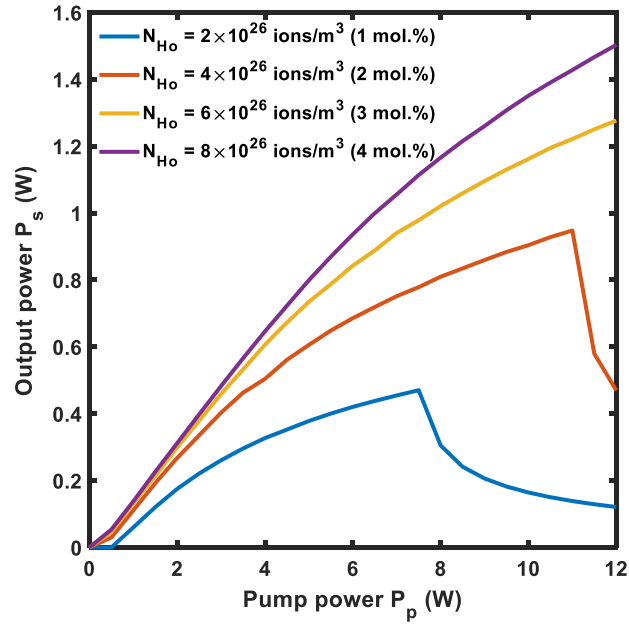


Fig. 7.6. Output power P_s as a function of the input pump power P_p , for different values of the holmium concentration N_{Ho} . Fiber length $L_{fiber} = 0.4$ m, neodymium concentration $N_{Nd} = 2 \times 10^{26}$ ions/m³ (1 mol.%), input mirror reflectivity $R_{in} = 99\%$, output mirror reflectivity $R_{out} = 70\%$.

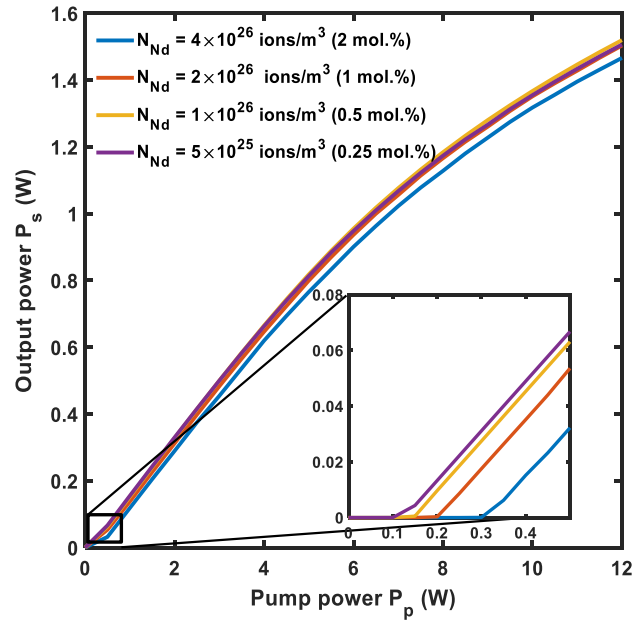


Fig. 7.7. Output power P_s as a function of the input pump power P_p , for different values of the neodymium concentration N_{Nd} . Fiber length $L_{fiber} = 0.4$ m, holmium concentration $N_{Ho} = 8 \times 10^{26}$ ions/m³ (4 mol.%), input mirror reflectivity $R_{in} = 99\%$, output mirror reflectivity $R_{out} = 70\%$.

Fig. 7.8 shows the output power P_s as a function of the input pump power P_p , for different values of output mirror reflectivity R_{out} . The slope efficiency η increases as the output mirror reflectivity R_{out} decreases until $R_{out} = 60\%$, while the input pump threshold P_{th} decreases from $P_{th} = 0.3\text{ W}$ to $P_{th} = 0.05\text{ W}$.

The optimal laser configuration is obtained for fiber length $L_{fiber} = 0.4\text{ m}$, holmium concentration $N_{Ho} = 8 \times 10^{26}\text{ ions/m}^3$, neodymium concentration $N_{Nd} = 1 \times 10^{26}\text{ ions/m}^3$, and output mirror reflectivity $R_{out} = 60\%$, allowing the slope efficiency $\eta = 16.67\%$ and the input pump threshold $P_{th} = 0.2\text{ W}$. These simulated performances are better than those typical of CW lasers obtained with heavily-holmium-doped fiber with the same geometry, pumped at $\lambda_p = 888\text{ nm}$, showing $\eta = 10.2\%$ and input pump threshold $P_{th} = 4.3\text{ W}$ [61].

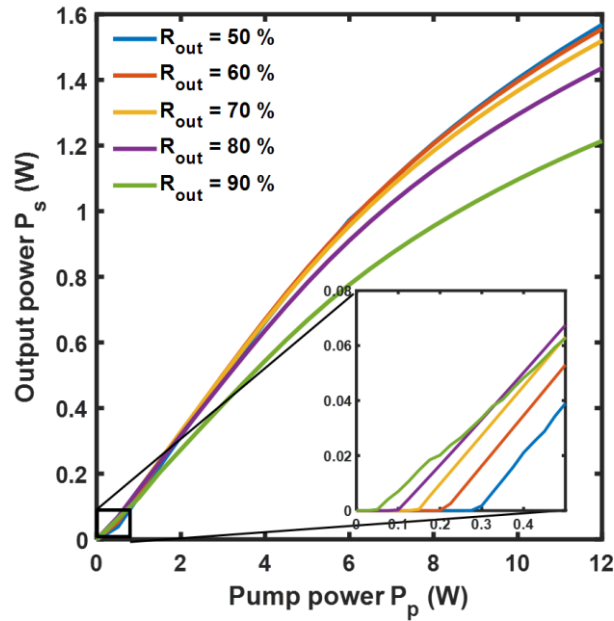


Fig. 7.8. Output power P_s as a function of the input pump power P_p , for different values of the output mirror reflectivity R_{out} . Fiber length $L_{fiber} = 0.4\text{ m}$, holmium concentration $N_{Ho} = 8 \times 10^{26}\text{ ions/m}^3$ (4 mol.%), neodymium concentration $N_{Nd} = 1 \times 10^{26}\text{ ions/m}^3$ (0.5 mol.%), input mirror reflectivity $R_{in} = 99\%$.

7.4 Results discussion

By the inspection of the energy level diagram of Fig. 2.4, for each ion couple involved in the ET2 transition an energy loss equal to the energy difference $\Delta E = 1.7 \times 10^3\text{ cm}^{-1}$ [76] between level 8 and level 3 occurs, due to the 1-3

and 8-6 transitions. This energy leakage could be the cause of the sawtooth. Indeed, simulating the system without ET2 effect, by putting null K_{ET2} , the laser shows the typical characteristic with a pump threshold $P_{th} = 0.6 W$, a slope efficiency $\eta = 0.2\%$, and a saturation power $P_{ss} = 4.3 W$, without any sawtooth.

Fig. 7.9 shows the output power P_s (blue curve) and the output residual pump power P_{res} at the end of the fiber (red curve) as a function of the input pump power P_p . The output residual pump power P_{res} steeply increases when the output signal P_s shows the discontinuity, close to $P_p = 7.5 W$. For larger values of the input pump power P_p , a large amount is not absorbed, reaching about the 50 % for $P_p = 12 W$. This is plausibly caused by a too large depopulation of level 1 ($Nd: I_{9/2}$), reducing ET2 effect. By simulation, the N_1 ion population at the end of the fiber steeply decreases for pump power higher than $P_p = 7.5 W$. Therefore, few ions can be promoted from level 1 to level 3 ($Nd: I_{15/2}$) and the related transition 8-6 does not occur efficiently. Accordingly with this phenomenon, for pump power larger than $P_p = 7.5 W$, the N_8 ion population steeply increases affecting the laser population inversion. This could be a further cause of the sawtooth.

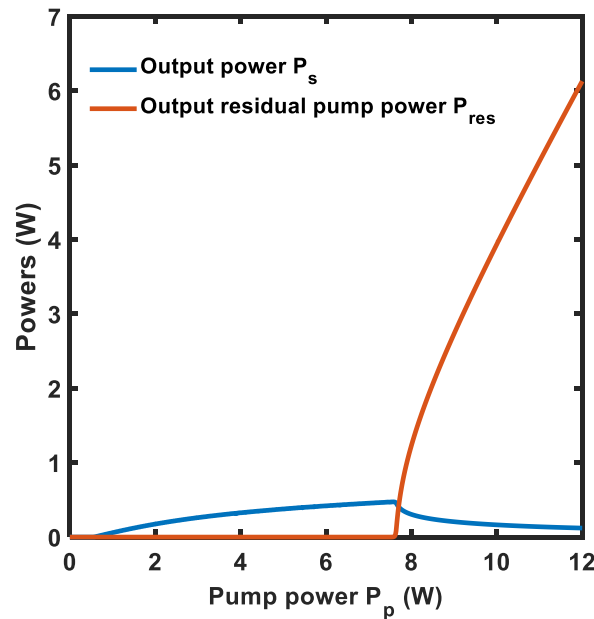


Fig. 7.9. Output power P_s (blue curve) and output residual pump power P_{res} (red curve) as a function of the input pump power P_p . Fiber length $L_{fiber} = 0.4 m$, holmium concentration $N_{Ho} = 2 \times 10^{26} ions/m^3$ (1 mol.%), neodymium concentration $N_{Nd} = 2 \times 10^{26} ions/m^3$ (1 mol.%), input mirror reflectivity $R_{in} = 99\%$, output mirror reflectivity $R_{out} = 70\%$.

7.5 Conclusions

For the first time, a CW laser emitting at $\lambda_s = 3.92 \mu m$ based on a holmium and neodymium co-doped fluoroindate glass fiber is accurately designed, by using measured and recovered spectroscopic parameters. By employing an input pump power at the wavelength $\lambda_p = 808 nm$, a fiber length $L_{fiber} = 0.4 m$, an holmium concentration $N_{Ho} = 8 \times 10^{26} ions/m^3$ (4 mol.%), a neodymium concentration $N_{Nd} = 1 \times 10^{26} ions/m^3$ (0.5 mol.%), and an output mirror reflectivity $R_{out} = 60 \%$, a slope efficiency $\eta = 16.67 \%$ and an input pump threshold $P_{th} = 0.2 W$ can be obtained. This result is interesting if compared with the efficiency obtainable with holmium doped fiber.

8 Design of a gain-switching pulsed laser based on a Ho^{3+} -doped fluorindate fiber

8.1 Introduction

In this chapter, a gain-switched pulsed laser based on a commercial, heavily holmium-doped fluorindate glass fiber, is designed to emit in the middle-infrared range, at the wavelength $\lambda = 3.92 \mu\text{m}$. The laser, pumped at $\lambda = 888 \text{ nm}$, is modeled by a six-level system, by taking into account experimental spectroscopic parameters, to identify a feasible laser configuration. An output signal peak power of about $P_s^{peak} = 14.62 \text{ W}$ with a full width at half maximum (FWHM) pulse duration less than $\tau_s = 73 \text{ ns}$ and pulse energy $E_s = 1.214 \mu\text{J}$ is predicted, by considering an input peak power of $P_p^{peak} = 10 \text{ W}$, and pump repetition rate of $f = 100 \text{ kHz}$, by employing a 8 cm-long fluorindate fiber with holmium concentration $N_{\text{Ho}} = 100\,000 \text{ ppm}$. The obtained result encourages the construction of a pulsed laser based on a commercially available optical fiber, for applications in different fields as sensing and biomedicine.

8.2 Laser design

The considered fiber is a step-index double-cladding fluorindate (InF_3) glass fiber, doped with 10 mol.% of Ho^{3+} ions, commercially available by Le Verre Fluoré [60]. The core diameter is $d_{co} = 16 \mu\text{m}$ and the numerical aperture is $NA = 0.2$. The cladding is 2-D shaped, obtained with circular diameter $d_{cl1} = 100 \mu\text{m}$ truncated by two parallel plans at a distance $d = 90 \mu\text{m}$, to enhance cladding pump absorption. The second cladding has diameter $d_{cl2} = 155 \mu\text{m}$. Fig. 8.1 illustrates the fiber section geometry and the electric field

modulus of the fundamental HE₁₁ mode simulated via a Finite Element Method (FEM) code.

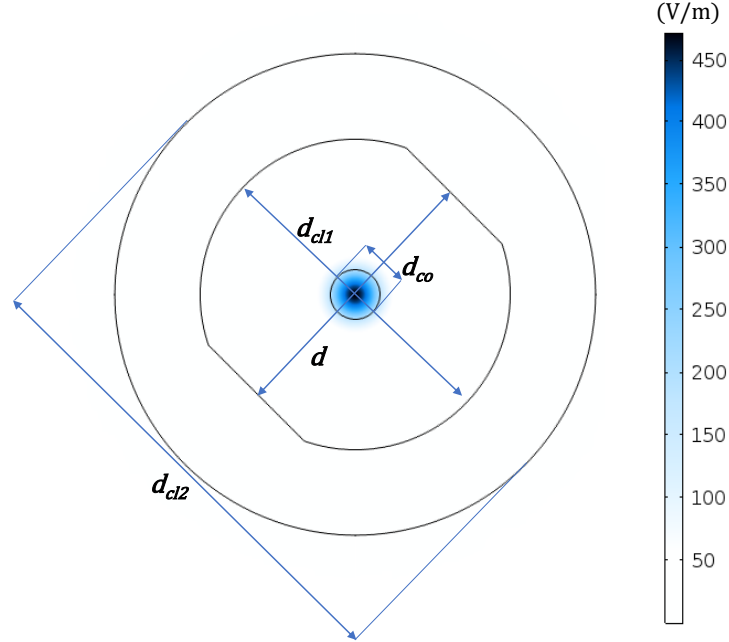


Fig. 8.1. Double-cladding fluorindate fiber section geometry with the electric field modulus (V/m), arbitrarily normalized, of the fundamental HE₁₁ mode.

It is slightly multimode with normalized frequency number $V = 2.56$ at the signal wavelength. It exhibits a second order mode, which can be neglected in the laser operation since its overlapping coefficient with the spatial distribution of ion populations is less than a half of that pertaining to the fundamental mode. This prevents its contribution in the laser operation. The rare earth dopant concentration is $N_{Ho} = 100\ 000\ ppm = 2 \times 10^{27}\ ions/m^3$. The used spectroscopic and optical parameters are taken from [67, 71] and listed in Table 8.I. Since ETU rate K , cross relaxation (CR₁) rate W_{CR1} , and cross relaxation (CR₂) rate W_{CR2} are reported in literature with respect to relative level populations, they were obtained by dividing the values of [67, 71] by the dopant concentration N_{Ho} . The pump and signal wavelengths are $\lambda_p = 888\ nm$ and $\lambda_s = 3920\ nm$, respectively. The equivalent ASE noise bandwidth is $B_{ase} = 100\ nm$, while the optical losses are $\alpha = 0.2\ dB/m$ for both pump and signal wavelengths as reported in [72]. The simulations are performed via the differential equations by using Finite-Difference Time-Domain (FDTD) method, by considering a time grid with step $\Delta t = 0.1\ ns$ and a space grid with step Δz to obtain twenty space samples along the fiber. The pump excitation wave-

form is considered as a square wave with amplitude P_p^{peak} , repetition rate f , and duty cycle D .

8.2.1 Model validation

The six-level model is validated by considering the experimental data reported in literature [61]. In particular, Fig. 8.2 shows the comparison between the six-level model and of the five-level model simulated efficiencies, with respect to the measured values, for a CW input pump, i.e., for a duty cycle $D = 100\%$, fiber length $L_{fiber} = 23\text{ cm}$, and second mirror reflectivity $R_2 = 84\%$ [61]. A slope efficiency $\eta_{CW} = 8.9\%$ and power threshold $P_{th} = 4.2\text{ W}$ are simulated with the six-level model.

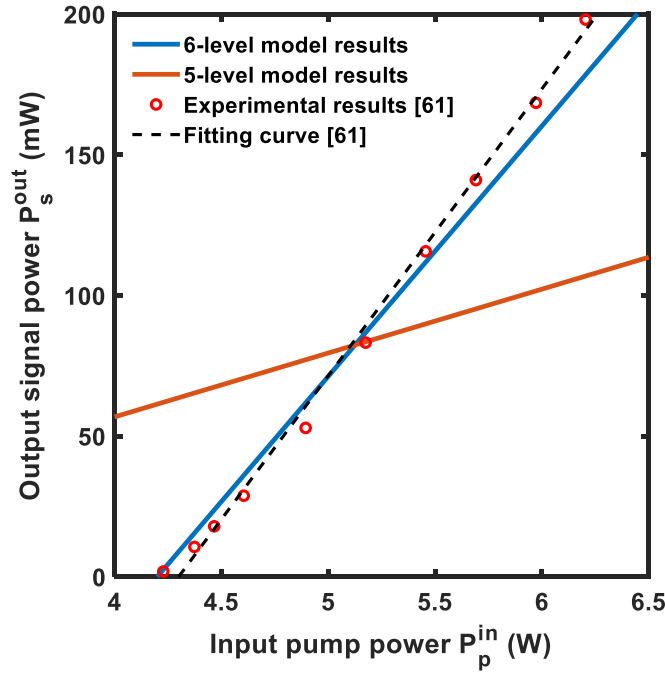


Fig. 8.2. Output signal power P_s^{out} as a function of the input pump power P_p^{in} , for the six-level model (blue line), five-level model (orange line), experimental results (red circles) [61], and the fitting linear line for the experimental results (black dashed line) [61].

These values are in good agreement with the experimental ones $\eta_{CW} = 10.2\%$ and $P_{th} = 4.3\text{ W}$. The five-level model provides less accurate simulation results, the slope efficiency being $\eta_{CW} = 2.27\%$ and the power threshold $P_{th} = 1.5\text{ W}$ with a significant deviation with respect to the experimental values. The discrepancy between the experimental values and the six-level model simulated parameters could be due to i) the employed attenuation $\alpha = 0.2\text{ dB/m}$ for both

pump and signal wavelengths, which is probably overestimated and ii) the employed emission and absorption cross-section approximated as coincident at the two considered wavelengths, listed in Table 8.I. However, in absence of further experimental spectroscopic data, this choice is precautionary for the laser feasibility investigation.

8.2.2 Pulsed laser results

As an example of the pulsed laser simulation, Fig. 8.3 shows the unregular output signal pulses $P_s^{out}(t)$ (red curve) at the end of the fiber length L_{fiber} and the input pump pulses $P_p^{in}(t)$ (black curve), with peak power $P_p^{peak} = 10 W$, as a function of time t ; pump repetition rate $f = 100 kHz$, input pump duty cycle $D = 50 \%$, fiber length $L_{fiber} = 10 cm$, and second mirror reflectivity $R_2 = 70 \%$. In the simulation, the considered input pump laser is the effectively coupled in the fiber. The laser of Fig. 8.3 is not optimized. The emission exhibits multiple output peaks with unstable amplitudes.

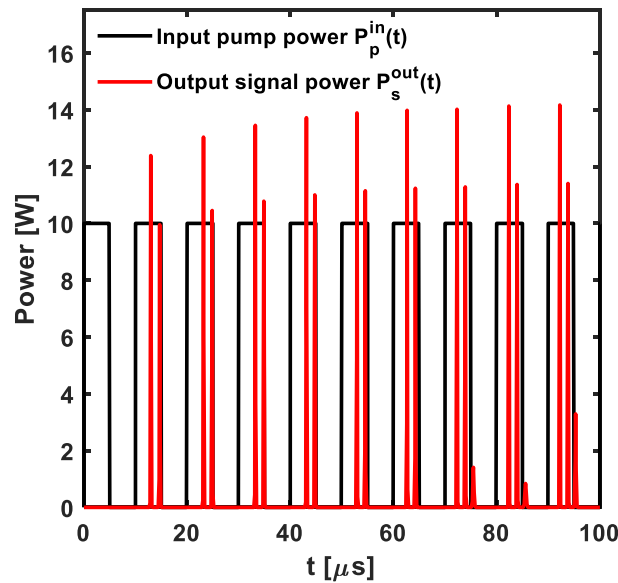


Fig. 8.3. Output signal pulses (red curve) and input pump pulses (black curve), with peak power $P_p^{peak} = 10 W$, as a function of time. Pump repetition rate $f = 100 kHz$, input pump duty cycle $D = 50 \%$, fiber length $L_{fiber} = 10 cm$, second mirror reflectivity $R_2 = 70 \%$.

TABLE 8.I
SPECTROSCOPIC PARAMETERS OF FLUOROINDATE GLASS FIBER [67,71]

Symbol	Value	Description
$\sigma_{14}(\lambda_p)$	$4.3 \times 10^{-26} m^2$	Absorption cross section $I_8 \rightarrow I_5$
$\sigma_{41}(\lambda_p)$	$4.3 \times 10^{-26} m^2$	Emission cross section $I_5 \rightarrow I_8$
$\sigma_{36}(\lambda_p)$	$7.1 \times 10^{-25} m^2$	Absorption cross section $I_6 \rightarrow S_2$
$\sigma_{63}(\lambda_p)$	$7.1 \times 10^{-25} m^2$	Emission cross section $S_2 \rightarrow I_6$
$\sigma_{34}(\lambda_s)$	$3.4 \times 10^{-25} m^2$	Absorption cross section $I_6 \rightarrow I_5$
$\sigma_{43}(\lambda_s)$	$3.4 \times 10^{-25} m^2$	Emission cross section $I_5 \rightarrow I_6$
τ_{R2}	16.2 ms	I_7 radiative lifetime
τ_{R3}	6.2 ms	I_6 radiative lifetime
τ_{R4}	135 μ s	I_5 radiative lifetime
τ_{R5}	16.3 μ s	F_5 radiative lifetime
τ_{R6}	312 μ s	S_2 radiative lifetime
β_{21}	1	$I_7 \rightarrow I_8$ branching ratio
β_{31}	0.942	$I_6 \rightarrow I_8$ branching ratio
β_{32}	0.058	$I_6 \rightarrow I_7$ branching ratio
β_{41}	0.557	$I_5 \rightarrow I_8$ branching ratio
β_{42}	0.430	$I_5 \rightarrow I_7$ branching ratio
β_{43}	0.013	$I_5 \rightarrow I_6$ branching ratio
β_{51}	0.758	$F_5 \rightarrow I_8$ branching ratio
β_{52}	0.192	$F_5 \rightarrow I_7$ branching ratio
β_{53}	0.046	$F_5 \rightarrow I_6$ branching ratio
β_{54}	0.004	$F_5 \rightarrow I_5$ branching ratio
β_{61}	0.500	$S_2 \rightarrow I_8$ branching ratio
β_{62}	0.400	$S_2 \rightarrow I_7$ branching ratio
β_{63}	0.100	$S_2 \rightarrow I_6$ branching ratio
β_{64}	≈ 0	$S_2 \rightarrow I_5$ branching ratio
β_{65}	≈ 0	$S_2 \rightarrow F_5$ branching ratio
K	$2.11 \times 10^{-24} m^3/s$	Energy transfer upconversion (ETU) rate
W_{CR1}	$3.48 \times 10^{-23} m^3/s$	Cross relaxation (CR1) rate
W_{CR2}	$1.5 \times 10^{-22} m^3/s$	Cross relaxation (CR2) rate

A deep investigation about the dependence of the laser output signal peak power P_s^{peak} , output signal pulse width τ_s , and energy E_s , on the laser fiber length L_{fiber} for different pairs of input pump duty cycle D and second mirror reflectivity R_2 , (see Figs. 8.4 – 8.6) is carried out. Since variations of the input pump duty cycle D and of the second mirror reflectivity R_2 are strictly related,

they have been investigated simultaneously. After a high number of simulations, only the cases of practical interest, with stable single pulse operation, are reported. For all investigated cases, the output residual pump peak power was under the 1% of the input pump peak power.

Fig. 8.4 shows the output signal peak power P_s^{peak} as a function of the laser fiber length L_{fiber} , for different pairs of input pump duty cycle D and second mirror reflectivity R_2 ; pump repetition rate $f = 100 \text{ kHz}$. As the input pump duty cycle D increases, the second mirror reflectivity R_2 must be reduced to guarantee single pulse output. This induces a strong decrease of the output signal peak power P_s^{peak} . The maximum output signal peak power $P_s^{peak} = 14.76 \text{ W}$ is obtained for the fiber length $L_{fiber} = 6 \text{ cm}$, with input pump duty cycle $D = 25\%$ and second mirror reflectivity $R_2 = 85\%$.

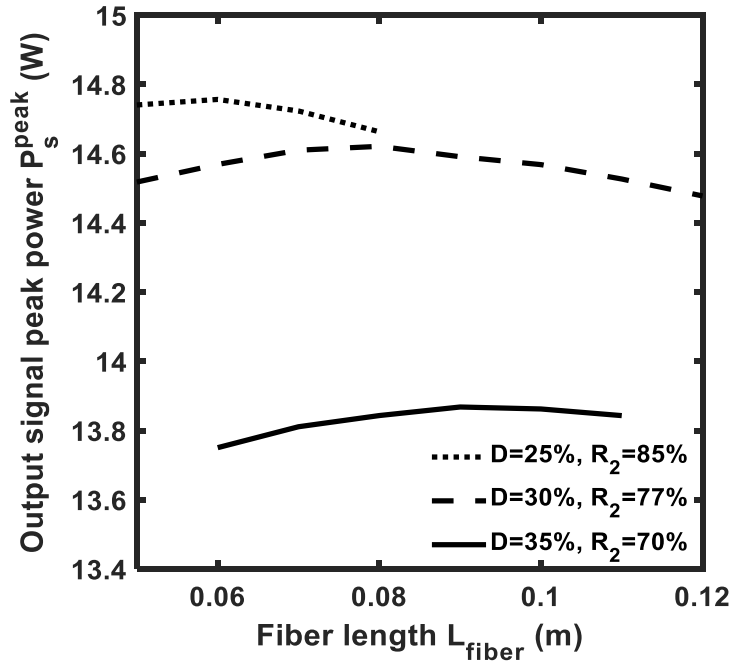


Fig. 8.4. Output signal peak power P_s^{peak} as a function of the laser fiber length L_{fiber} , for different pairs of input pump duty cycle D and second mirror reflectivity R_2 . Pump repetition rate $f = 100 \text{ kHz}$.

Fig. 8.5 shows the output signal pulse full width at half maximum (FWHM) width τ_s as a function of the laser fiber length L_{fiber} , for different pairs of input pump duty cycle D and second mirror reflectivity R_2 ; pump repetition rate $f = 100 \text{ kHz}$. The output pulse width τ_s increases almost linearly with the fiber length L_{fiber} . It is weakly dependent on the input pump duty cycle D and the second mirror reflectivity R_2 . To shorten the output optical pulse duration,

reduced fiber lengths L_{fiber} are more suitable. The shortest output pulse width $\tau_s = 58.9 \text{ ns}$ is obtained for input pump duty cycle $D = 25\%$, second mirror reflectivity $R_2 = 85\%$, and fiber length $L_{fiber} = 5 \text{ cm}$. This small length value is feasible thank to the very high dopant concentration.

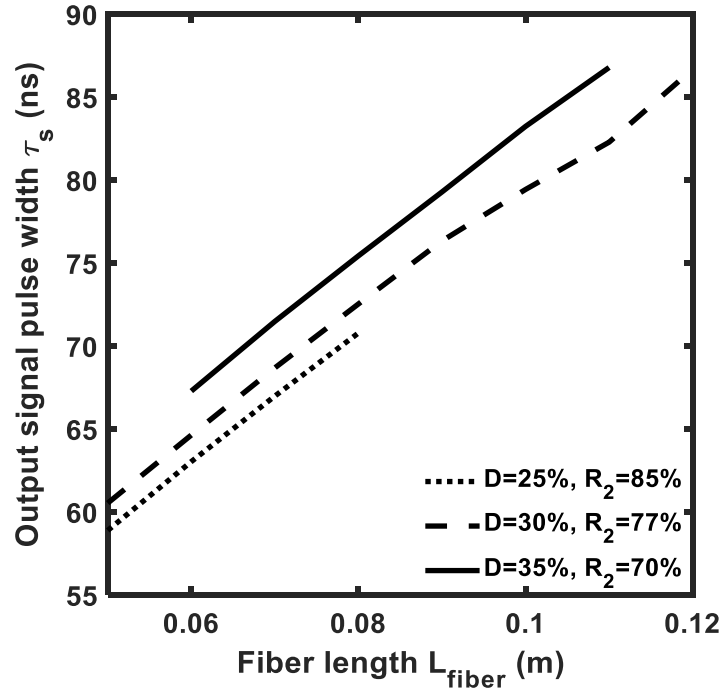


Fig. 8.5. Output signal pulse width τ_s as a function of the laser fiber length L_{fiber} , for different pairs of input pump duty cycle D and second mirror reflectivity R_2 . Pump repetition rate $f = 100 \text{ kHz}$.

Fig. 8.6 shows the output signal pulse energy E_s as a function of the laser fiber length L_{fiber} , for different pairs of input pump duty cycle D and second mirror R_2 ; pump repetition rate $f = 100 \text{ kHz}$. It grows almost linearly with the fiber length L_{fiber} and it is quite independent from the input pump duty cycle D and the second mirror reflectivity R_2 . The maximum output signal pulse energy $E_s = 1.37 \mu\text{J}$ is obtained for the input pump duty cycle $D = 30\%$, second mirror reflectivity $R_2 = 77\%$, and fiber length $L_{fiber} = 12 \text{ cm}$, leading to an optical-to-optical internal efficiency $\eta = 4.57\%$. The fiber length $L_{fiber} = 5 \text{ cm}$ allows the shortest obtained pulse width τ_s but leads to the minimum output signal pulse energy E_s . To find a tradeoff among the output signal peak power P_s^{peak} as high as possible, the output signal pulse width τ_s as short as possible, and the output signal pulse energy E_s as high as possible, the combination $R_2 = 77\%$ and $L_{fiber} = 8 \text{ cm}$ is chosen for the next investigations.

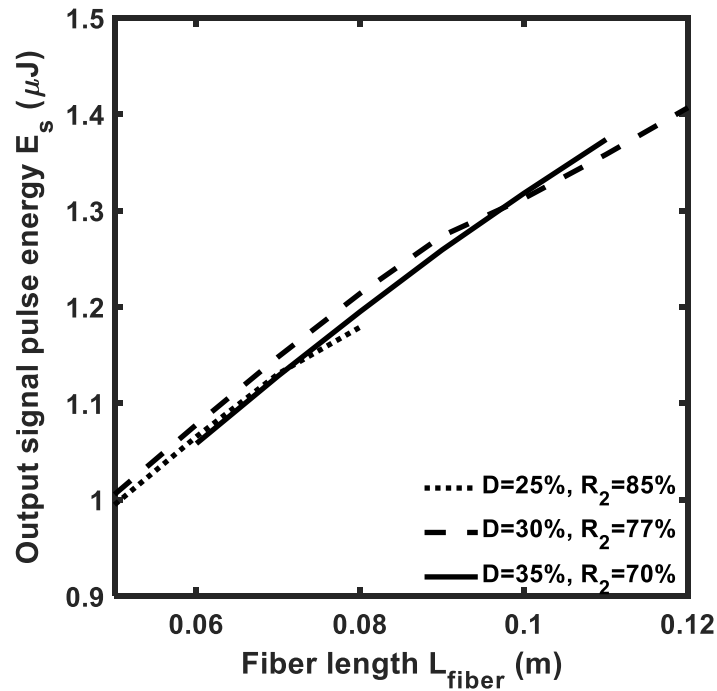


Fig. 8.6. Output signal pulse energy E_s as a function of the laser fiber length L_{fiber} , for different pairs of input pump duty cycle D and second mirror reflectivity R_2 . Pump repetition rate $f = 100$ kHz.

The investigation is completed by considering the dependence of the laser output signal peak power P_s^{peak} , output signal pulse width τ_s , and energy E_s on the input pump duty cycle D , for different values of the pump repetition rate f (see Figs. 8.7 – 8.9).

Fig. 8.7 shows the output signal peak power P_s^{peak} as a function of the input pump duty cycle D , for different values of the pump repetition rate f ; fiber length $L_{fiber} = 8$ cm; second mirror reflectivity $R_2 = 77\%$, input pump peak power $P_p^{peak} = 10$ W. The domains of correct laser operation are very narrow and strongly discontinuous. For each value of f only a small variation of D is allowed in order to obtain a stable single pulse output. Moreover, as the pump repetition rate f increases, also the input pump duty cycle D must increase to obtain the correct pulsed laser operation with stable single pulse output. The output signal peak power P_s^{peak} slightly increases, varying from $P_s^{peak} = 14.5$ W to $P_s^{peak} = 14.87$ W, as f and D increase.

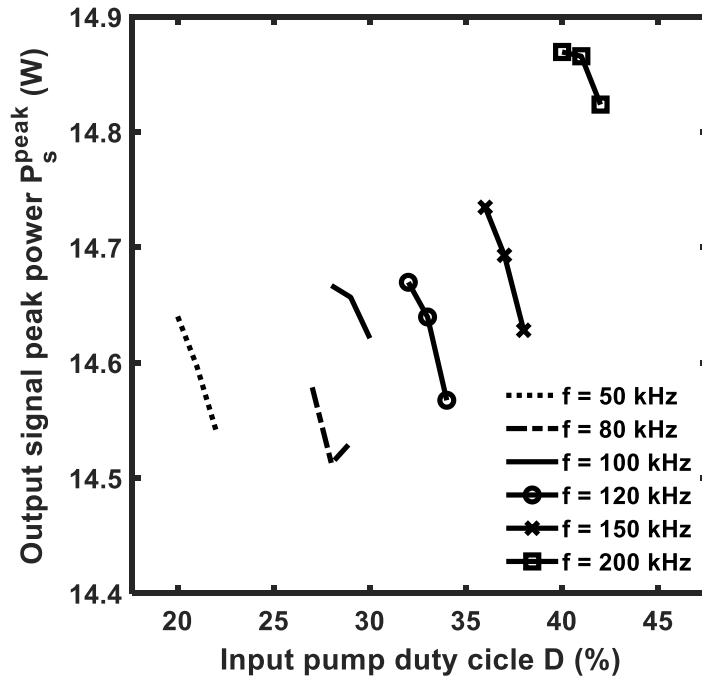


Fig. 8.7. Output signal peak power P_s^{peak} as a function of the input pump duty cycle D , for different values of the pump repetition rate f . Fiber length $L_{fiber} = 8\text{ cm}$, second mirror reflectivity $R_2 = 77\%$.

Fig. 8.8 shows the output signal pulse width τ_s as a function of the input pump duty cycle D , for different values of the pump repetition rate f ; fiber length $L_{fiber} = 8\text{ cm}$, second mirror reflectivity $R_2 = 77\%$. The output signal pulse width τ_s slightly decreases by increasing the pump repetition rate f and the input pump duty D , changing from $\tau_s = 72.75\text{ ns}$ to $\tau_s = 71.9\text{ ns}$.

Fig. 8.9 shows the output signal pulse energy E_s as a function of the input pump duty cycle D , for different values of the pump repetition rate f ; fiber length $L_{fiber} = 8\text{ cm}$, second mirror reflectivity $R_2 = 77\%$. The output signal pulse energy E_s exhibits a small increase as the pump repetition rate f and the input pump duty D increase. It is $E_s = 1.207\text{ }\mu\text{J}$ for $f = 50\text{ kHz}$ and $D = 20\%$ and $E_s = 1.23\text{ }\mu\text{J}$ for $f = 200\text{ kHz}$ and $D = 41\%$. This investigation predicts that good laser performances can be obtained till $f = 200\text{ kHz}$ also by varying the pump repetition rate in the whole investigated range, promising great flexibility of the proposed device.

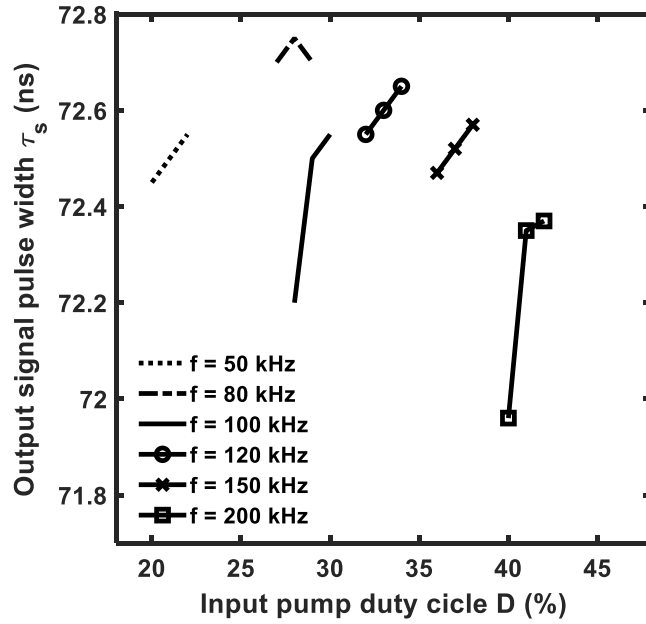


Fig. 8.8. Output signal pulse width τ_s as a function of the input pump duty cycle D , for different values of the pump repetition rate f . Fiber length $L_{fiber} = 8$ cm, second mirror reflectivity $R_2 = 77\%$.

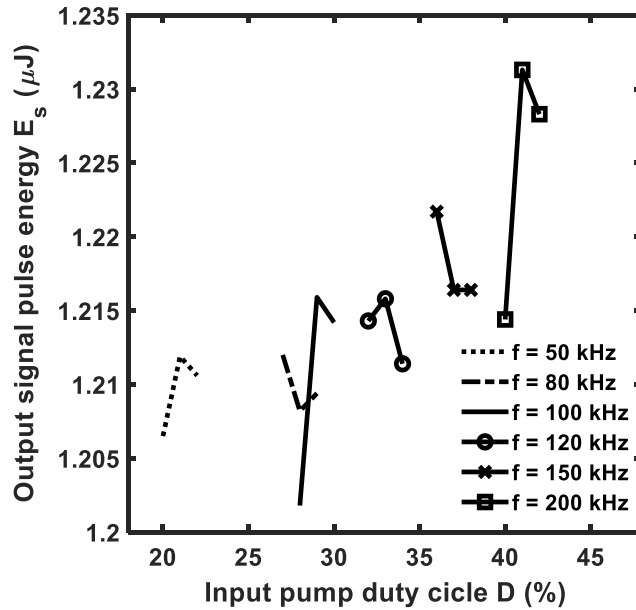
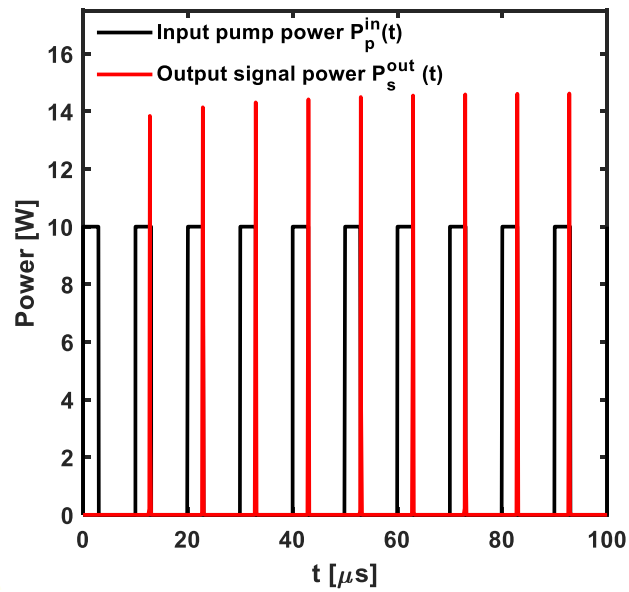


Fig. 8.9. Output signal pulse energy E_s as a function of the input pump duty cycle D , for different values of the pump repetition rate f . Fiber length $L_{fiber} = 8$ cm, second mirror reflectivity $R_2 = 77\%$.

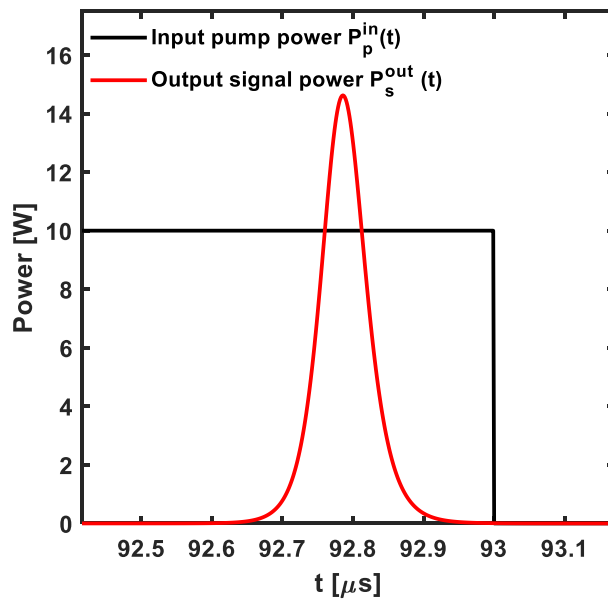
Lastly, the output signal pulses $P_s^{out}(t)$ (red curve) and the input pump pulses $P_p^{in}(t)$ (black curve), with peak power $P_p^{peak} = 10$ W, as a function of

time t , for the optimized cavity is illustrated in Fig. 8.10 for the pump repetition rate $f = 100 \text{ kHz}$, duty cycle $D = 30\%$, fiber length $L_{\text{fiber}} = 8 \text{ cm}$, output mirror reflectivity $R_2 = 77\%$. A stable single pulse signal at $\lambda_s = 3.92 \mu\text{m}$ with an output signal peak power $P_s^{\text{peak}} = 14.62 \text{ W}$, pulse width $\tau_s = 72.55 \text{ ns}$, signal pulse energy $E_s = 1.214 \mu\text{J}$ and optical-to-optical internal efficiency $\eta = 4.05\%$ is obtained. The time to first pulse is $t_{fp} = 15 \mu\text{s}$ and the stable gain-switched regime is achieved after about $t_R = 60 \mu\text{s}$. The obtained efficiency is consistent with the CW laser one [61].

These results pave the way to fabricate a new pulsed laser, based on a commercially available fluorindate fiber, with a stable output in a wide range of repetition pump rates f , from $f = 50 \text{ kHz}$ to beyond 200 kHz . Due to the narrow domains in which the laser exhibits stable single pulse operation, the optimized laser parameters, identified in the proposed design, provide useful guidelines to be followed in order to obtain a feasible pulsed emission. The interest is also due to the potential optimizations which could be obtained by co-doping the fluorindate fiber with Ho³⁺ and Nd³⁺ ions and employing a pumping scheme at $\lambda_p = 808 \text{ nm}$ [76].



(a)



(b)

Fig. 8.10. (a) Output signal pulses (red curve) and the input pump pulses (black curve), with peak power $P_p^{peak} = 10 W$, as a function of time. Pump repetition rate $f = 100 kHz$, input pump duty cycle $D = 30 \%$, fiber length $L = 8 cm$, second mirror reflectivity $R_2 = 77 \%$. (b) Zoom of a single output signal pulse.

8.3 Conclusions

For the first time, a pulsed laser emitting at $\lambda_s = 3.92 \mu m$ based on a commercial double-cladding heavily holmium-doped fluorindate glass fiber is accurately designed via a validated model, by using measured spectroscopic parameters. By employing an input pump with peak power $P_p^{peak} = 10 W$ at the wavelength $\lambda_p = 888 nm$, repetition rate $f = 100 kHz$ and duty cycle $D = 30 \%$, stable output pulses having peak power $P_s^{peak} = 14.62 W$, pulse width FWHM $\tau_s = 72.55 ns$ and pulse energy $E_s = 1.214 \mu J$, are simulated. The proposed gain-switched laser enables stable pulsed output in a wide range of pump repetition rates, from $f = 50 kHz$ to beyond $f = 200 kHz$. Future development will include different co-doping and pumping scheme solutions.

Conclusions

In this PhD thesis, both microwave and optical devices for FiWi networks in 5G and IoT scenarios have been designed, optimized and characterized.

Regarding the microwave devices, firstly a multilayer air-filled SIW array antenna, operating at $f = 60 \text{ GHz}$, has been designed and optimized, also taking into account the feeding transition from the connector to the air-filled SIW. The antenna is promising and will be constructed and characterized at the Institut d'Electronique et des Technologies du numéRique (IETR) in Rennes (France).

Moreover, microwave applicators for industrial monitoring and for thermal ablation of cancer have been designed, constructed, and characterized. In particular:

- (i) a SIW applicator for detecting water in diesel has been designed, starting from the dielectric characterization of water-diesel blends. The applicator has been constructed and characterized, exhibiting an experimental sensitivity $\Delta|S_{21}|/\Delta\rho = 1.42 \text{ mdB/ppm}$ obtained at the frequency $f = 9.76 \text{ GHz}$, with a coefficient of determination $R^2 = 0.94$;
- (ii) needle applicators for thermal ablation of hepatic cancer, with diameters 14G and 16G, have been designed and constructed to work in the ISM band, at $f = 2.45 \text{ GHz}$. The ex-vivo characterization, employing bovine liver, showed good agreement with simulations;
- (iii) a patch antenna applicator matched with SRR metamaterial, for thermal ablation of skin cancer, have been designed and optimized to work in the Ku-band. The applicator has been constructed and characterized, showing good agreement with simulations.

Regarding the optical devices, this PhD thesis has been focused on novel optical sources in the Mid-IR wavelength range, based on commercially available double cladding fluoroindate fibers. In particular:

- (i) a CW laser emitting at $\lambda_s = 3.92 \mu\text{m}$ and pumped at $\lambda_p = 808 \text{ nm}$, has been accurately designed considering a holmium and neodymium co-doped fluoroindate fiber, employing a home-made code solver.

Measured and recovered spectroscopical parameters have been employed to perform a realistic design. A slope efficiency $\eta = 16.67\%$ and an input pump threshold $P_{th} = 0.2\text{ W}$ can be obtained, by employing a fiber length $L_{fiber} = 0.4\text{ m}$, an holmium concentration $N_{Ho} = 8 \times 10^{26}\text{ ions/m}^3$ (4 mol.%), a neodymium concentration $N_{Nd} = 1 \times 10^{26}\text{ ions/m}^3$ (0.5 mol.%), and an output mirror reflectivity $R_{out} = 60\%$;

- (ii) a gain-switched pulsed laser emitting at $\lambda_s = 3.92\ \mu\text{m}$ and pumped at $\lambda_p = 808\text{ nm}$, based on a holmium-heavily-doped fluorindate fiber, has been designed via a validated model, taking into account experimental spectroscopical parameters. Stable output pulses having peak power $P_s^{peak} = 14.62\text{ W}$, pulse width FWHM $\tau_s = 72.55\text{ ns}$ and pulse energy $E_s = 1.214\ \mu\text{J}$, can be obtained by employing an input pump with peak power $P_p^{peak} = 10\text{ W}$, repetition rate $f = 100\text{ kHz}$ and duty cycle $D = 30\%$.

The obtained results have been in part published in the Proceedings of National and International Conferences or on International Journals, as listed at the end of the thesis.

List of publications

International Journals:

- [j1] A. M. Loconsole, V. Portosi, V. V. Francione, A. Anelli, A. Annunziato, M. C. Falconi, F. Prudeniano, "Optimization of a wideband antipodal Vivaldi antenna with metalenses," *International Journal of Microwave and Wireless Technologies*, Nov. 2022. (under review)
- [j2] V. Portosi, A. M. Loconsole, A. Campana, A. Anelli, F. Prudeniano, "A Novel L-shaped Metalens for UltraWideBand (UWB) Antennas," *IEEE Transactions on Antennas and Propagation*, Nov. 2022. (under review)
- [j3] F. Anelli, A. Annunziato, M. Godfrey, A. M. Loconsole, C. Holmes, F. Prudeniano, "Effects of Curvature on Flexible Bragg Grating in Off-Axis Core: Theory and Experiment," *Journal of Lightwave Technology*, Nov. 2022. (under review)
- [j4] A. M. Loconsole, M. C. Falconi, A. Annunziato, S. Cozic, S. Poulain, F. Prudeniano, "Design of a Mid-IR Laser Based on a Ho:Nd-codoped Fluoroindate Fiber," *Journal of Lightwave Technology*, Early Access, Nov. 2022.
- [j5] M. C. Falconi, A. M. Loconsole, F. Prudeniano, "Modeling of rare-earth-doped glass devices and optical parameter indirect evaluation," *Optical Materials*, vol. 132, Oct. 2022.
- [j6] A. M. Loconsole, V. V. Francione, V. Portosi, O. Losito, M. Catalano, A. Di Nisio, F. Attivissimo, F. Prudeniano, "Substrate-integrated waveguide microwave sensor for water-in-diesel fuel applications", *Applied Sciences*, vol. 11, n. 21, Nov. 2021.
- [j7] V. Portosi, A. M. Loconsole, M. Valori, R. Lorusso, I. Fassi, F. Bonelli, G. Pascazio, V. Lampignano, A. Fasano, F. Prudeniano, "Low-cost microwave needle applicator for cancer thermal ablation: feasibility investigation", *IEEE Sensors Journal*, vol. 21, n. 13, pp. 14027-14034, Jul. 2021.
- [j8] A. M. Loconsole, M. C. Falconi, V. Portosi, F. Prudeniano, "Numerical design of a gain-switched pulsed laser at 3.92 μm wavelength based on a

Ho³⁺-doped fluoroindate fiber”, *Journal of Lightwave Technology*, vol. 39, n. 10, pp. 3276–3283, Mar. 2021

- [j9] V. Portosi, A. M. Loconsole, F. Prudenzano, “A split ring resonator-based metamaterial for microwave impedance matching with biological tissue”, *Applied Sciences*, vol. 10, n. 19, pp. 1-14, Sep. 2020.

Proceedings of SPIE:

- [sp1] A. M. Loconsole, M. C. Falconi, A. Annunziato, S. Cozic, S. Poulain, F. Prudenzano, “Feasibility investigation of Ho:Nd codoped InF₃ fibers pumped at 808 nm wavelength,” *SPIE Photonics Europe, “Fiber Lasers and Glass Photonics: Materials through Applications III” (PE114)*, 3–7 April 2022, Strasburg, France.
- [sp2] M. C. Falconi, A. M. Loconsole, A. Annunziato, S. Cozic, S. Poulain, F. Prudenzano, “Design of an Er³⁺: InF₃ fiber laser pumped with red light”, *SPIE Photonics Europe, “Fiber Lasers and Glass Photonics: Materials through Applications III” (PE114)*, 3–7 April 2022, Strasburg, France.
- [sp3] M. C. Falconi, A. Loconsole, D. Laneve L. Thi Ngoc Tran, L. Zur, A. Chiasera, R. Balda, J. Fernandez, P. Gluchowski, A. Lukowiak, M. Ferrari, F. Prudenzano, “Design of active devices based on rare earth doped glass/glass ceramic: from the material characterization to the device refinement”, *SPIE Photonics Europe, “Fiber Lasers and Glass Photonics: Materials through Applications” (PE114)*, 6 – 10 April 2020, Strasburg, France.

Proceedings of International Conferences:

- [c1] A. M. Loconsole, V. Portosi, V. V. Francione, G. Roberto, F. Anelli, F. Prudenzano, “Wideband antipodal Vivaldi antenna with metalenses for GPR applications,” *IEEE Proceedings of 21st Mediterranean Microwave Symposium (MMS 2022)*, 9-13 May 2022, Pizzo Calabro, Italy, pp. 1-5.
- [c2] V. Portosi, A. M. Loconsole, M. Valori, V. Marrocco, F. Bonelli, G. Pascasio, V. Lampignano, A. Fasano, F. Prudenzano, “Refinement of a Microwave Needle Applicator for Cancer Therapy via Metamaterials”, *IEEE Proceedings of 21st Mediterranean Microwave Symposium (MMS 2022)*, 9-13 May 2022, Pizzo Calabro, Italy, pp. 1-5.
- [c3] F. Anelli, V. Portosi, A. M. Loconsole, A. Lacatena, A. Quatela, D. Laneve, F. Prudenzano, “Design of Electromagnetic Shielding for Food

- Pasteurization via Corrugated Waveguide and Graphite Rings,” *IEEE Proceedings of 21st Mediterranean Microwave Symposium (MMS 2022)*, 9-13 May 2022, Pizzo Calabro, Italy, pp. 1-5.
- [c4] A. M. Loconsole, M. C. Falconi, V. Portosi, A. Annunziato, S. Taccheo, F. Prudenzano, “Incoherent Multi-Wavelength Emission in the Wavelength Range 1500-2100 nm”, *IEEE Proceedings of AEIT International Annual Conference 2021, 4-8 October 2021, Milan, Italy*, pp. 1-6.
- [c5] V. Portosi, A. M. Loconsole, M. Valori, R. Lorusso, F. Bonelli, G. Pascazio, V. Lampignano, A. Fasano, R. Lorusso, F. Prudenzano, “Optimization of low-cost needle microwave applicators for cancer therapy”, *IEEE Proceedings of XXXIV General Assembly and Scientific Symposium (GASS) of the International Union of Radio Science (URSI)*, 28 August-4 September 2021, Rome, Italy.
- [c6] M. C. Falconi, A. M. Loconsole, V. Portosi, S. Taccheo, F. Prudenzano, “600 nm-Wide Band ASE optical source exploiting a Tm:Er:Yb:Ho co-doped germanate fiber”, *IEEE Proceedings of 2020 International Conference on Transparent Optical Networks (ICTON)*, 19-23 July 2020, Bari, Italy, pp.1-5, art. no. 9203356. (Invited paper)
- [c7] G. Ricchiuti, M. C. Falconi, A. M. Loconsole, V. Portosi, S. Cozic, S. Poulain, F. Prudenzano, “Mid-infrared supercontinuum generation in ZBLAN fluoride/fluoroindate fibers at wavelength $\lambda=2.9 \mu\text{m}$ ”, *IEEE Proceedings of 2020 International Conference on Transparent Optical Networks (ICTON)*, 19-23 July 2020, Bari, Italy, pp.1-5, art. no. 92031.
- [c8] V. Portosi, A. M. Loconsole, M. Valori, R. Lorusso, F. Bonelli, G. Pascazio, V. Lampignano, A. Fasano, R. Lorusso, F. Prudenzano, “Feasibility investigation of low-cost microwave needle applicator for thermal ablation cancer therapy”, *IEEE Proceedings of 15th IEEE International Symposium on Medical Measurements and Applications 2020*, 1-3 June 2020, Bari, Italy, pp.1-6.
- [c9] M. C. Falconi, D. Laneve, C. Clemente, G. Ricchiuti, A. Loconsole, V. Portosi, A. Crudele, G. Galzerano, F. Prudenzano, “Fluoride Glass Pulse Laser in Middle Infrared Wavelength Range”, *CLEO/EUROPE-EQEC 2019*, 23 – 27 June 2019, Munich, Germany.

International Conferences:

- [i1] M.C. Falconi, A.M. Loconsole, A. Annunziato, F. Anelli, Y. Wang, G. Galzerano, F. Prudenzano, “Simulation of a Dy³⁺:ZBLAN fiber laser

- passively Q-switched with a SESAM,” *Photoluminescence in Rare Earths: Photonic Materials (PRE'22-Poland)*, 11–14 September 2022, Szczawnica, Poland.
- [i2] M.C. Falconi, A.M Loconsole, A. Annunziato, F. Prudenzano, “Numerical investigation of an Er³⁺:IFG fiber for lasing at 3.5 μm,” *Photoluminescence in Rare Earths: Photonic Materials (PRE'22-Poland)*, 11–14 September 2022, Szczawnica, Poland.
- [i3] A. M. Loconsole, G. Roberto, M. C. Falconi, D. Laneve, V. Portosi, A. Massaro, N. Savino, F. Prudenzano, “Compact Vivaldi antipodal SIW antenna for GPR applications,” *XXXIV General Assembly and Scientific Symposium (GASS) of the International Union of Radio Science (URSI)*, 28 August-4 September 2021, Rome, Italy.

Proceedings of National Conferences:

- [p1] A. M. Loconsole, M. C. Falconi, A. Annunziato, V. Portosi, F. Prudenzano, “Design of a Ho:Nd-codoped fluoroindate fiber for Mid-IR laser emission,” *IEEE Proceedings of 2022 Italian Conference on Optics and Photonics*, 15-17 June 2022, Trento, Italy.
- [p2] M. C. Falconi, A. M. Loconsole, A. Annunziato, F. Anelli, F. Prudenzano, “Design of an erbium-doped fluoroindate fiber laser pumped at 635 nm,” *IEEE Proceedings of 2022 Italian Conference on Optics and Photonics*, 15-17 June 2022, Trento, Italy.
- [p3] A. M. Loconsole, M. C. Falconi, D. Laneve, V. Portosi, S. Taccheo, F. Prudenzano, “Wideband optical amplifier based on Tm:Er:Yb:Ho codoped germanate glass”, *IEEE Proceedings of 2020 Italian Conference on Optics and Photonics*, 8-11 September 2020, Parma, Italy, pp. 1-4.
- [p4] A. M. Loconsole, M. C. Falconi, D. Laneve, V. Portosi, S. Taccheo, F. Prudenzano, “Tm:Er:Yb:Ho amplified spontaneous emission source operating from 1480 nm to 2100 nm”, *IEEE Proceedings of 2020 Italian Conference on Optics and Photonics*, 8-11 September 2020, Parma, Italy, pp. 1-4.

National Conferences:

- [n1] M. C. Falconi, A. M. Loconsole, A. Annunziato, F. Anelli, Y. Wang, G. Galzerano, F. Prudenzano, “Modeling of a SESAM-based dysprosium-doped ZBLAN fiber laser operating in Q-switching regime,” *Riunione*

Nazionale di Elettromagnetismo (RiNEm) 2022, 18-21 September 2022, Catania, Italy.

- [n2] A. M. Loconsole, V. Portosi, F. Anelli, A. Annunziato, V. V. Francione, M. C. Falconi, F. Prudeniano, “Low-profile antipodal Vivaldi antenna (AVA) for ground-penetrating radar applications,” *Riunione Nazionale di Elettromagnetismo (RiNEm) 2022*, 18-21 September 2022, Catania, Italy.
- [n3] V. Portosi, A.M. Loconsole, M. Valori, V. Marrocco, I. Fassi, F. Bonelli, G. Pascazio, V. Lampignano, A. Fasano, F. Prudeniano, “Design of Metamaterials for the Refinement of Mini-invasive Microwave Needle Applicator,” *VI Convegno Nazionale “Interazione tra Campi Elettromagnetici e Biosistemi” (ICEmB 2022)*, 8-10 June 2022, Cagliari, Italy.
- [n4] V. Portosi, A. M. Loconsole, M. Valori, V. Marrocco, F. Bonelli, G. Pascazio, V. Lampignano, A. Fasano, F. Prudeniano, “A low-cost microwave needle applicator for cancer ablation”, *Riunione Nazionale di Elettromagnetismo (RiNEm) 2020*, 26-27 September 2020, Rome, Italy.

References

- [1] S. Ghosh, D. Sen, “An Inclusive Survey on Array Antenna Design for Millimeter-Wave Communications,” *IEEE Access*, vol. 7, pp. 83137–83161, 2019.
- [2] T. Potelon, M. Ettorre, L. Le Coq, T. Bateman, J. Francey, R. Sauleau, “Reconfigurable CTS Antenna Fully Integrated in PCB Technology for 5G Backhaul Applications,” *IEEE Trans. Antennas Propag.*, vol 67, no. 6, pp. 3609–3618, Jun. 2019.
- [3] M. Li, and K. M. Luk, “Low-Cost Wideband Microstrip Antenna Array for 60-GHz Applications,” *IEEE Trans. Antennas Propag.*, vol 62, no. 6, pp. 3012–3018, Jun. 2014.
- [4] X.-P. Chen, K. Wu, L. Han, and F. He, “Low-cost high gain planar antenna array for 60-GHz band applications,” *IEEE Trans. Antennas Propag.*, vol. 58, no. 6, pp. 2126–2129, Jun. 2010.
- [5] K. Gong, Z. N. Chen, X. Qing, P. Chen, and W. Hong, “Substrate integrated waveguide cavity-backed wide slot antenna for 60-GHz bands,” *IEEE Trans. Antennas Propag.*, vol. 60, no. 12, pp. 6023–6026, Dec. 2012.
- [6] Y. Miura, J. Hirokawa, M. Ando, Y. Shibuya, and G. Yoshida, “Double-layer full-corporate-feed hollow-waveguide slot array antenna in the 60 GHz-band,” *IEEE Trans. Antennas Propag.*, vol. 59, no. 8, pp. 2488–2851, Aug. 2011.
- [7] F. Foglia Manzillo, M. Ettorre, M. S. Lahti, K. T. Kautio, D. Lelaidier, E. Seguenot, and R. Sauleau, “A Multilayer LTCC Solution for Integrating 5G Access Point Antenna Modules,” *IEEE Trans. Microw. Theory Tech.*, vol. 64, no. 7, Jul. 2016.
- [8] M. Bozzi, A. Georgiadis, K. Wu, “Review of substrate-integrated waveguide circuits and antennas,” *IET Microw. Antennas Propag.*, vol. 5, no. 8, pp. 909–920, Jul. 2011.
- [9] O. Losito, V. Portosi, G. Venanzoni, F. Bigelli, D. Mencarelli, P. Scalmati, C. Renghini, P. Carta, F. Prudeniano, “Feasibility investigation of

- SIW cavity-backed patch antenna array for Ku band applications,” *Appl. Sci.*, vol. 9, no. 7, Mar. 2019.
- [10] T. Castellano, O. Losito, L. Mescia, M. A. Chiapperino, G. Venanzoni, D. Mencarelli, G. Angeloni, C. Renghini, P. Carta, F. Prudeniano, “F. Feasibility investigation of low cost substrate integrated waveguide (SIW) directional couplers,” *Prog. Electromagn. Res. PIER*, vol. 59, pp. 31–44, March 2014.
- [11] D. Mencarelli, A. Morini, F. Prudeniano, G. Venanzoni, F. Bigelli, O. Losito, M. Farina, “Broadband single-layer slotted array antenna in SIW technology,” *IEEE Antennas Wirel. Propag. Lett.*, vol. 15, pp. 263–265, Jun. 2015.
- [12] M. A. Chiapperino, O. Losito, T. Castellano, G. Venanzoni, L. Mescia, G. Angeloni, C. Renghini, P. Carta, P. Potenza, F. Prudeniano, “Dual-Band substrate integrated waveguide resonator based on sierpinski carpet,” *Prog. Electromagn. Res. PIER*, vol. 57, pp. 1–12, Aug. 2015.
- [13] G. Venanzoni, D. Mencarelli, A. Morini, M. Farina, O. Losito, F. Prudeniano, “Compact substrate integrated waveguide six-port directional coupler for X-band applications”, *Microw. Opt. Technol. Lett.*, vol. 57, pp. 2589–2592, Aug. 2015.
- [14] G. Venanzoni, D. Mencarelli, A. Morini, M. Farina, O. Losito, F. Prudeniano, “Compact double-layer substrate integrated waveguide magic Tee for X-band applications”. *Microw. Opt. Technol. Lett.*, vol. 58, pp. 932–936, Feb. 2016.
- [15] G. Venanzoni, D. Mencarelli, A. Morini, M. Farina, F. Prudeniano, “Review of substrate integrated waveguide circuits for beam-forming networks working in X-band,” *Appl. Sci. vol. 9 no. 5*, Mar. 2019.
- [16] Feng Xu and K. Wu, “Guided-wave and leakage characteristics of substrate integrated waveguide,” *IEEE Trans. Microw. Theory Tech.*, vol. 53, no. 1, pp. 66-73, Jan. 2005.
- [17] Y. J. Cheng, K. Wu, W. Hong, “Power Handling Capability of Substrate Integrated Waveguide Interconnects and Related Transmission Line Systems,” *IEEE Trans. Adv. Packag.*, vol. 3, no. 4, pp. 900–909, Nov. 2008.
- [18] Y. Cassivi, L. Perregrini, P. Arcioni, M. Bressan, K. Wu, G. Conciauro, “Dispersion characteristics of substrate integrated rectangular waveguide”. *IEEE Microwave & Wirel. Compon. Lett.*, vol. 12, no. 9, pp. 333–335, Sep. 2002
- [19] K. Y. Kapusuz, A. V. Berghe, S. Lemey, H. Rogier, “Partially Filled Half-Mode Substrate Integrated Waveguide Leaky-Wave Antenna for 24

- GHz Automotive Radar,” *IEEE Antennas Wirel. Propag. Lett.*, vol. 20, no. 1, pp. 33-37, Jan. 2021
- [20] F. Parment, A. Ghiotto, T.-P. Vuong, J.-M. Duchamp, K. Wu, “Millimeter-wave air-filled substrate integrated waveguide slot array antenna,” *Electron. Lett.*, vol. 53, no. 11, Mar. 2017.
- [21] A. Belenguer, H. Esteban, A. L. Borja, V. E. Boria, “Empty SIW Technologies: A Major Step Toward Realizing Low-Cost and Low-Loss Microwave Circuits,” *IEEE Microw. Mag.*, vol. 20, no. 3, pp. 24-45, Mar. 2019.
- [22] A. M. Loconsole, V. V. Francione, V. Portosi, O. Losito, M. Catalano, A. Di Nisio, F. Attivissimo, F. Prudenziario, “Substrate-integrated waveguide microwave sensor for water-in-diesel fuel applications”, *Appl. Sci.*, vol. 11, n. 21, Nov. 2021.
- [23] P. Prakash, M.C. Converse, J.G. Webster, D.M. Mahvi, “An optimal sliding choke antenna for hepatic microwave ablation,” *IEEE Trans. Biomed. Eng.*, vol. 56, pp. 2470 – 2476, Jun. 2009.
- [24] H. Luyen, S.C. Hagness, N. Behdad, “A balun-free helical antenna for minimally invasive microwave ablation,” *IEEE Trans. Antennas Propag.*, vol. 63, pp. 959 – 965, Mar. 2015.
- [25] C.L. Brace, P.F. Laeseke, D.W. van der Weide, F.T. Lee, “Microwave ablation with a triaxial antenna: results in ex vivo bovine liver,” *IEEE Trans. Microw. Theory Tech.*, vol. 53, pp. 215-220, Jan. 2005.
- [26] S. Labonte, A. Blais, S.R. Legault, H.O. Ali, L. Roy, “Monopole antennas for microwave catheter ablation,” *IEEE Trans. Microw. Theory Tech.*, vol. 44, pp. 1832 – 1840, Oct. 1996.
- [27] Z.A. Ibitoye, E.O. Nwoye, M.A. Aweda, A.A. Oremosu, C.C. Annunobi, O.N. Akanmu, “Optimization of dual slot antenna using floating metallic sleeve for microwave ablation,” *Med. Eng. Phys.*, vol. 37, pp.384 – 391, Apr. 2015.
- [28] M. Cavagnaro, C. Amabile, P. Bernardi, S. Pisa, N. Tosoratti, “A minimally invasive antenna for microwave ablation therapies: design, performances and experimental assessment,” *IEEE. Trans. Biomed. Eng.*, vol. 58, pp. 949-959, Apr. 2011.
- [29] I. Longo, G. Biffi Gentili, M. Cerretelli, N. Tosoratti, “A coaxial antenna with miniaturized choke for minimally invasive interstitial heating,” *IEEE. Trans. Biomed. Eng.*, vol. 50, pp. 82-88, Jan. 2003.

- [30] H. Luyen, S.C. Hagness, N. Behdad, “Reduced-diameter designs of coax-fed microwave ablation antennas equipped with baluns,” *IEEE Antennas Wirel. Propag. Lett.*, vol. 16, pp. 1385 – 1388, Dec. 2016.
- [31] P. Gas, B. Szymanik, “Shape optimization of the multi-slot coaxial antenna for local hepatic heating during microwave ablation,” in *Proc. 2018 IIPhDW*, Swinoujście, Poland, 2018.
- [32] V. Portosi, A.M. Loconsole, F. Prudenzi, “A split ring resonator-based metamaterial for microwave impedance matching with biological tissue”, *Appl. Sci.*, vol.10, no. 19, Sep. 2020.
- [33] G. Andria, F. Attivissimo, A. Di Nisio, A. M. L. Lanzolla, P. Larizza, S. Selicato, “Development and performance evaluation of an electromagnetic tracking system for surgery navigation,” *Measurement*, vol. 148, pp.1-7, Dec. 2019.
- [34] C. Caloz, T. Itoh, *Electromagnetic metamaterials: transmission line theory and microwave applications*, John Wiley & Sons, Inc., 2006.
- [35] N. Ghazisaidi, M. Maier, “Fiber-wireless (FiWi) access networks: Challenges and opportunities,” *IEEE Network*, vol. 25, no. 1, pp. 36-42, Jan.-Feb. 2011.
- [36] A. Kanno, K. Inagaki, I. Morohashi, T. Sakamoto, T. Kuri, I. Hosako, T. Kawanishi, Y. Yoshida, and K. Kitayama, “40 Gb/s W-band (75–110 GHz) 16-QAM radio-over-fiber signal generation and its wireless transmission,” *Opt. Express*, vol. 19, no. 26, pp. B56-B63, 2011.
- [37] J. He, B. Li, L. Deng, M. Tang, L. Gan, S. Fu, P. P. Shum, D. Liu, “Experimental investigation of inter-core crosstalk tolerance of MIMO-OFDM/OQAM radio over multicore fiber system,” *Opt. Express*, vol. 24, no. 12, pp. 13418-13428, 2016.
- [38] D. Novak, Z. Ahmed, R. B. Waterhouse and R. S. Tucker, “Signal generation using pulsed semiconductor lasers for application in millimeter-wave wireless links,” *IEEE Trans. Microw. Theory Tech.*, vol. 43, no. 9, pp. 2257-2262, Sept. 1995.
- [39] J. Kim, K. Jung, J. Shin, C.-G. Jeon, D. Kwon, “Femtosecond Laser-Based Microwave Signal Generation and Distribution,” *J. Lightwave Technol.*, vol. 34, no. 20, pp. 4631-4638, 2016.
- [40] L. Zhang, F. Guan, L. Zhang, Y. Jiang, “Next generation mid-infrared fiber: fluorindate glass fiber,” *Opt. Mater. Express*, vol. 12, no. 4, pp. 1683-1707, Mar. 2022.

- [41] Q. Luo, H. L. Xu, S. A. Hosseini, J.-F. Daigle, F. Théberge, M. Sharifi, S. L. Chin, “Remote sensing of pollutants using femtosecond laser pulse fluorescence spectroscopy,” *Appl. Phys. B*, vol. 82, pp. 105-109, Nov. 2005.
- [42] S. B. Mirov, I. S. Moskalev, S. Vasilyev, V. Smolski, V. V. Fedorov, D. Martyshkin, J. Peppers, M. Mirov, A. Dergachev, V. Gapontsev, “Frontiers of Mid-IR Lasers Based on Transition Metal Doped Chalcogenides,” *IEEE J. Sel. Top. Quantum Electron.*, vol. 24, no. 5, pp. Sep. 2018.
- [43] A. E. Klingbeil, J. B. Jeffries, R. K. Hanson, “Temperature-dependent mid-IR absorption spectra of gaseous hydrocarbons,” *J. Quant. Spectrosc. Radiat. Transf.*, vol. 107, vol. 3, pp. 407-420, Oct. 2007.
- [44] J. M. Bakker, I. Compagnon, G. Meijer, G. von Helden, M. Kabelac, P. Hobza, M. S. de Vries, “The mid-IR absorption spectrum of gas-phase clusters of the nucleobases guanine and cytosine,” *Phys. Chem. Chem. Phys.*, vol. 6, no. 10, pp. 2810-2815, Apr. 2004.
- [45] K. Wang, D.-W. Sun, H. Pu, “Emerging non-destructive terahertz spectroscopic imaging technique: Principle and applications in the agri-food industry,” *Trends Food Sci. Technol.*, vol. 67, pp. 93-105, Sep. 2017.
- [46] Z. Zhou, Z. Wang, W. Huang, Y. Cui, H. Li, M. Wang, X. Xi, S. Gao, Y. Wang, “Towards high-power mid-IR light source tunable from 3.8 to 4.5 μm by HBr-filled hollow-core silica fibres,” *Light: Sci. Appl.*, vol. 11, Jan. 2022.
- [47] R. M. Schwartz, D. Woodbury, J. Isaac, P. Sprangle, H. M. Milchberg, “Remote detection of radioactive material using mid-IR laser-driven electron avalanche,” *Sci. Adv.*, vol. 5, no. 3, Mar. 2019.
- [48] M. C. Falconi, D. Laneve, M. Bozzetti, T. T. Fernandez, G. Galzerano, F. Prudenzano, “Design of an Efficient Pulsed Dy³⁺: ZBLAN Fiber Laser Operating in Gain Switching Regime,” *J. Light. Technol.*, vol. 36, no. 23, pp. 5327–5333, Sep. 2018.
- [49] L. Sójka, L. Pajewski, S. Lamrini, M. Farries, T. M. Benson, A. B. Seddon, and S. Sujecki, “High Peak Power Q-switched Er:ZBLAN Fiber Laser,” *J. Light. Technol.*, vol. 39, no. 20, pp. 6572-6578, Jul. 2021.
- [50] E. A. Anashkina, “Laser Sources Based on Rare-Earth Ion Doped Tellurite Glass Fibers and Microspheres,” *Fibers*, vol. 8, no. 30, pp. 1-17, May 2020.
- [51] M. C. Falconi, G. Palma, F. Starecki, V. Nazabal, J. Troles, J.-L. Adam, S. Taccheo, M. Ferrari, and F. Prudenzano, “Dysprosium-doped

- chalcogenide master oscillator power amplifier (MOPA) for mid-IR emission,” *J. Lightw. Technol.*, vol. 35, no. 2, pp. 265–273, Jan. 2017.
- [52] M. R. Majewski, R. I. Woodward, J.-Y. Carrée, S. Poulain, M. Poulain, S. D. Jackson, “Emission beyond 4 μm and mid-infrared lasing in a dysprosium-doped indium fluoride (InF_3) fiber,” *Opt. Lett.*, vol. 43, no. 8, pp. 1926-1929, 2018.
- [53] Y. Wang, F. Jobin, S. Duval, V. Fortin, P. Laporta, M. Bernier, G. Galzerano, R. Vallée, “Ultrafast Dy^{3+} :fluoride fiber laser beyond 3 μm ,” *Opt. Lett.*, vol. 44, pp. 395-398, Jan. 2019.
- [54] M. Saad, R. Pafchek, P. Foy, Z. Jiang, D. Gardner, P. Hawkins, “Indium Fluoride Glass Fibers for Mid-Infrared applications,” *WSOF2015*, Hong Kong, China, 4-6 Nov. 2015, paper WW4A.3.
- [55] J. Pisarska, “IR transmission and emission spectra of erbium ions in fluorindate glass,” *J. Non-Cryst. Solids*, vol. 345-346, pp. 382-385, Oct. 2004.
- [56] V. A. Jerez, C. B. de Araujo, Y. Messaddeq, “Dynamics of energy transfer and frequency upconversion in Tm^{3+} doped fluorindate glass,” *J. Appl. Phys.*, vol. 96, no. 5, 2530-2534, Sep. 2004.
- [57] L. J. Borrero-Gonzalez, G. Galleani, D. Manzani, L. A. O. Nunes, S. J. L. Ribeiro, “Visible to infrared energy conversion in Pr^{3+} - Yb^{3+} co-doped fluorindate glasses”, *Opt. Mater.*, vol. 35, no. 12, pp. 2085-2089, Oct. 2013.
- [58] M. Kochanowicz, J. Zmojda, A. Baranowska, P. Miluski, M. Lesniak, M. Kuwik, J. Pisarska, W. A. Pisarski, J. Dorosz, D. Dorosz, “Near-IR and mid-IR luminescence end energy transfer in fluorindate glasses co-doped with Er^{3+} / Tm^{3+} ,” *Opt. Mater. Express*, vol. 9, no. 12, Dec. 2019.
- [59] M. Kochanowicz, J. Zmojda, P. Miluski, A. Baranowska, M. Kuwik, W. A. Pisarski, J. Pisarska, J. Dorosz, D. Dorosz, “Sensitization of Ho^{3+} -doped fluorindate glasses for near and mid-infrared emission,” *Opt. Mater.*, vol. 101, Mar. 2020, Art. no 109707.
- [60] Le Verre Fluoré, Catalog 2019, Bruz, Brittany, France. [Online]. Available: <https://leverrefluore.com/wp-content/uploads/2019/06/CatalogLVF-2019.pdf>
- [61] F. Maes, V. Fortin, S. Poulain, M. Poulain, J.-Y. Carrée, M. Bernier, R. Vallée, “Room-temperature fiber laser at 3.92 μm ”, *Optica*, vol. 5, no. 7, pp. 761-764, Jul. 2018.

- [62] F. Zhou, J. Li, H. Luo, F. Quellette, Y. Liu, "Numerical Analysis of 3.92 μm Dual-Wavelength Pumped Heavily-Holmium-Doped Fluoroindate Fiber Lasers," *J. Light. Technol.*, vol. 39, no. 2, pp. 633-645, Jan. 2021.
- [63] A. M. Loconsole, M. C. Falconi, V. Portosi, F. Prudeniano, "Numerical Design of a Gain-Switched Pulsed Laser at 3.92 μm Wavelength Based on a Ho³⁺-Doped Fluoroindate Fiber," *J. Lightw. Technol.*, vol. 39, no. 10, pp. 3276-3283, May 2021.
- [64] M. R. Majewski, S. D. Jackson, "Numerical Design of 4 μm -Class Dysprosium Fluoride Fiber Lasers," *J. Light. Technol.*, vol. 39, no. 15, pp. 5103-5110, May 2021.
- [65] P. Wang, J. Zhang, J. Zhang, S. Jia, L. Wang, Y. Ning, H. Peng, G. Farrell, S. Wang, R. Wang, "3.5 μm emission in Er³⁺ doped fluoroindate glasses under 635 nm laser excitation," *J. Lumin.*, vol. 237, Sep. 2021.
- [66] H. He, Z. Jia, T. Wang, Y. Ohishi, W. Qin, G. Qin, "Intense emission at \sim 3.3 μm from Er³⁺-doped fluoroindate glass fiber," *Opt. Lett.*, vol. 46, no. 5, pp. 1057-1060, Feb. 2021.
- [67] A. Florez, S. L. Oliveira, M. Florez, L. A. Gomez, L. A. O. Nunes, "Spectroscopic characterization of Ho³⁺ ion-doped fluoride glass," *J. Alloys Compd.*, vol. 418, pp. 238-242, Feb. 2006.
- [68] S. L. Oliveira, M. J. V. Bell, A. Florez, L. A. O. Nunes, "Spectroscopic investigation of 2.0 μm emission in Ho³⁺-doped fluoroindate glasses," *J. Phys. D: Appl. Phys.*, vol. 39, pp. 3230-3234, Jul. 2006.
- [69] A. Berrou, C. Kieleck, M. Eichhorn, "Mid-infrared lasing from Ho³⁺ in bulk InF₃ glass," *Opt. Lett.*, vol. 40, no. 8, pp. 1699-1701, Apr. 2015.
- [70] L. Gomes, V. Fortin, M. Bernier, R. Vallée, S. Poulain, M. Poulain, S. D. Jackson, "The basic spectroscopic parameters of Ho³⁺-doped fluoroindate glass for emission at 3.9 μm ," *Opt. Mater.*, vol. 60, pp. 618-626, Sep. 2016.
- [71] L. Gomes, V. Fortin, M. Bernier, F. Maes, R. Vallée, S. Poulain, M. Poulain, S. D. Jackson, "Excited state absorption and energy transfer in Ho³⁺-doped indium fluoride glass," *Opt. Mater.*, vol. 66, pp. 519-526, Feb. 2017.
- [72] S. Jia, Z. Jia, C. Yao, L. Zhang, Y. Feng, G. Qin, Y. Ohishi, W. Qin, "2875 nm Lasing From Ho³⁺-Doped Fluoroindate Glass Fibers," *IEEE Photon. Technol. Lett.*, vol. 30, no. 4, pp. 323-326, Feb. 2018.
- [73] K. S. Wu, D. Ottaway, J. Munch, D. G. Lancaster, S. Bennetts, S. D. Jackson, "Gain-switched holmium-doped fibre laser," *Optics Express*, vol. 17, no. 23, pp. 20872-20877, Nov. 2009.

- [74] J. Li, Y. Yang, D. D. Hudson, Y. Liu, S. D. Jackson, “A tunable Q-switched Ho³⁺-doped fluoride fiber laser,” *Laser Phys. Lett.*, vol. 10, Feb. 2013.
- [75] M. C. Falconi, A. M. Loconsole, A. Annunziato, S. Cozic, S. Poulain, F. Prudenziato, “Design of an Er³⁺:InF₃ fiber laser pumped with red light,” Proc. SPIE 12142, Fiber Lasers and Glass Photonics: Materials through Applications III, art. no. 121420Z, *SPIE Europe 2022*, 3-7 April 2022, Strasbourg, France.
- [76] R. Wang, J. Zhang, H. Zhao, X. Wang, S. Jia, H. Guo, S. Dai, P. Zhang, G. Brambilla, S. Wang, P. Wang, “3.9 μm emission and energy transfer in ultra-low OH⁻, Ho³⁺/Nd³⁺ co-doped fluorindate glasses,” *J. Lumin.*, vol. 225, Sep. 2020, Art. no. 117363.
- [77] Z. Zhang, R. Wang, M. Liu, S. Wang, J. Zhang, G. Brambilla, S. Jia, P. Wang, “Enhanced 3.9 μm emission from diode pumped Ho³⁺/Eu³⁺ codoped fluorindate glasses,” *Opt. Lett.*, vol. 46, no. 9, pp. 2031-2034, Apr. 2021.
- [78] P. Paradis, V. Fortin, Y. O. Aydin, R. Vallée, M. Bernier, “10 W-level gain-switched all-fiber laser at 2.8 μm ,” *Opt. Lett.*, vol. 43, no. 13, pp. 3196-3199, Jul. 2018.
- [79] F. Jobin, V. Fortin, F. Maes, M. Bernier, and R. Vallée, “Gain-switched fiber laser at 3.55 μm ,” *Opt. Lett.*, vol. 43, no. 8, pp. 1770–1773, Apr. 2018.
- [80] N. Bawden, H. Matsukuma, O. Henderson-Sapir, E. Klantsataya, S. Tokita, and D. J. Ottaway, “Actively Q-switched dual-wavelength pumped Er³⁺:ZBLAN fiber laser at 3.47 μm ,” *Opt. Lett.*, vol. 43, no. 11, pp. 2724–2727, Jun. 2018.
- [81] J. B. Pendry, A. J. Holden, D. J. Robbins, W. J. Stewart, “Magnetism from conductors and enhanced nonlinear phenomena,” *IEEE Trans. Microw. Theory Tech.*, vol. 47, pp. 2075–2084, 1999.
- [82] H. Attia, L. Yousefi, O. M. Ramahi, “Analytical model for calculating the radiation field of microstrip antennas with artificial magnetic superstrates: Theory and experiment,” *IEEE Trans. Antennas Propag.*, vol. 59, pp. 1438–1445, 2001.
- [83] S. Maslovski, P. Ikonen, I. Kolmakov, S. Tretyakov, “Artificial magnetic material based on the new magnetic particle: Metasolenoid,” *Prog. Electromagn. Res. PIER*, vol. 54, pp. 61–81, 2005.

- [84] Y. H. Liu, X. P. Zhao, “Investigation of anisotropic negative permeability medium cover for patch antenna”, *IET Microw. Antennas Propag.*, vol. 2, pp. 737–744, 2008.
- [85] Connector Southwest Microwave 1892-04A-9 datasheet. Available online: <https://www.hasco-inc.com/content/Southwest/End%20Launch/Jack/1892-04A-9.pdf>
- [86] W. Digman, “Effects of Fuel Contamination on Corrosion of Aircraft Fuel Systems”. *SAE Technical Paper*, Warrendale, PA, USA, 1962.
- [87] I. M. Atadashi, M. K. Aroua, A. R. Abdul Aziz, N. M. N. Sulaiman, “The effects of water on biodiesel production and refining technologies: A review,” *Renew. Sustain. Energy Rev.*, vol. 16, pp. 3456–3470 2012.
- [88] L. C. Oliveira, E. G. Pereira, R. C. Oliveira, M. R. A. Morais, A. M. N. Lima, H. Neff, “SPR sensor for tampering detection in biofuels”, *In Proc. of the 2015 IEEE International Instrumentation and Measurement Technology Conference (I2MTC)*, Pisa, Italy, 11–14 May 2015.
- [89] C. H. Lee, Y. Jeong, H. Ashraf, “Rectangular Cavity Sensor for Distinguishing Between Normal and High-Drivability-Index Gasolines”. *IEEE Access*, vol. 8, pp. 182193–182203, 2020.
- [90] S. Kulkarni, M. S. Joshi, “Design and Analysis of Shielded Vertically Stacked Ring Resonator as Complex Permittivity Sensor for Petroleum Oils,” *IEEE Trans. Microw. Theory Tech.*, vol. 63, pp. 2411–2417, 2015.
- [91] G. A. Eyebe, N. Sama, N. Boubekeur, F. Domigue, “Microwave Sensing Schemes of CPW Resonators Fully Printed on Humidity Sensitive Substrates,” *IEEE Microw. Wirel. Compon. Lett.*, vol. 29, pp. 303–305, 2020.
- [92] SPEAG, DAK Professional Handbook V 1.10, August 2013.
- [93] Keysight, FieldFox Handheld Analyzers 4/6.5/9/14/18/26.5/32/44/50 GHz datasheet. Available online: <https://www.keysight.com/it/en/assets/7018-03314/data-sheets/5990-9783.pdf>.
- [94] D. M. Pozar, *Microwave Engineering*, 3rd ed.; Wiley: Hoboken, NJ, USA, 2004.
- [95] A. Nella, A. Gandhi, “Lumped Equivalent Models of Narrowband Antennas and Isolation Enhancement in a Three Antennas System”. *Radiengineering*, vol. 27, pp. 646–653 2018.
- [96] G. Andria, F. Attivissimo, A. Di Nisio, A. Trotta, S. M. Camporeale, P. Pappalardi, “Design of a microwave sensor for measurement of water in fuel contamination”. *Measurement*, vol. 136, pp. 74–81 2019.

- [97] Q. Xue, X. Tang, Y. Li, H. Liu, X. Duan, "Contactless and Simultaneous Measurement of Water and Acid contaminations in Oil Using a Flexible Microstrip Sensor". *ACS Sens.*, vol. 5, pp. 171–179, 2020.
- [98] J.C. Lin, P. Bernardi, S. Pisa, M. Cavagnaro, E. Piuzzi, "Antennas for medical therapy and diagnostics," *Modern Antenna Handbook*, C.A. Balanis, John Wiley & Sons Inc. Publication, USA, 2008, pp. 1377–1401.
- [99] P. Bernardi, M. Cavagnaro, J.C. Lin, S. Pisa, E. Piuzzi, "Distribution of SAR and temperature elevation induced in a phantom by a microwave cardiac ablation catheter," *IEEE Trans. Microw. Theory Tech.*, vol. 52, pp. 1978–1986, Aug. 2004.
- [100] H.H. Pennes, "Analysis of tissue and arterial blood temperatures in the resting human forearm," *J. Appl. Physiol.*, vol. 1, pp. 5-34, Aug. 1948.
- [101] E. Ewertowska, R. Quesada, A. Radosevic, A. Andaluz, X. Moll, F. García Arnas, E. Berjano, F. Burdío, M. Trujillo, "A clinically oriented computer model for radiofrequency ablation of hepatic tissue with internally cooled wet electrode," *Int. J. Hyperthermia*, vol. 35, Oct. 2018.
- [102] M. Cavagnaro, C. Amabile, P. Bernardi, S. Pisa, N. Tosoratti, "A minimally invasive antenna for microwave ablation therapies: design, performances and experimental assessment," *IEEE. Trans. Biomed. Eng.*, vol. 58, pp. 949-959, Apr. 2011.
- [103] A.P. O'Rourke, M. Lazebnik, J.M. Bertram, M.C. Converse, S.C. Hagness, J.G. Webster, D.M. Mahvi, "Dielectric properties of human normal, malignant and cirrhotic liver tissue: in vivo and ex vivo measurements from 0.5 to 20 GHz using a precision open-ended coaxial probe," *Phys. Med. Biol.*, vol. 52, pp. 4707-4719, Jul. 2007.
- [104] P. Gas, B. Szymanik, "Shape optimization of the multi-slot coaxial antenna for local hepatic heating during microwave ablation," in *Proc. 2018 IIPhDW*, Swinoujście, Poland, 2018.
- [105] W. Scarcia, G. Palma, M.C. Falconi, F. De Leonardis, V.M.N. Passaro, F. Prudeniano, "Electromagnetic modelling of fiber sensors for low-cost and high sensitivity temperature monitoring," *Sensors*, vol. 15, pp. 29855-29870, Nov. 2015.
- [106] D. Andreuccetti, R. Fossi, C. Petrucci, "An Internet Resource for the Calculation of the Dielectric Properties of Body Tissues in the Frequency Range 10 Hz–100 GHz", IFAC-CNR: Florence, Italy, 1997; Available online: <http://niremf.ifac.cnr.it/tissprop>

- [107] Y. Gong, G. Wang, “Superficial tumor hyperthermia with flat left-handed metamaterial lens”. *Prog. Electromagn. Res. PIER*, vol. 98, pp. 389–405, 2009.
- [108] M. C. Velázquez-Ahumada, M. J. Freire, R. Marqués, “Metamaterial focusing device for microwave hyperthermia”. *Microw. Opt. Technol. Lett.*, vol. 53, pp. 2868–2872, 2011.
- [109] Y. Tao, G. Wang, “Conformal hyperthermia of superficial tumor with left-handed metamaterial lens applicator” *IEEE. Trans. Biomed. Eng.*, vol. 59, pp. 3525–3530, 2012.
- [110] D. Vrba, J. Vrba, “Novel applicators for local microwave hyperthermia based on zeroth-order mode resonator metamaterial,” *Int. J. Antennas Propag.* 2014.
- [111] L. Leggio, O. de Varona, E. A. Dadrasnia, “A comparison between different schemes of microwave cancer hyperthermia treatment by means of left-handed metamaterial lenses,” *Prog. Electromagn. Res. PIER*, vol. 150, pp. 73–87, 2015.
- [112] K. Lias, N. Buniyamin, M. Zulkarnaen, “Simulation study of an EBG-M applicator towards non-invasive breast hyperthermia cancer procedure” *J. Teknol.*, vol. 78, pp. 75–81, 2016.
- [113] Y. Tao, E. Yang, G. Wang, “Left-handed metamaterial lens applicator with build-in cooling feature for superficial tumor hyperthermia,” *Appl. Comput. Electromagn. Soc. J.*, vol. 32, pp. 1029–1034, 2017.
- [114] A. Florez, J. F. Martinez, M. Florez, P. Porcher, “Optical transition probabilities and compositional dependence of Judd-Ofelt parameters of Nd³⁺ ions in fluoroindate glasses,” *J. Non-Cryst. Solids*, vol. 284, pp. 261-267, 2001.
- [115] Y. V. Orlovskii, T. T. Basiev, K. K. Pukhov, “Multiphonon Relaxation in Fluoride and Ternary Sulfide Laser Crystals with Neodymium Ions,” *J. Exp. Theor. Phys.*, vol. 106, 2008, Art. no. 661.
- [116] Y. V. Orlovskii, R. J. Reeves, R. C. Powell, T. T. Basiev, K. K. Pukhov, “Multiple-phonon non-radiative relaxation: Experimental rates in fluoride crystals doped with Er³⁺ and Nd³⁺ ions and theoretical model,” *Phys. Rev. B*, vol. 49, n. 6, Feb. 1994.
- [117] L. de S. Menezes, G. S. Maciel, C. B. de Araújo, Y. Messaddeq, “Thermally enhanced frequency upconversion in Nd³⁺-doped fluoroindate glass,” *J. Appl. Phys.*, vol. 90, no. 9, pp. 4498–4501, 2001.
- [118] M. C. Falconi, A. M. Loconsole, D. Laneve, L. Thi Ngoc Tran, L. Zur, A. Chiasera, R. Balda, J. Fernandez, P. Gluchowski, A. Lukowiak, M.

Ferrari, and F. Prudenzano, "Design of active devices based on rare-earth-doped glass/glass ceramic: from the material characterization to the device parameter refinement," *Proc. SPIE Fiber Lasers and Glass Photonics: Materials through Applications II*, Online Only (France), 6-10 Apr 2020.